OPTICAL VORTICES
AND
THEIR APPLICATION
TO INTERFEROMETRY

JAN MASAJADA

Institute of Physics
Wrocław University of Technology

Prace Naukowe Instytutu Fizyki
Nr 36 Politechniki Wrocławskiej Nr 36

Monografie Nr 25 2004

Optical vortex,
interferometry,
phase singularity

Wir optyczny,
interferometria,
nieciągłość fazowa

Jan MASAJADA*

OPTICAL VORTICES AND THEIR APPLICATION TO INTERFEROMETRY

Regular net of optical vortices can be generated by three plane waves interference. Such a net has a number of unique properties and its geometry is very sensitive to phase and amplitude disturbances introduced to any of the three interfering waves. The Optical Vortex Interferometer (OVI) is a new instrument which takes advantage of special properties of optical vortex net. The OVI can be set up in various configurations fitted to specific needs of measurements. The key problem for OVI accuracy is localization of vortex points. A number of localization methods, which work with subpixel resolution have been proposed and tested. These methods are fast and enable real time measurements. In this monograph, the basic physical and technical features of OVI are discussed. The possible applications of OVI are: small-angle rotations and small linear shift measurement, determination of wavefront geometry, 3-D scanning interferometry, superresolution microscopy. The measurement of small-angle rotations is presented in detail. The monograph contains also an introduction to the theory of optical vortices.

---

* Institute of Physics, Wrocław University of Technology, Wybrzeże Wyspiańskiego 27, 50-370 Wrocław.

1. Introduction

Singular Optics is a new branch of modern optics. The name was suggested by Prof. Marat Soskin from Ukraine and widely accepted. Optical singularities are classified into three categories [Nye 1999]: ray singularities, phase singularities and polarization singularities. Ray singularities were known in ancient Greece as “caustics”. The name “caustic” means the area of burning light; places where the energy of light is particularly strong. The ancient Greeks did not think about caustics as singularities – pure mathematical objects – but just as the places of very high intensity of light. Contemporary physics is written in mathematical language and physical quantities are represented by pure mathematical objects. The optical singularities are represented by singularities in mapping between two manifolds. The rigorous mathematical definition of singularity is [Lu 1976]: Let f be a differentiable mapping from M to N, where M and N are differentiable manifolds. A point $x_0 \in M$ is a singular point of f if rank $df(x_0) < \min\{\dim M, \dim N\}$, where $df(x_0)$ is the Jacobian matrix of f at x_0. Otherwise, x_0 is a regular point of f. The results of the singularity theory, although highly abstract, describe the intricate phenomena investigated in contemporary physics. For example, the classification of singular mappings provides a clear insight into the hidden order of the physical phenomena, which were believed to be chaotic before applying singular theory.

Theoretically (i.e. according to geometrical optics), the density of light energy at caustic is infinite. In practice, the caustics are softened by diffraction. A well known caustic is the focus of an ideal focusing lens. A lens with aberrations also produces caustics, but of a more complex structure. Even more complex examples are images obtained by natural “imaging” systems like a rippling water surface. For a long time, such images had been understood as a complicated example of problems that can be fully analyzed using ray tracing procedures, with the only limitation being the computation capacity. The catastrophe theory developed by Thom (1972) and Arnold (1986) gives new insight into this problem. With the catastrophe theory, the important group of stable and generic caustics can be defined; moreover, such caustics can be classified into several classes. Although these classes are defined mathematically, they have a non-trivial physical interpretation. Stability means that under a small disturbance in the optical system (like water surface reflecting sun rays), the given caustic does not change its character and still belongs to the same class. Generic means that the object in question occurs without special preparation or conditions. A discussion on these terms can be found in many works (see, for example, Nye (1999), Kravtsov *et al.* (1993)). There are a number of books (see, for example, Berry *et al.* (1980), Kravtsov *et al.* (1990, 1993), Nye (1999)) that can be used in studying the catastrophe theory.

Phase singularities, recognized by Nye *et al.* (1974), belong to the deeper level of optical singularities. For the last twenty years, an increasing number of studies have started to contribute to this subject. Phase singularities are points in the phase field where the phase is undetermined. Because the complex amplitude function must be uniquely defined at such points, the light amplitude must equal zero. In this work, special attention is paid to optical vortices (OVs). Optical vortices together with edge dislocations belong to the main categories of stable phase singularities. There is a connection between ray singularities and phase singularities, which is explained in the paper by Berry *et al.* (1980) and the book by Nye (1999).

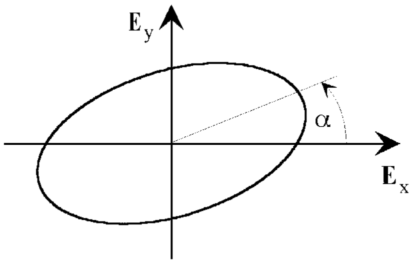

Fig. 1.1. Polarization ellipse. α is an azimuth angle

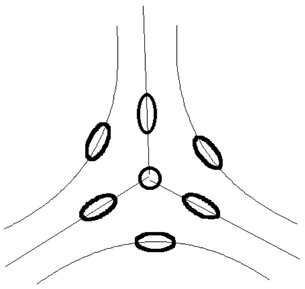

Fig. 1.2 Star pattern of polarization ellipses surrounding C-point

Polarization singularities of different kinds have been widely studied both experimentally and theoretically (see, for example, Nye (1983), Nye *et al.* (1987), Hajnal (1987a), Hajnal (1987b), Nye (1999), Berry *et al.* (2001), Freund (2001)). A simple example of polarization singularity is given here. The distribution of the polarization ellipses (Fig. 1.1) [Meyer-Arendt 1972] can be determined in an observation plane. Within such a distribution, there are points (C-points) where light has circular polarization and the azimuth is undefined, and as such, the C-points are polarization singular points (Fig. 1.2). Moreover, these points (lines in space) are structurally stable and generic structures. The relationship between phase singularities and C-points is discussed in literature (see, for example, Nye (1999)).

In modern physics "singularities" became so popular that one can perceive "Singular Physics" as a new discipline. The Singular Optics can be considered as a part of Singular Physics. In fact, optical singularities have a lot in common with singular structures existing in other branches of physics. The mathematical description is similar; hence it is possible to transfer results directly from one branch to another. For example, at the beginning, the optical singularities were described by borrowing some concepts from crystallography [Nye *et al.* 1974], where singularities are known as dislocations. Optical singularities are particularly easy to generate and process in a fully controlled laboratory experiment. They can give deeper insight into the physics of electromagnetic fields or singular structures in other branches of modern physics, for example, solid state, quantum mechanics, fluid physics and acoustics. Figure 1.3 shows the vortex generated in a scattered focused acoustic wave beam. Contrary to transversal light waves, the acoustic waves are longitudinal, but the generated phase singularities reveal similar features.

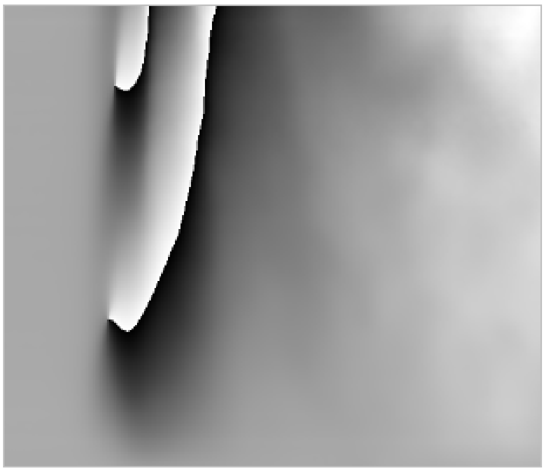

Fig. 1.3. Phase map (in grayscale) obtained by ultrasonic microscope working at frequency 5.9 MHz. There are two points around which the phase (the gray ratio) changes at 2π rate. These points are singularities in phase distribution. (Figure, courtesy of W. Grill, Leipzig University)

The other example refers to the works by Whewell, published as early as 1833 [Whewell 1833, 1836]. Whewell noticed singularities in the cotidal lines distribution. Cotidal lines are lines connecting points where the tide is high at particular times. More details on this can also be found in paper by Berry (1981) and book by Nye (1999).

This monograph is focused on OVs, which are phase singularities. It gives a brief overview of OVs properties, generation and applications. It also presents the author's works on this subject. The most important part of this work is a new kind of interferometer that was invented by the author and named Optical Vortex Interferometer (OVI). The OVI is a new promising tool in optical measurements. The monograph presents the latest results confirmed by experiment and intensive numerical and theoretical modeling.

Since the OVs are singular objects within the scalar field the light waves are represented by complex amplitude function (scalar approximation) and therefore, through this work, the light intensity is understood as square of modulus of the light complex amplitude.

The monograph is organized as follows: Chapter 2 gives some basic information on OVs and more specific on OVs diffraction by half-plane and slit. Chapter 3 describes the generation and detection of the OVs. Special attention is put on two subjects. The first are holographic techniques that are not only popular, but also used by the author. The second is the three plane waves method which is fundamental for OVI and was investigated by the author. Chapter 4 is devoted to OVI and presents the results and ideas by the author and his coworkers. Chapter 5 contains a short summary of the whole monograph. Appendix A gives a short overview of Gaussian beam family functions, which are used for laser radiation modeling and play an important role in Singular Optics. Appendix B contains a list of the most important symbols and abbreviations used throughout this work.

2. Optical vortices

2.1. Introduction

This chapter focuses on the properties of optical vortices. The OVs are important geometric features of the phase distribution of light beam. A complete analysis of geometry must include other possible topological phase structures, such as edge dislocations, saddle points, maxima and minima. Within the given wavefront all these structures have subtle influence on each other and play an intricate game. A detailed study of these dependences can be found in the literature (see, for example, Nye *et al.* (1974), Freund (1995), Nye (1999)).

The multiplicity of papers devoted to optical vortices as well as the variety of problems they deal with make a complete presentation of OVs properties impossible. The facts given below were selected because they were either fundamental or important for further consideration or were a subject of author's works. More about OVs statistical properties can be found in [Berry 1978, Freund 1994, 1995], phase singularities in non-monochromatic fields [Gbur *et al.* 2002, Popescu *et al.* 2002, Berry 2002], phase singularities and quantum mechanics [Barnett *et al.*1994, Allen *et al.* 1996, Abramochkin *et al.* 1996, Courtial *et al.* 1997, Arlt *et al.* 1999], phase singularities in non-linear media [Ackemann *et al.* 1995, Dholakia *et al.* 1996, Petrov *et al.* 1997].

2.2. Geometrical properties of optical vortices

The existence of an optical vortex (OV) in a wave field causes the presence of an isolated singular point (vortex point) in phase distribution. The simplest expression that describes such a wavefront (monochromatic and linearly polarized), which satisfies the wave equation is [Freund *et al.* 1994]

$$U(x,y,z,t) = (x + i\,sgn\,y)^m \exp\{i(\omega t - k z)\}\,. \tag{2.1}$$

In the *xy* plane (where *z* is the axis of propagation of singular point in the local coordinate system) the function (2.1) satisfies Laplace's equation and can be written as

$$U(x, y, 0, 0) = (x + i\,sgn\,y)^m = U_0(x, y)^m \exp\{i\,sgn\;m\theta\}, \tag{2.2}$$

where $U_0(x, y) = \sqrt{x^2 + y^2}$, θ is an argument of $(x + i\,sgn\,y)$, and *sgn* equals 1 for positive OV and –1 for negative OV, respectively. The integer parameter *m* indicates the value of the topological charge of OV.

Since formula (2.2) represents the monochromatic wave, the phase factor $\exp\{i(\omega t - k z)\}$ is neglected.

Figure 2.1a shows a plot of equiphase $m\theta = \text{const}$ lines given by expression (2.2). Figures 2.1b, c show this plot for real beams. The equiphase lines converge to a single point – the singular point. When the sign of OV is positive $sgn = +1$ then the phase circulates counterclockwise, otherwise it circulates clockwise. This definition depends on the direction along which the optical vortex is observed; however, in the case of two-dimensional sections, considered in this monograph, such a definition is unique and widely used in the literature. The general three dimensional case has been presented by Nye (1999). At the singular point the phase is undetermined. Since the complex amplitude function must be single valued, the light amplitude at the position of singular point is forced to zero – in equation (2.2) $U(x = 0, y = 0) = 0$. Figures A2, A3, in Appendix A, show the intensity distribution of different optical beams carrying OVs. The other way to find the positions of a singular point is to plot the lines given by the set of equations

$$\text{Re}(U) = 0, \tag{2.3a}$$

$$\text{Im}(U) = 0. \tag{2.3b}$$

The OV position is determined by the intersection point of the above lines[1] (zero lines shown in Fig. 2.2). The other characteristic feature of light beams carrying OV is their helical wavefront shape (Fig. 2.3).

So far wavefronts possessing single (including multi-charge), highly symmetrical OV were considered. In practice, OVs are not of perfect symmetry. Moreover, the real wavefronts usually contain a number of adjacent OVs. The simplest expression representing wavefronts with *N* OVs (in the *xy* cross section) is [Freund *et al.* 1993]

$$U(x, y) = \prod_{n=1}^{N} (X_n + i\,\varepsilon_n Y_n), \tag{2.4}$$

---

[1] This set of equations can also be written when zero is replaced by some other arbitrary number *const*: Re(*U*) = const and Im(*U*) = const.

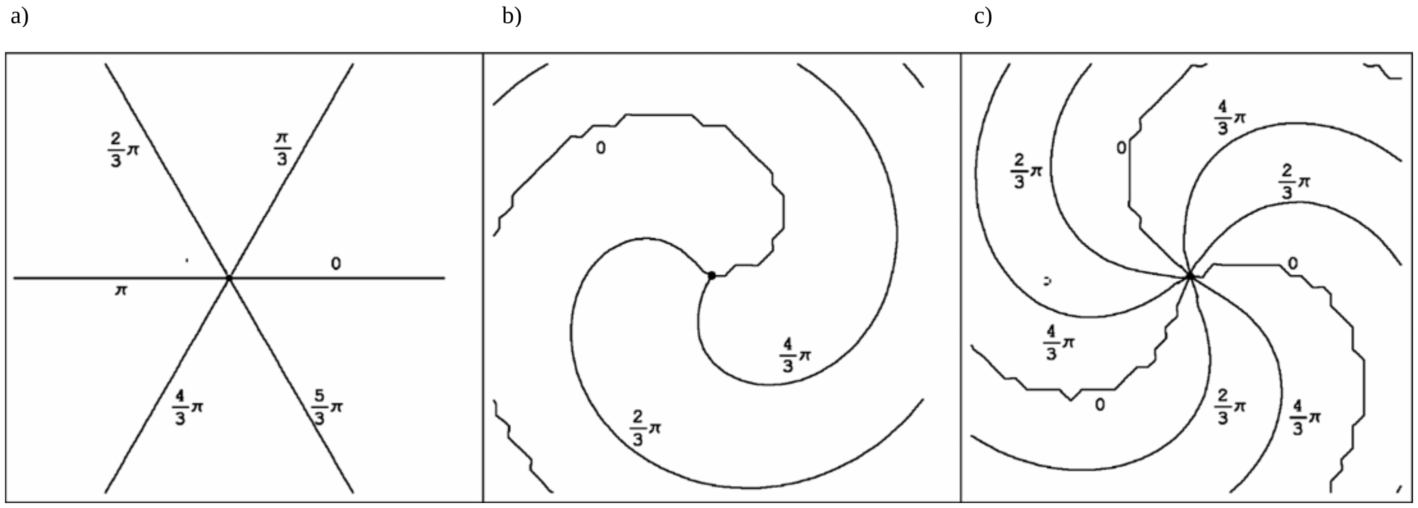

Fig. 2.1. The plot of equiphase lines in *xy* cross section for: a) wavefront described by equation (2.1) $m = 1$, $sgn = 1$; b) Gaussian wavefront with single OV; $m = 1$, $sgn = 1$. Gaussian wavefronts, which carry OVs are described in Appendix A. This wavefront is represented by formula (A7); c) Gaussian wavefront with multi-charge single OV (see formula (A7)); $m = 3$, $sgn = –1$

$$X_n(x,y) = a_n[(x - x_n)\cos(\alpha_n) + (y - y_n)\sin(\alpha_n)]\,, \qquad (2.4a)$$

$$Y_n(x,y) = a_n[-(x - x_n)\sin(\alpha_n + \sigma_n) + (y - y_n)\cos(\alpha_n + \sigma_n)]\,, \qquad (2.4b)$$

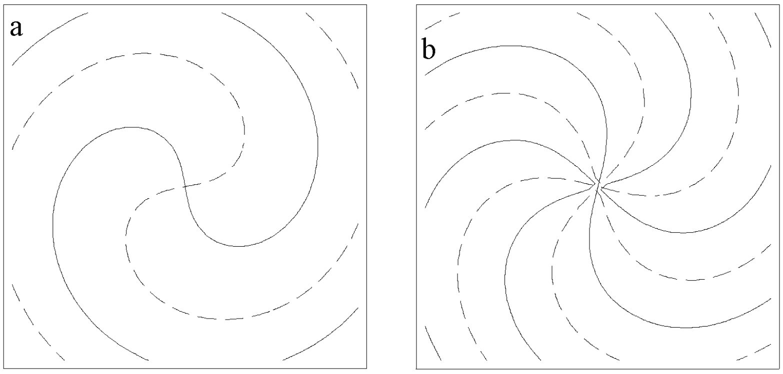

Fig. 2.2. Plot of lines Re(*U*) = 0 solid lines and Im(*U*) = 0 dashed lines for wavefront given by equation (A.7) a) *m* =1, *sgn* = 1; b) *m* = 3, *sgn* = –1

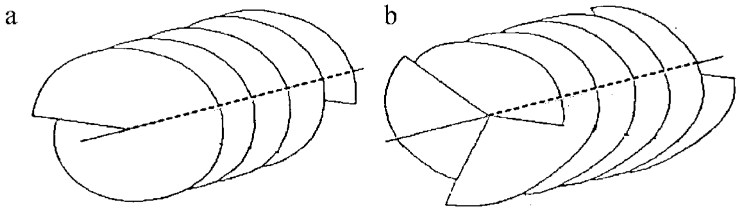

Fig. 2.3. Sketch of helical wavefronts [Basisty *et al.* 1995] of topological charge a) *m* = 1; b) *m* = 3

ε_n are parameters describing OV anisotropies (Fig. 2.4) – parameter ε can be negative and then the OV has negative topological charge, a_n are amplitude scale factors and σ_n is the skew angle different from zero if the *x* and *y* axes are non-orthogonal. The OVs with non-unit ε and/or non-zero σ will be called anisotropic. The angle α_n is measured counterclockwise between the internal dislocation *x*-axis and the laboratory *x*-axis; x_n, y_n are coordinates of *n*-th OVs. Formula (2.4) can be written as follows

$$U(x,y) = \prod_{n=1}^{N} r_n \exp\left\{ i \sum_{n=1}^{N} \varphi_n \right\} = U_N(x,y)\exp\{i\Phi_N(x,y)\}\,, \qquad (2.5)$$

where

$$r_n = \sqrt{X_n^2 + \varepsilon_n^2 Y_n^2}\ , \tag{2.5a}$$

$$\varphi_n = \mathrm{atan}\left(\frac{\varepsilon_n Y_n}{X_n}\right), \tag{2.5b}$$

$$U_N = \prod_{n=1}^{N} r_n\ , \tag{2.5c}$$

$$\Phi_N = \arg(U) = \sum_{n=1}^{N} \varphi_n\ . \tag{2.5d}$$

The above formulas show that within a given wavefront, OVs affect each other. This interaction is limited by a number of topological constraints, which will be briefly discussed below. Another description of general anisotropic OVs can be found in papers by Schechner (1996) and Freund *et al.* (1997).

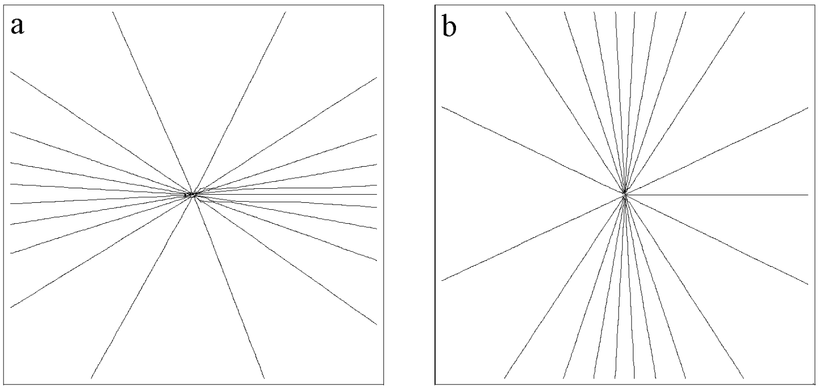

Fig. 2.4. Equiphase lines of an anisotropic single optical vortex
a) σ = 3; b) σ = 1/3

It is worth noting that expression (2.4) does not meet Laplace's equation (but the generalized term for single optical vortex $x \pm i\varepsilon y$ does). However, in this section general topological features of OVs are considered. Since these features are common for various scalar physical fields the non-optical expressions can also be used for their representation. In fact, expression (2.4) is the simplest expression that describes vortices and preserves their fundamental topological properties in a scalar field (in *xy* cross section). All properties illustrated with this expression are also present in more specific cases (including optical fields). Moreover, as has been shown by Freund *et al.*

(1993), equation (2.4) is an arbitrary close approximation to a valid solution of the wave equation (a combination of valid laser modes) over an arbitrary volume of space.

In general, within a given wavefront, the equiphase lines can form closed curves (anisotropic OVs), which end at the phase singularities or at the field boundary. Figure 2.5a shows two isotropic OVs – one with positive and other with negative topological charge and Figure 2.5b shows two isotropic OVs of positive topological charge. The equiphase lines resemble electric field lines between two electrical charges; however, this analogy is not exact in the case of anisotropic OVs, since there are no anisotropic elementary electric charges.

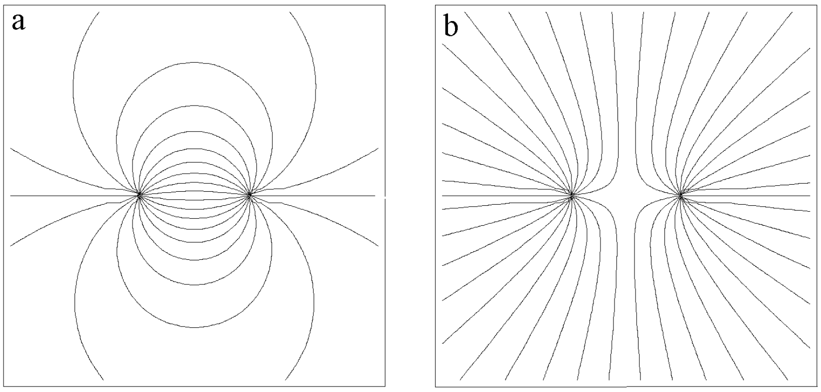

Fig. 2.5. Equiphase lines of two vortices
a) one negative and one positive vortex; b) two positive vortices

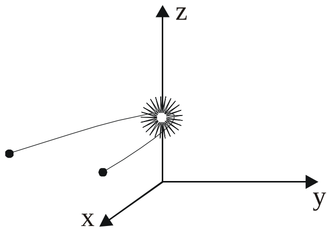

Fig. 2.6. Two OVs moving along parabola
and colliding at its vertex

As was mentioned above formulas (2.4), (2.5) exhibit the mutual influence between the OVs seeded in the given wavefront. Figures 2.5 illustrate this fact (by analogy to electrical charges). The interactions between OVs influence their dynamics as was studied in a number of papers (see, for example, Nye *et al.* (1974), Indebetouw (1993), Roux (1995), Vaupel *et al.* (1995), Rozas *et al.* (1997). Figure 2.6 shows an example of the trajectory of two OVs, which can be described by the following equation [Berry 1981]

$$U = [k c t - i k^2 x^2 - (\alpha - i \beta)(x + i y)] \exp\{i(k z - \omega t)\}\,. \tag{2.6}$$

The OVs propagate along the parabola and collide at the parabola vortex.

Mutual relations between OVs are even more rich. The sign principle introduced by Freund *et al.* (1994) gives a deeper insight into the OVs net structure.

The sign principle. Within a given wavefront the vortices on any given neighboring crossings of $\mathrm{Re}(U) = 0$ and $\mathrm{Im}(U) = 0$ must be of opposite sign.

The sign principle has a number of important implications. For example, the sign of a single vortex determines the sign of any other vortex within the given wavefront. Moreover, the sign of the first optical vortex created during the field evolution will fix the signs of all future generated vortices. Although the above formulation is limited to OVs of unit topological charge (i.e. generic OVs), it can be easily adopted to a more complex situation. The multi-charge vortex is unstable, so by adding a small perturbation to the field it can be separated into a number of single vortices. After separation one can apply the sign principle. A similar trick can be applied with respect to isolated vortices [Freund *et al.* 1994].

2.3. The angular momentum

The light beam can carry non-zero angular momentum [Allen *et al.* 1999, Allen 2002]. The mechanical effects of transfer of angular momentum associated with light polarization were first measured by Beth (1936) [Allen *et al.* 1992]. Beth used a half-wave plate suspended on a fine quartz fiber. The circularly polarized beam passed through the plate, which transformed the right-handed circular polarized light into left-handed circular polarized light. The measured torque of the half-wave plate was evidence of angular momentum transfer and was in good quantitative agreement with the theory. The beams carrying OVs also possess non-zero angular momentum. Thus, the total angular momentum of light has two components which are called, by analogy to the components of total electron angular momentum in atom, the spin and orbital angular momentum. However, in the case when the paraxial approximation is not valid, the separation of these two components may be a difficult task [Allen *et al.* 1999].

The transfer of orbital angular momentum between light and matter was observed for the first time in the experiment reported by He *et al.* (1995). A vortex beam was generated using a special blazed hologram. Then the vortex beam was directed (by microscope) into a liquid containing absorptive particles. The particles rotated in the direction determined by the sign of OVs topological charge, and rotation was observed by microscope.

The nonzero angular momentum means that OVs in free propagation are stable features. However, the vortex free beams can also carry nonzero angular momentum, which was reported by Courtial *et al.* (1997). This fact makes the relation between OVs and light beam angular momentum more complicated, which was illustrated in the paper by Soskin *et al.* (1997), where the propagation of the combination of Gaussian beams with OVs and without OVs is analyzed.

2.4. Vortex diffraction

In this section, the fundamental problem in physical optics, i.e. the diffraction phenomenon, will be discussed. The important question is: how do the OVs behave while the carrier beam is a subject of diffraction? This question is studied in the most elementary case of diffraction by half-plane and the slit. The diffraction of pure Gaussian beams by half-plane was studied in the paper by Pearson *et al.* (1969). A more rigorous approach was recently presented by Peterson *et al.* (2002). Gaussian beam diffraction was also studied for circular apertures and thin lenses using both numerical and analytical methods (see, for example, Krauss (1988), Toker *et al.* (1993), Gu *et al.* (1997)).

The simplest diffraction process, i.e. diffraction of Gaussian beams with OVs on a half plane and a slit, was studied by Masajada (2000a, b, c). The calculations were performed both numerically and analytically. The analytical calculations were based on scalar Kirchhoff diffraction integral in Fresnel approximation. The reliability of a simple numerical algorithm used for computer calculations is shortly discussed in section 3.2.4.

The Fresnel diffraction integral for the one dimensional slit with edges at position q and h with respect to the x-axis has the form [Goodman 1968]

$$U(x_i, y_i, z_i) = \Omega \int_h^q \int_{-\infty}^{\infty} U(x, y, z_D) \exp\left\{ \frac{-i\,k}{2\,z_i} [(x_i - x)^2 + (y_i - y)^2] \right\} dx\,dy\,, \qquad (2.7)$$

where: coordinates x_i, y_i, z_i refer to the image plane,

$$\Omega = \frac{\exp\{-i\,k\,z_i\}}{i\,z_i\,\lambda}\,, \qquad (2.7a)$$

$U(x, y, z_D)$ is the complex amplitude of diffracted beam (A.7) in object plane. For calculation purposes the binomial $(x + i\,sgn\,y)^m$ can be expanded and the complex amplitude U becomes

$$U(x, y, z_D) = U_z \exp\{-r^2 A\} \sum_{t=0}^{m} \binom{m}{t} sgn^t\, i^t\, x^{m-t}\, y^t\,, \qquad (2.8)$$

where

$$U_z = U_0 \frac{w_0}{w_z^{m+1}} \exp\left\{ -i\,(m+1)\,\mathrm{atan}\left(\frac{z_i}{z_R} \right) \right\} \exp\{i\,k\,z_i\}\,. \tag{2.8a}$$

In the case of $m = 1$ the integral (2.7) can be rewritten as

$$U(x_i, y_i, z_i) = T\,[U1_x\,U_y + i\,sgn\,U_x\,U1_y]\,, \tag{2.9}$$

where

$$T = U_0\,\Omega \exp\{-i\,K\,(x_i^{\,2} + y_i^{\,2})\}\,, \tag{2.9a}$$

$$K = k\,/\,2z_i\,, \tag{2.9b}$$

$$U1_x = \int_{-\infty}^{\infty} x \exp\{-Gx\}\,dx = i\sqrt{\pi}\,K\,F^{-\frac{3}{2}}\,x_i \exp\left\{ -\frac{K^2}{F}\,x_i^{\,2} \right\}, \tag{2.9c}$$

$$U_y = \int_q^h \exp\{-Gy\}\,dy = \frac{1}{2}\sqrt{\frac{\pi}{F}} \exp\left\{ -\frac{K^2}{F}\,x_i^{\,2} \right\} [\mathrm{erf}(H) - \mathrm{erf}(G)]\,, \tag{2.9d}$$

$$U_x = \int_{-\infty}^{\infty} \exp\{-Gx\}\,dx = \sqrt{\frac{\pi}{F}} \exp\left\{ -\frac{K^2}{F}\,x_i^{\,2} \right\}, \tag{2.9e}$$

$$U1_y = i\int_q^h y \exp\{-Gy\}\,dy = \frac{1}{2F}[\exp\{-q^2\,F + i\,2\,q\,K\,y_i\} - \exp\{-h^2\,F + i\,2\,h\,K\,y_i\}]$$
$$+ \frac{i\sqrt{\pi}\,K\,y_i}{2} \exp\left\{ -\frac{K^2}{F}\,y_i^{\,2} \right\} [\mathrm{erf}(G) - \mathrm{erf}(H)]\,, \tag{2.9f}$$

$$G = \frac{q\,F - i\,Ky_i}{\sqrt{F}}\,, \tag{2.9g}$$

$$H = \frac{h\,F - i\,Ky_i}{\sqrt{F}}\,, \tag{2.9h}$$

$$F = A + i\,K\,, \tag{2.9i}$$

$$Gx = x^2\,(A + i\,K) + 2\,i\,K\,x_i\,x\,, \tag{2.9j}$$

$$Gy = y^2\,(A + i\,K) + 2\,i\,K\,y_i\,y\,. \tag{2.9k}$$

A is given by formula (A.9) and function erf (z) is defined as [Erdèlyi *et al.* 1953]

$$\mathrm{erf}(z) = \frac{2}{\sqrt{\pi}} \int_0^z e^{-t^2} dt\,. \tag{2.9l}$$

In the case of half-plane, $h \to \infty$. The limit $h \to \infty$ can be evaluated under the condition $\arg(H) \to \alpha$ and $|\alpha| < \pi/4$ [Erdèlyi *et al.* 1953]. The expressions for U_y and $U1_y$ become

$$U_y = \frac{1}{2}\sqrt{\frac{\pi}{F}} \exp\left\{-\frac{K^2}{F} x_i{}^2\right\} \mathrm{erfc}(G)\,, \tag{2.10a}$$

$$U1_y = \frac{1}{2F} \exp\{-q^2 F + i\,2\,q\,K y_i\} + \frac{i\sqrt{\pi}\,K}{2} y_i \exp\left\{-\frac{K^2}{F} y_i{}^2\right\} \mathrm{erfc}(G)\,, \tag{2.10b}$$

where function $\mathrm{erfc}(z)$ is defined as [Erdèlyi *et al.* 1953]

$$\mathrm{erfc}(z) = \frac{2}{\sqrt{\pi}} \int_z^\infty e^{-t^2} dt = 1 - \mathrm{erf}(z)\,. \tag{2.10c}$$

In order to calculate the integral (2.7) for the case of higher values of topological charge *m*, the iteration formula, which is briefly derived below, is necessary. First, the following expression can be written

$$IT = \int_q^h y^n \exp\{-Gy\}\, dy = \frac{1}{n+1} y^{n+1} \exp\{-Gy\} \Bigg|_q^h$$

$$- \frac{1}{n+1} \int_q^h y^{n+1} (-2y\,F + i\,2K y_i\, y) \exp\{-Gy\}\, dy. \tag{2.11a}$$

Let

$$L = \frac{1}{n+1} y^{n+1} \exp\{-Gy\} \Bigg|_q^h\,, \tag{2.11b}$$

then

$$IT = L + \frac{2F}{n+1} \int_q^h y^{n+2} \exp\{-Gy\}\, dy$$

$$- \frac{2i}{n+1} K y_i \int_q^h y^{n+1} \exp\{-Gy\}\, dy. \tag{2.11c}$$

Finally, the following iteration formula can be written

$$\int_q^h y^{n+2}\exp\{-Gy\}\,dy = i\frac{K}{F}y_i\int_g^h y^{n+1}\exp\{-Gy\}\,dy + \frac{n+1}{2F}\int_q^h y^n\exp\{-Gy\}dy$$

$$-\frac{1}{2F}\left[h^{n+1}\exp\{-h^2F + i\,2Ky_i\,h\} - q^{n+1}\exp\{-q^2F + i\,2Ky_i\,q\}\right]. \qquad (2.11d)$$

In the case of OV with charge two the integral (2.7) has the solution

$$U(x_i, y_i, z_i) = T[U2_x\,U_y + i\,2sgnU1_x\,U1_y - U2_y\,U_x], \qquad (2.12)$$

where

$$U2_x = \int_{-\infty}^{\infty} x^2\exp\{-G\,x\}\,dx = -\frac{\sqrt{\pi}}{4}\frac{4K^2x_i^{\,2} - 2F}{F^{\frac{5}{2}}}\exp\left\{-\frac{4K^2x_i^{\,2}}{4F}\right\}, \qquad (2.12a)$$

$$U2_y = \int_{-\infty}^{\infty} y^2\exp\{-G\,y\}\,dy = -\frac{\exp\{-h^2F + i\,2Ky_i\,h\}}{2F}\left(h + \frac{i\,2Ky_i}{2F}\right)$$

$$+\frac{\exp\{-q^2F + i\,2Ky_i\,q\}}{2F}\left(q + \frac{i\,2Ky_i}{2F}\right) + \frac{\sqrt{\pi}}{4}F^{-\frac{3}{2}}\exp\left\{-\frac{4K^2y_i^{\,2}}{4F}\right\}$$

$$\left(1 - \frac{4K^2y_i^{\,2}}{2F}\right)[\mathrm{erf}(H) - \mathrm{erf}(Q)]. \qquad (2.12b)$$

In the case when $h \to \infty$ the expression for $U2_y$ is

$$U2_y = \frac{\sqrt{\pi}}{4}\left(F^{-\frac{3}{2}} - 2K^2y_i^{\,2}F^{-\frac{5}{2}}\right)\exp\left\{-\frac{4K^2y_i^{\,2}}{4F}\right\}\mathrm{erfc}(Q)$$

$$+\frac{\exp\{-q^2F + i\,2K\,y_i\,q\}}{2F}\left(q + \frac{i\,2K\,y_i}{2F}\right). \qquad (2.13)$$

In the case of optical vortex with charge three the integral (2.7) has the solution

$$U(x_i, y_i, z_i) = T[U3_x\,U_y + i\,3sgnU2_x\,U1_y - 3U1_x\,U2_y - i\,sgnU_x\,U3_y], \qquad (2.14)$$

where

$$U3_x = \int_{-\infty}^{\infty} x^3\exp\{-Gx\}\,dx = i\frac{\sqrt{\pi}}{2}F^{-\frac{5}{3}}Kx_i\left(3 - 4\frac{K^3x_i^{\,3}}{F}\right)\exp\left\{\frac{K^2x_i^{\,2}}{F}\right\}, \qquad (2.14a)$$

$$U3_y = \int_q^h y^3 \exp\{-Gy\}\, dy = \exp\{-h^2 F + i\, 2Ky_i\, h\}$$

$$\left(-\frac{h^2}{2F} - \frac{2Ky_i\, h}{4F^2} + \frac{4K^2 {y_i}^2}{8F^3} - \frac{1}{2F^2} \right)$$

$$-\exp\{-q^2 F + i\, 2Ky_i\, q\} \left(-\frac{q^2}{2F} - \frac{2Ky_i\, q}{4F^2} + \frac{4K^2 {y_i}^2}{8F^3} - \frac{1}{2F^2} \right)$$

$$+ i\sqrt{\pi} \left(\frac{6}{8} F^{-\frac{5}{2}} Ky_i - \frac{2}{16} F^{-\frac{7}{2}} Ky_i \right) (\mathrm{erf}(H) - \mathrm{erf}(Q))\,. \tag{2.14b}$$

When $h \to \infty$ the expression for $U3_y$ becomes

$$U3_y = \int_q^\infty y^3 \exp\{-Gy\}\, dy = \frac{\exp\{-q^2 F + i\, 2Ky_i\, q\}}{2F} \left(q^2 + \frac{i\, Ky_i\, q}{F} - \frac{K^2 {y_i}^2}{F} + \frac{1}{2F} \right)$$

$$+ i\sqrt{\pi} \left(6F^{-\frac{5}{2}} Ky_i - 4F^{-\frac{7}{2}} K^3 {y_i}^3 \right) \mathrm{erfc}(Q)\,. \tag{2.15}$$

Obviously, the above formulas are complicated and it is rather hard to conclude about the singular point behaviour under diffraction. Nevertheless, these formulas can be used for numerical studies and can be treated as a reference for testing the numerical procedures.

2.4.1. Examples

In this section, a number of numerical examples based on formulas derived in the previous paragraph are presented. Numerical calculations were performed in two different ways. In the first, formulas (2.9)–(2.15) were used, in the second, the Fresnel diffraction integral (2.7) was computed numerically. An agreement between results obtained by both methods showed that formulas and numerical integration were put into the program in the right way. Additionally, calculations were made for each of the cases, assuming either a wide open slit or a half-plane being shifted down by a large distance. Such cases are equivalent to the free space propagation and as expected, the calculated diffracted beams were the same as the incident one, but scaled.

In the first example, the focused Gaussian beam with single OV diffracted by half-plane is considered. The beam parameters are $w_0 = 0.04$ mm, $z_D = 15$ mm (see Appendix A); where z_D is a distance between beam waist plane and half-plane edge. The distance between half-plane and image plane is 500 mm. Figure 2.7 shows the Gaussian beam intensity and the plot of zero lines. Figure 2.8 shows the localization of the OV (in image plane) with respect to the position of half-plane edge. The results are not surprising. The vortex position in the image is almost central for large negative value of *q*, when the central part of the beam is widely open and the diffraction by edge occurs in area of small light intensity of the incident beam. When the edge stops the beam in the area of highest intensity (*q* is equal to about –0.1 mm or less) the vortex shift is larger. The vortex shift

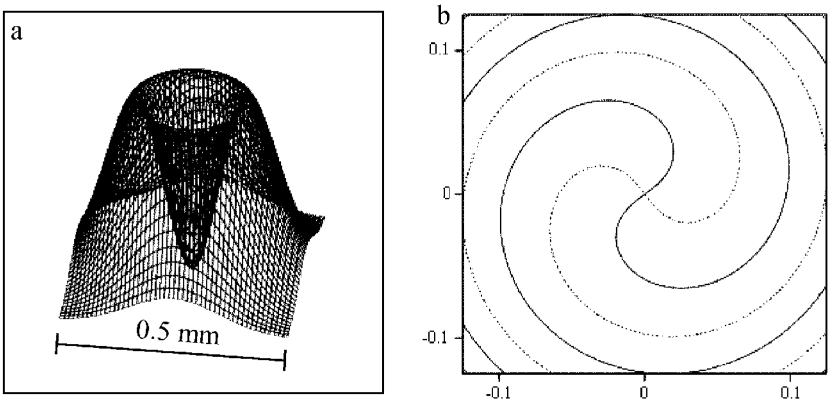

Fig. 2.7. The plot of focused Gaussian beam with single OV. The beam is plotted in half-plane plane. a) intensity, b) real (solid) and imaginary (dotted) zero lines. Values are given in millimeters

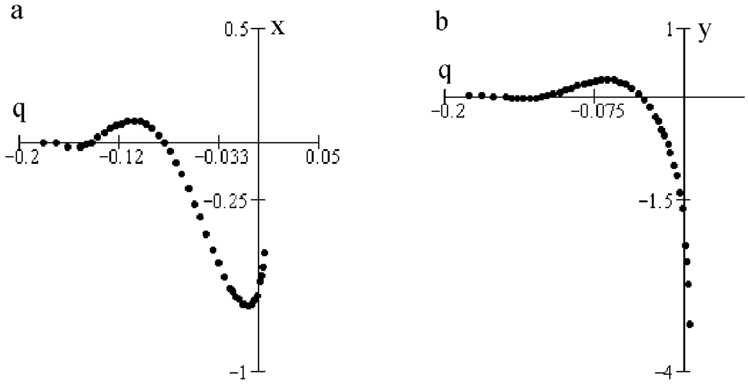

Fig. 2.8. The plot of the OV position in image plane against the edge position of the half-plane (measured along *y*-axis). a) *x*-coordinate; b) *y*-coordinate. The distances are given in millimeters

occurs in both directions *x* and *y*, but these shifts differ in character. When *q* crosses zero value the half-plane stops the central beam point, but it does not stop the vortex point. It is still reconstructed at the diffraction image, but its shift from the central point increases rapidly. The last three points in Figure 2.8 are plotted for *q* = (0.001, 0.002, 0.003) mm and the y coordinates are $y = (–2.4, –2.7, –3.3)$ mm, respectively.

This shows that the OV is a global, and not a point (i.e. strictly bounded to the vortex point) phenomenon. Increasing q value beyond the values shown in Figure 2.8 causes a rapid shift of the vortex point towards negative y-values. This global character of the OVs will be illustrated in the last part of this section by analyzing the diffraction by a ring. Geometrically the vortex point shifts into the shadow part of the image. Hence, when parameter q becomes zero, localization of the vortex point becomes difficult. The shift along the x-axis is due to the beam phase distribution asymmetry (Fig. 2.7b); i.e. when part of the beam is covered by a half-plane the phase distribution of the open part of the beam has broken symmetry. As expected, the x-shift is great when parameter q is close to zero; where the open beam asymmetry is higher, but not exactly for $q = 0$, when the beam intensity is close to zero.

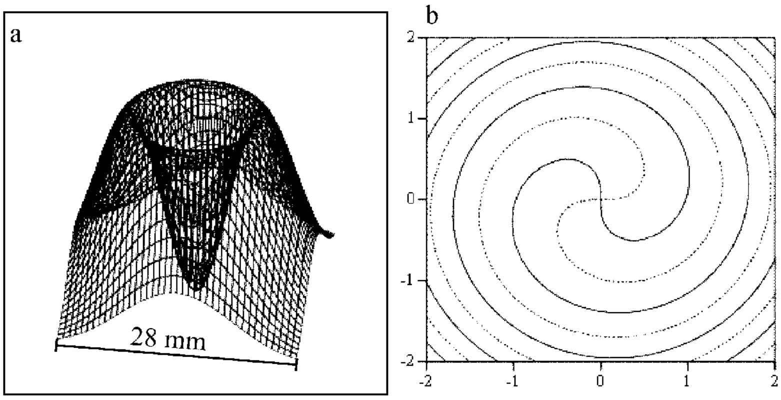

Fig. 2.9. The plot similar to that of Figure 2.7 but for quasi-plane Gaussian beam

The next example is a nearly plane Gaussian beam with single OV (Fig. 2.9). The beam parameters are $w_0 = 0.055\,\text{mm}$, $z_D = 3000\,\text{mm}$. The diffracted beam behavior is more complicated. When gradually stopping the beam with the half-plane one observes, in the image plane, a different number of vortex points. For some values of parameter q the new vortices are born in pairs of opposite topological charges and for some other values of q these extra vortex pairs annihilate. Figure 2.10 shows an example of such behavior. The vortex points are exposed by interference images as characteristic fork-like structures. The process of vortex creation is particularly strong when the half-plane edge covers an area were the light intensity is maximal. In the case of a quasi-plane beam such an area is wide and relatively distant from the vortex point. The creation and annihilation of new vortex points do not wipe away the original vortex point, which moves in a similar way as in the previous case. However, in this case the original vortex path is slightly disturbed by the presence of other vortex points. It is worth noting that increasing the distance between half-plane and observation plane changes the number of vortex points.

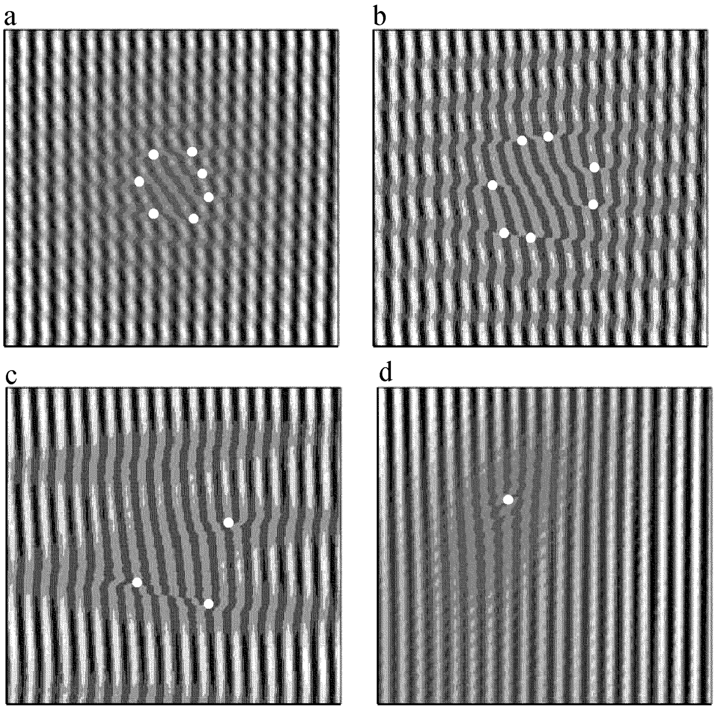

Fig. 2.10. Interferometric images of the quasi-plane Gaussian beam with single OV diffracted by the half-plane. The distance between half-plane and observation plane is 500 mm. The diffraction images were calculated using formulas (2.7)–(2.15) and the off-axis plane wave was added numerically to calculate the interference fringes. Characteristic fork-like fringe structures (pointed by white circles) indicate the location of OV. a) $q = -8$; b) $q = -5$; c) $q = -2$; d) $q = -0.3$

A further observation plane corresponds to a lower number of extra vortex points. This shows that the vortex reconstruction process is complicated. The light energy of the plane beam is spread over some larger area compared to the focused beam, and it seems to be the main reason for its different behavior. The other reason is that for the strongly divergent beam, the far field area is closer than for the almost flat phase front. When the half-plane edge moves to the beam center (where light intensity is low) the diffraction effects that are responsible for the creation of new vortices have smaller influence and no new vortices appear. When the half-plane edge goes beyond the vortex point in the incident beam the vortex point in the observation plane “flies” rapidly along the *y*-axis into the dark part of the image, as in the case of focused Gaussian beam with OV.

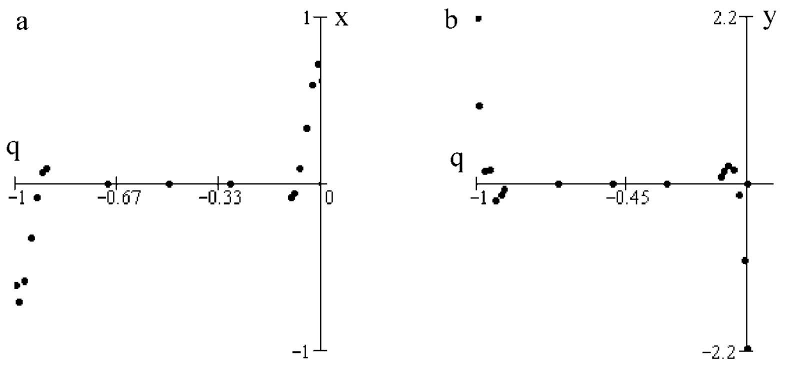

Fig. 2.11. The plot of OV position in image plane against the slit left edge position (along *y*-axis). The slit width is 1mm. When $q = 0.5$ the vortex point lies at slit center. The incident beam is shown in Figure 2.7. a) *x*-coordinate; b) *y*-coordinate. Values are given in millimeters

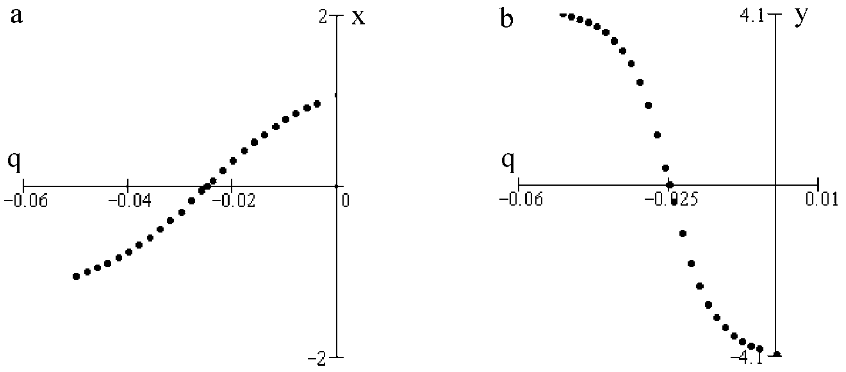

Fig. 2.12. The plot of OV position in image plane against the slit left edge (along *y*-axis). The slit width is 0.05 mm. When $q = 0.025$ the vortex point lies at slit center. The incident beam is shown in Figure 2.7. a) *x*-coordinate; b) *y*-coordinate. Values are given in millimeters

Next example is an image of the focused Gaussian beam with single OV diffracted by a slit. The beam parameters are as in the first example. Figures 2.11, which have the same form as Figures 2.8, show the OV path in respect of parameter q describing the position of the slit left edge. The slit has 1 mm in width and is much wider than the beam spot (Fig. 2.7a). That is why diffraction can be considered as two independent cases of diffraction by two half-planes. When the parameter q is –0.5 mm, the incident beam center (vortex point) coincides with the slit center. When $q = 0$, the left edge of the slit coincides with the vortex point. When $q = -1$, the right edge of the slit coincides with the vortex point. Comparison between Figures 2.8 and 2.11 shows that the dynamics of the vortex point is similar in both cases. It should be kept in mind that the figures are plotted with different ranges of variable *q* and Figure 2.11 consists of two parts representing diffraction by both edges of the slit. In Figure 2.8 negative values of coordinate *x* (for small *q*) correspond to negative values of coordinate *y*, while in Figure 2.11 the negative values of coordinate *x* correspond to positive values of coordinate *y*. This is due to different topological charge of the OV carried by the incident beam in the first and the third example. Figures 12 show one more interesting case. The slit width is 0.05 mm and is smaller than beam radius. Now at the central positions of the incident beam diffraction occurs on both slit edges. The beam center hits the slit center when *q* = 0.025 mm. The plot looks more smooth when compared to that from Figure 2.11. In Figure 2.11 there is a wide area of zero shift when the beam goes between slit edges without touching them. In the present case vortex reaction is more pronounced in both *x* and *y* directions.

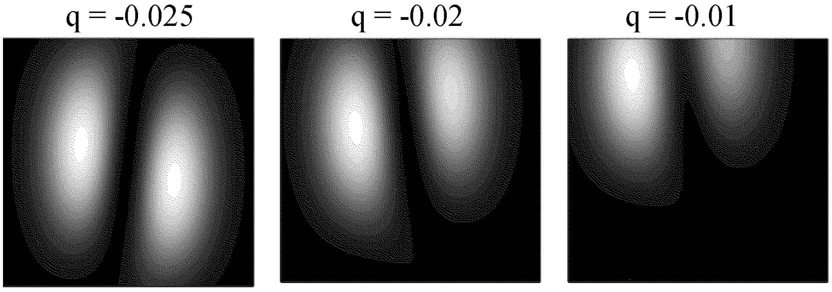

Fig. 2.13. Gaussian beam with single OV (Fig. 2.7) diffracted by a slit of 0.05 mm width. For *q* = –0.025 mm the vortex point lies at slit center. For smaller *q* the vortex point moves towards the slit edge. The figures are plotted in such a way that vortex point lies in their center. When incident beam moves off the slit center the vortex point moves towards the dark part of the diffraction image. The intensity asymmetry in the first figure, when vortex point lies at the slit center is due to broken radial symmetry of Gaussian beam which is partially covered by the slit. The vortex with opposite sign gives opposite orientation of this asymmetry

Consider the beam approaching the slit edge from the shadow side. The question is: when does the vortex carried by the beam start to interfere with the slit? Theoretically, a perfect vortex beam interferes with the slit at any distance from the beam center. However, this fact has no practical meaning if a vortex point is apart from a slit center by a distance a bit larger than half of the slit width. If this happens the vortex point is reconstructed by diffraction deeply in the dark part of the diffracted beam and cannot be detected. When the beam moves towards the slit center the vortex point approaches the optical axis of the image plane. When passing the slit center the vortex point goes towards the dark part of the diffraction image, but on the opposite side. In the case when the narrow slit center coincides with the vortex point position, the open part of the incident beam has lower symmetry. The symmetry is still enough to keep the vortex point at the image center, but the intensity distribution of the diffracted beam is no longer symmetrical. Figure 2.13a shows the intensity plot for this case. The image is asymmetrical and when changing OV charge to its opposite, the asymmetry of the diffraction image has the opposite orientation. Figure 2.13 shows also how the vortex point moves towards shadow part of the image, when the slit moves.

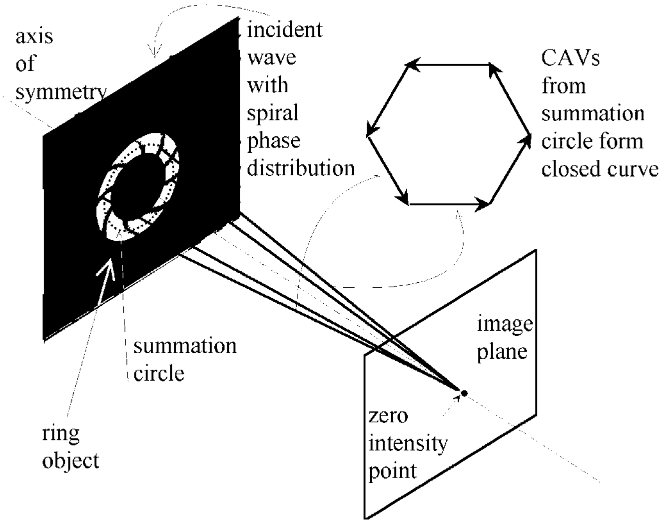

Fig. 2.14. Schematic plot showing the reconstruction of the vortex point when the Gaussian beam with single OV is diffracted by a ring

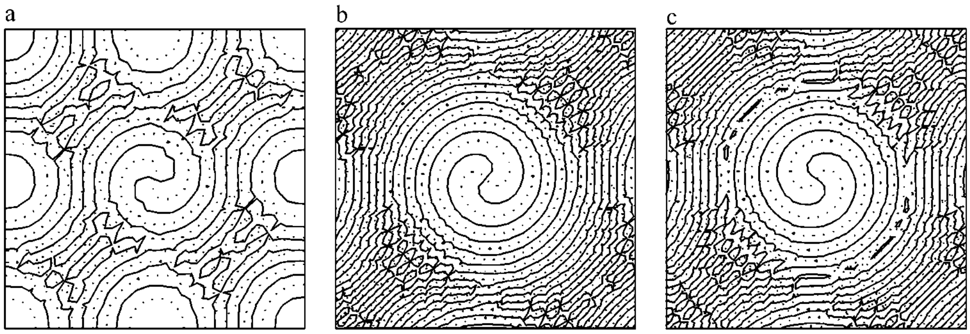

Fig. 2.15. The plot of lines Re(0) = 0 (solid line) and Im(0) = 0 (dotted line) for the focused Gaussian beam with single OV diffracted by ring.
a) the circular stop of radius 0.35 mm which covers more than 90% of the incident beam;
b) ring with inner radius 0.15 mm and external radius 0.2 mm; c) ring with inner radius 0.3 mm and external radius 0.35 mm. The cross section of solid and dotted line in the middle of the plot shows that the OV is not destroyed by diffraction and preserves its position.
In the marginal part of the figures the density of equiphase lines is too high to plot it properly

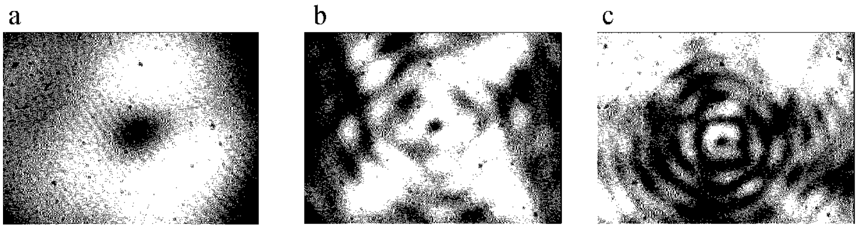

Fig. 2.16. The experiment showing the diffraction of a Gaussian like beam with single OV generated by synthetic hologram (Fig. 3.1d). a) The intensity distribution at diffraction plane; b) diffraction by small radius narrow ring; c) diffraction by large radius narrow ring

The diffraction of Gaussian beams carrying optical vortices of higher topological charges results in more intricate behavior. The multi-charge OV is not stable phenomenon and splits into single OVs when introduced to a small perturbation. A number of new born vortices are also present in the diffracted beam. This results in complicated dynamics in the diffraction image. Some examples are given in Masajada (2000b). For the author the present investigation was an introduction to the more advanced problem of the diffraction of Gaussian beams with OVs by microstructure [Masajada (2000c)]. This in turn has an important practical application in microscopy (see, for example, section 4.5).

The ring or circular stop are objects where the global character of the OVs can be illustrated in the simplest way. Figure 2.14 shows that at the central point (in the image plane) the contribution of CAVs having the same amplitude, but phases going through full angle adds to zero. Since the whole image can be reconstructed from such sums the intensity at the central point is equal to zero and there is a single vortex point there. Figures 2.15 and 2.16 show results of calculations (numerical integration) and experiment for the Gaussian beam with single OV stopped by ring.

3. Generation and detection of optical vortices

3.1. Introduction

Several methods have been developed for generation of optical vortices. Two of those of methods are of special interest to the author, i.e. synthetic holograms and the three plane waves interference. The most popular method of generating optical vortices uses synthetic holograms. The aforementioned method is very flexible, and in the case of low spatial frequency holograms, it is available without special printing equipment. The manufacturing of the highest quality synthetic holograms demands an advanced and expensive technology. The generation by three plane waves interference can also be realized in a simple and inexpensive way; generating a highly controllable net of single OVs, which can be used in optical metrology.

Apart from the holographic and three plane waves methods, several other ways of OVs generation were proposed and tested in experiments. These are: phase converter made with cylindrical lenses [Allen *et al.* 1992, Allen *et al.* 1999; Courtial *et al.* 1999, O'Neil *et al.* 2000], generation by spiral phase masks [Khonina *et al.* 1992, Beijersbergen *et al.* 1994, Turnbull *et al.* 1996, Allen *et al.* 1999], laser modes separation [Coullet *et al.* 1989, Brambilla *et al.* 1991, Coats *et al.* 1994, Harris *et al.* 1994a, Abramochkin *et al.* 1997] and light propagation through non-linear media [Indebetouw *et al.* 1994, Ackemann *et al.* 1995].

3.2. OVs generation by synthetic holograms

It is possible to design holograms that produce beams carrying single or multiple OVs, while meeting some specific conditions regarding their geometry. There are a number of synthetic hologram fabrication methods that can be used for this purpose. The low quality holograms can be printed onto foil with a high resolution laser or ink printer. Following this method one can get holograms that are sufficient enough for simple demonstrations in student laboratories. The highest quality holograms are plotted using electron lithography (see, for example, Turunen *et al.* (1997)). The literature concerning synthetic holograms is vast (see Soifer (2001) for references). There are also a number of works devoted to synthetic holograms that generate phase singularities (see, for example, Arlt *et al.* (1998), Vasnetsov *et al.* (1999)). This subject cannot be fully presented in this short monograph. The author has focused on aspects that are more widely discussed in the literature or are the subject of his particular interest.

3.2.1. Theory

Consider the interference pattern on a screen in the *x*-*y* plane when a plane reference beam

$$U_p = U_{0p} \exp\{i \cdot (k_x r_x + k_z r_z + \delta_0)\} \tag{3.1}$$

is incident at an angle $\vartheta = \mathrm{asin}(k_x / k)$. Here, δ_0 is a relative phase shift between reference and object beam. The object beam is a Gaussian beam that carries a single OV (see Appendix A, eq. (A.8)). The light intensity on a screen at $z = 0$ will be

$$I = \left| \left(U_{0p} \exp\{i k_x r_x + \delta_0\} + U_0 \frac{\rho}{w_z} \exp\{i(\varphi + \Phi_G)\} \exp\left\{ -\frac{\rho^2}{w_z^2} \right\} \right) \right|^2 , \tag{3.2}$$

which yields

$$I = U_{0p}^2 + U_0^2 \frac{\rho^2}{w_z^2} \exp\left\{ -2\frac{\rho^2}{w_z^2} \right\} + 2 U_{0p} U_0 \exp\left\{ -\frac{\rho^2}{w_z^2} \right\} \cos(\varphi - k_x x + \Phi_G + \delta_0) . \tag{3.2a}$$

The last term in equation (3.2a) expresses the interference pattern, which should produce the beam carrying OVs. The first two terms can be neglected because they produce an amplitude background of the interference pattern. For the same reason, the amplitude factor in the interference term can be neglected. To neglect the Gouy phase term Φ_G [Siegman 1986], the condition for beam curvature $R(z) = \infty$ is assumed. Now the hologram transmission is [Vasnetsov *et al.* 1999]

$$T = \frac{1}{2}(1 - \cos(\varphi - k_x r_x + \delta_0)) . \tag{3.3}$$

Formula (3.3) describes the fringe pattern to be printed onto the hologram. If such a hologram is reconstructed with a Gaussian beam, the field just behind the hologram will be

$$U_r = \frac{A_0}{2}\exp\left\{-\frac{\rho^2}{w_z^2}\right\} - \frac{A_0}{4}\exp\left\{-\frac{\rho^2}{w_z^2}\right\}\exp\{i(k_x r_x - \varphi + \delta_0)\} -$$

$$\frac{A_0}{4}\exp\left\{-\frac{\rho^2}{w_z^2}\right\}\exp\{-i(k_x r_x - \varphi + \delta_0)\}, \tag{3.4}$$

where A_0 is the amplitude of the reconstructing beam and w_z is its transverse dimension. The zero order beam is vortex free; however, the first-order beams contain a phase component $\exp\{\pm i\varphi\}$ characteristic of helical beams.

To print the sinusoidal fringes requires high resolution lithography. For most purposes it is enough to produce binarized holograms. The aforementioned binarization means here that in areas where light intensity is higher than half of the maximum, its value is made equal one, and in other cases, the intensity is put to zero. After binarization, the transmission of the hologram under consideration can be written as [Heckenberg *et al.* 1992]

$$T = \frac{1}{2} - \sum_{n=1}^{\infty} \operatorname{sinc}\left(\frac{n}{2}\right)\cos[n(\varphi - k_x r_x) + \delta_0]. \tag{3.5}$$

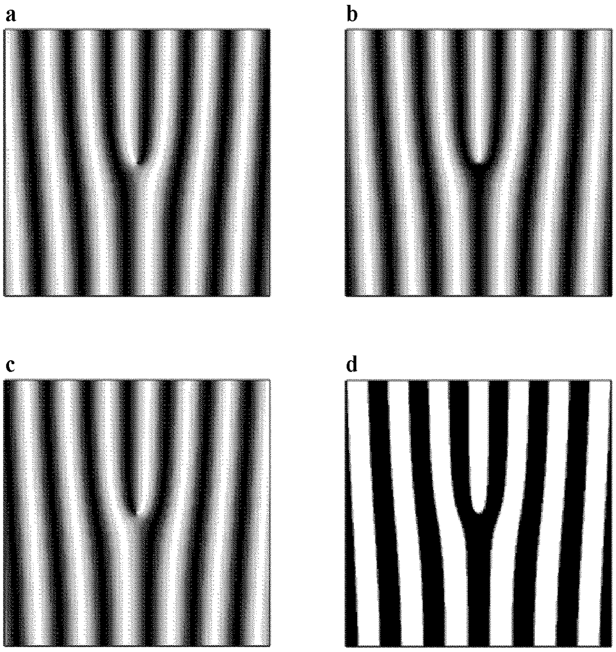

Fig. 3.1. Holograms plotted using equations (3.3) (cases a, b, c) and (3.5) (case d).
a) $\delta_0 = 0$; b) $\delta_0 = \pi/2$; c) $\delta_0 = \pi$; d) $\delta_0 = \pi/2$ and the number of terms in sum (3.8) is 9

Figure 3.1 shows examples of holograms given by equations (3.3) and (3.5).

In the reconstruction of binarized holograms, numerous beams corresponding to subsequent diffraction orders are generated. The *n*-th order beam can be described as

$$I_n = \frac{A_0}{4}\operatorname{sinc}\left(\frac{n}{2}\right)\exp\left\{-\frac{\rho^2}{w_z^2}\right\}\exp\{i(n\varphi - n k_x r_x + \delta_0)\}\,. \tag{3.6}$$

Each term contains the factor $\exp\{i n\varphi\}$, which is characteristic of the helical beam of charge *n* and propagating at an angle $\vartheta_n = \operatorname{asin}(n k_x / k)$. It can be shown that the *n*-th order diffracted beam (3.6) generated by the hologram given in formula (3.5) (under Gaussian beam illumination) is closely related to Laguerre–Gauss beams with *n*-th order OVs (A.5) [Heckenberg *et al.* 1992].

To produce the hologram which generates in the first diffraction order the beam carrying OV of charge *m*, the fringe equation (3.3) has to be written as

$$T = \frac{1}{2}(1 - \cos(m\varphi - k_x r_x + \delta_0)) \tag{3.7}$$

and formula (3.5) becomes

$$T = \frac{1}{2} - \sum_{n=1}^{\infty}\operatorname{sinc}\left(\frac{n}{2}\right)\cos[n(m\varphi - k_x r_x) + \delta_0]\,. \tag{3.8}$$

Figure 3.2 shows two examples of holograms given by equations (3.7) and (3.8).

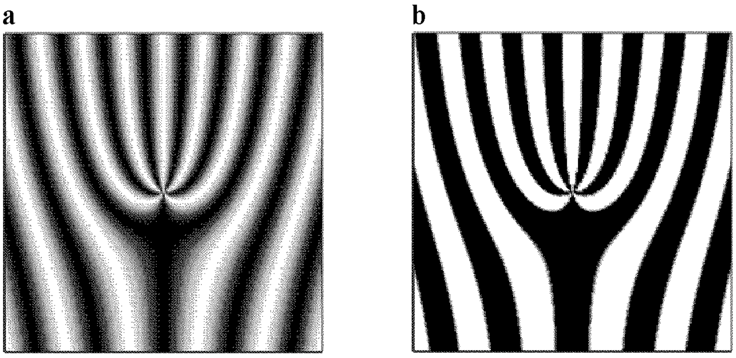

Fig. 3.2. Holograms printed using equations (3.7) (case a) and (3.8) (case b).
The OV charge is *m* = 5. The other parameters are as in Figures (3.1b) and (3.1d), respectively

So far, the off-axis holograms have been considered. The corresponding on-axis holograms can also be manufactured. Figure 3.3 shows examples of their fringe pattern. Such holograms have all the disadvantages common to on-axis holograms

[Goodman 1968] and are not widely used. In the book by Vasnetsov *et al.* (1999) transition from the pattern shown in Figure 3.3 to the patterns shown in Figure 3.1 or Figure 3.2 by the increase of the reference wave angle is studied in detail.

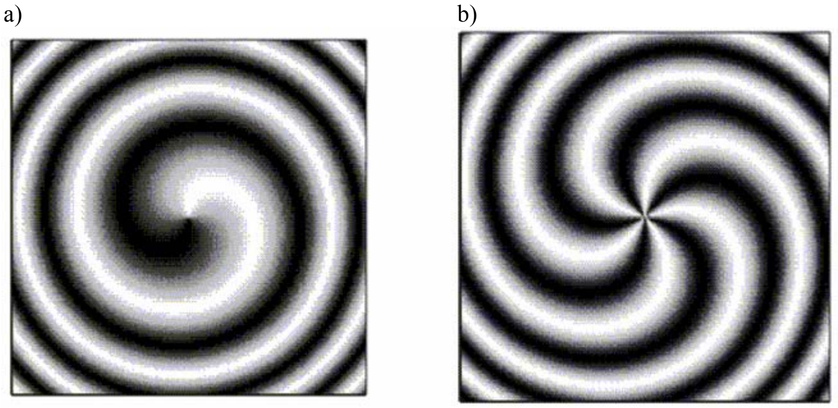

Fig. 3.3. The on-axis holograms generating optical vortex with a) charge $m = 1$ and b) $m = 5$. In the case of on-axis holograms even small wavefront curvature has visible influence on fringe geometry (contrary to off-axis case). For this reason the extra term $c(x^2 + y^2)$ $(c < 1)$ was added to the cosine argument in formulas (3.3) and (3.7). If $c = 0$ one gets a star like structure with straight arms. Formulas (3.4) and (3.8) cannot be used if the non-zero curvature of object wavefront is to be considered

3.2.2. OVs detection with interferometer

The obvious way to detect the OVs within the given beam is to use an interferometer. The interference pattern of a beam carrying OVs with a plane wave was calculated in section 3.2.1 devoted to the synthetic holograms; the hologram is in fact the interference pattern between the wavefront carrying OVs and plane wave. Figure 3.4 shows examples of interferograms obtained by the interference between the beams generated by the synthetic hologram shown in Figure 3.1d and the plane wave. The characteristic spiral (for the coaxial plane wave) and fork-like fringe (for the off-axis plane wave) indicates the presence of optical vortices in the reconstructed beam.

Apart from the interferometric techniques, there are some other methods for the OVs detection and analysis; however, they are rarely used. An example of such a method is the use of the cylindrical mode converter [Tamm *et al.* 1990b]. This method was used to demonstrate the switching between the states of opposite vortex helicity in laser beams. The OVs can also be detected using the correlation technique. This method uses the appropriate synthetic hologram for OVs generation as a matched filter [Heckenberg *et al.* 1992, Tang *et al.* 1994]. In addition to OVs detection, the method supports the way for the vortex charge recognition; however, it fails in OV localization. An important advantage of this method is that no reference beam or interferometric system is necessary. Another example is the use of the Shack–Hartmann detecting system, which is described in paper by Aksenov *et al.* (2002).

The other question is about the OVs localization in the interference field of three plane waves. Such OVs net is a base for a new interferometer presented in Chapter 4. In subsection 4.3, several methods are discussed for this purpose.

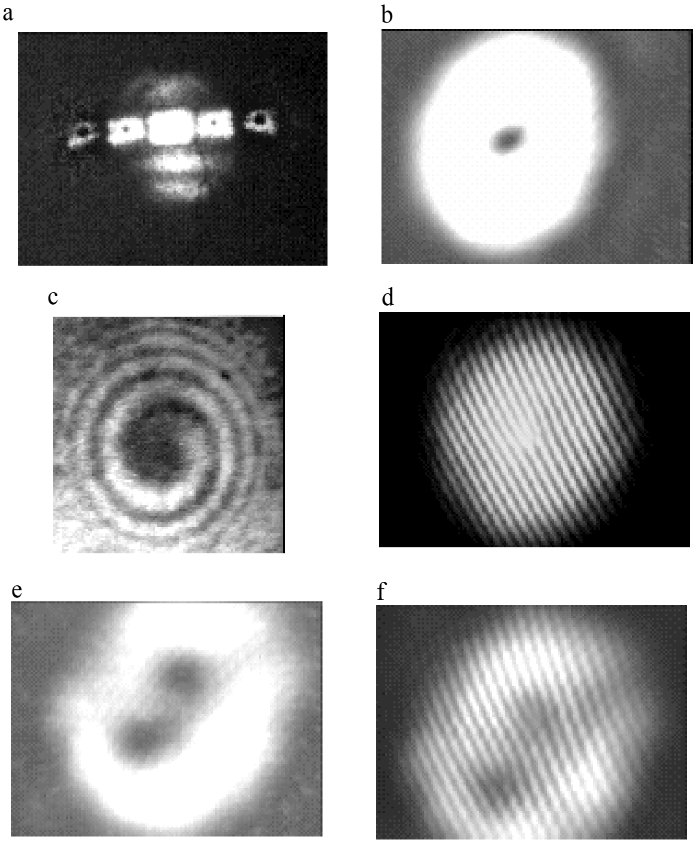

Fig. 3.4. Reconstruction of the hologram shown in Figure 3.1d.
a) illumination with expanded laser beam (the beam is wider than diffractive structure). The first and the second diffraction orders are visible; b) The first order diffraction beam (illumination with narrow Gaussian laser beam); c) The interferogram of the first order diffraction beam (Figure b) with coaxial plane wave. The characteristic spiral pattern is present; d) The interferogram of the same diffraction beam but with off-axial plane wave. The characteristic fork pattern is present; e) The second order diffraction beam. It contains two single OV, which get separated while propagating; f) the off-axis interferogram of the second order diffraction beam

3.2.3. Experiment

Standard computer printers were used to print hologram masks in the course of this experiment. In our experience [Przerwa-Tetmajer 2002] the best results are achieved by using an ink printer in color mode. In this mode, the foil is covered more uniformly than in black and white mode used in an ink or laser printer. The holograms that generate a multi-vortex beam were designed by simply fitting a few holograms generating a single OV. The masks were reduced optically twenty times and transferred onto a holographic plate with the devoted optical device. In this way, the amplitude holograms were manufactured. If necessary, the holograms were blazed using a bleaching technique. The blazed holograms have better diffraction efficiency.

If high quality holograms were needed one more step was applied. In order to get high fringe densities, the image obtained by low density synthetic holograms was used as an object in the classical holographic system. In this way, high density amplitude holograms were produced, with quasi-sinusoidal fringe geometry. The holograms manufactured in this way were sufficient for simple experiments and for demonstrations in student laboratory. Figures 3.4, 3.5 and 3.6 show examples of images obtained from such holograms.

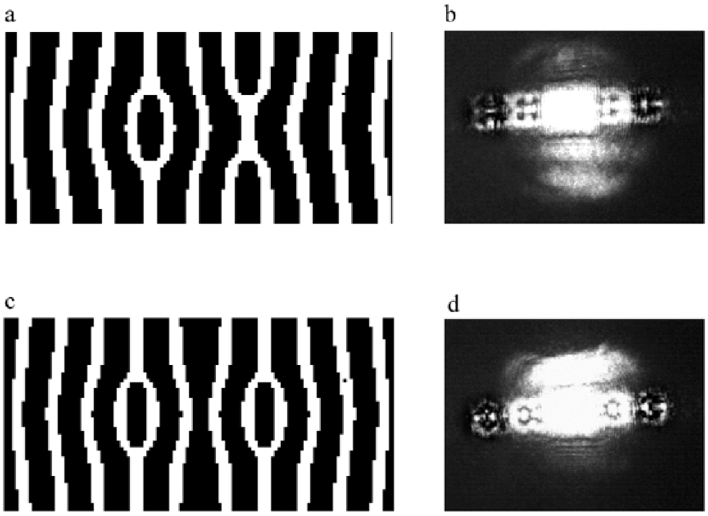

Fig. 3.5. a) Fringe pattern of hologram generating four vortices in quadruple geometry and its image shown in Figure b. In the image two diffraction orders are visible. In each order four dark spots indicate single optical vortices (multi-charge in order higher than first); c) Fringe pattern for four vortices generation in non-quadruple geometry and its image shown in Figure d. Images (b) and (d) were taken for the same distance between hologram and image plane. The non-quadruple geometry of OVs is less stable (they start to overlap) than the quadruple system. This shows that in some respect OVs behave like electrical charges [Bazhenov *et al.* 1992]

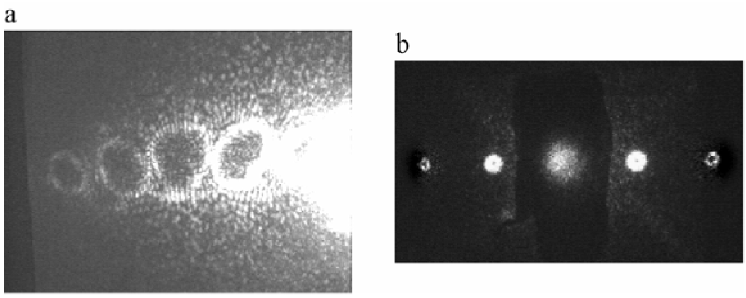

Fig. 3.6. a) The left side of the image generated by blazed hologram whose fringe pattern is shown in Figure 3.1.d. Five diffraction orders are visible; b) The image of hologram that was registered from the hologram shown in Figure 3.1d, as is described in the text. Weak image of the secondary order beams shows that the obtained hologram is quasi-sinusoidal. Contrast of the second order beam was improved for printing

3.2.4. Image evaluation

In most cases, the image reconstructed from synthetic holograms cannot be calculated analytically. Moreover, for the number of cases that can be studied analytically, the final formulas are too complicated to give any insight regarding image structure. Nevertheless, analytical results can be still useful for testing the numerical methods. In paper by Masajada (1999), the testing of a simple numerical procedure for the evaluation of images reconstructed from holograms was reported. The test hologram shown in Figure 3.7 was a simplified version of the hologram shown in Figure 3.1d. The simplification allows the direct use of the Fresnel diffraction integral (2.7).

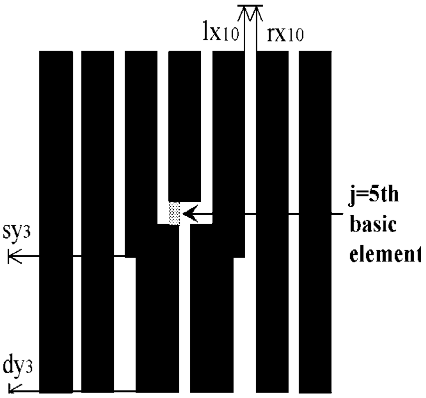

Fig. 3.7. Simplified hologram

The simplified hologram produces OVs (Fig. 3.8). By comparing the results obtained analytically and by numerical integration, the accuracy of numerical algorithms can be investigated for diffractive elements that generate OVs.

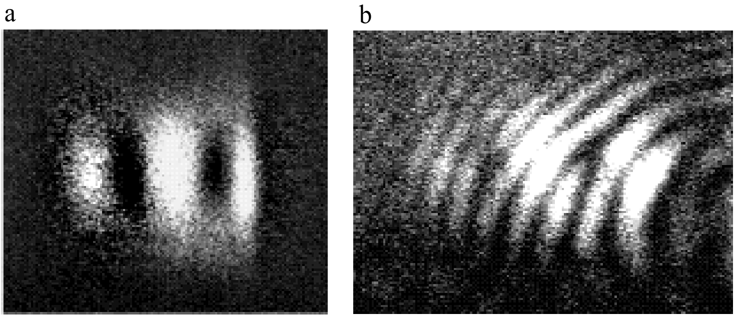

Fig. 3.8. The first order diffraction beam obtained from the simplified hologram shown in Figure 3.7. a) the intensity image; b) the off-axis interferogram

In order to analytically calculate the image from the hologram the latter was divided into rectangular (basic) elements, as shown in Figure 3.7. Each basic element is described by a product of two rectangular functions

$$\Pi\left(\frac{x - center_x}{width_x}\right)\Pi\left(\frac{y - center_y}{width_y}\right), \tag{3.9}$$

where $center_x$, $center_y$ are coordinates of mass center of the given basic element along x and y axes, respectively, and $width_x$, $width_y$ are corresponding widths. Calculating the integral (2.7) for the j-th basic element leads to the formula (assuming the illumination by monochromatic coaxial plane wave)

$$UR_j = \frac{\sin(2kz)}{\pi} FA_j + \frac{\cos(2kz)}{\pi} FB_j, \tag{3.10a}$$

$$UI_j = \frac{\sin(2kz)}{\pi} FB_j - \frac{\cos(2kz)}{\pi} FA_j, \tag{3.10b}$$

where

$$FA_j = \frac{\sqrt{2\pi}}{2}\left\{\begin{aligned} &[\mathrm{Ci}(\xi rx_j) - \mathrm{Ci}(\xi lx_j)]\,[\mathrm{Ci}(\xi sy_j) - \mathrm{Ci}(\xi dy_j)] \\ &+ [\mathrm{Si}(\xi rx_j) - \mathrm{Si}(\xi lx_j)]\,[\mathrm{Si}(\xi sy_j) - \mathrm{Si}(\xi dy_j)] \end{aligned}\right\}, \tag{3.10c}$$

$$FB_j = -\frac{\sqrt{2\pi}}{2}\left\{\begin{aligned} &[\mathrm{Si}(\xi rx_j) - \mathrm{Si}(\xi lx_j)]\,[\mathrm{Ci}(\xi sy_j) - \mathrm{Ci}(\xi dy_j)] \\ &+ [\mathrm{Ci}(\xi rx_j) - \mathrm{Ci}(\xi lx_j)]\,[\mathrm{Si}(\xi sy_j) - \mathrm{Si}(\xi dy_j)] \end{aligned}\right\}, \tag{3.10d}$$

Ci, Si are Fresnel cosine and sine integrals [Goodman 1968], $\xi = \sqrt{2/\pi}$, lx_j, rx_j are left and right limits of the j-th basic element, sy_j, d_{yj} are up and down limits of the j-th element (Fig. 3.7).

The total complex amplitude at image point P for the simplified hologram can be expressed as

$$U(P) = \sum_{j=1}^{N} (UR_j + iUI_j) , \tag{3.11}$$

where N is a number of basic elements.

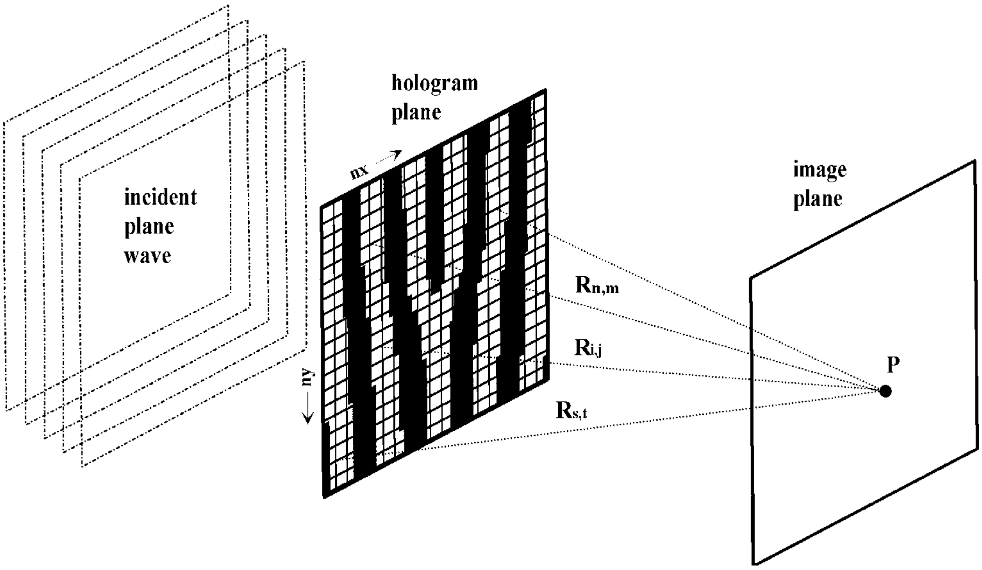

Fig. 3.9. The scheme for numerical calculations
of the hologram image at the given point P

The numerical calculations were performed along the scheme illustrated in Figure 3.9. The real and imaginary parts of light complex amplitude were calculated from the formulas [Masajada *et al.* 1994]

$$UR(P) = \sum_{i=1}^{n_x} \sum_{j=1}^{n_y} \cos(kR(P)_{i,j}) , \tag{3.12a}$$

$$UI(P) = \sum_{i=1}^{n_x} \sum_{j=1}^{n_y} \sin(kR(P)_{i,j}) . \tag{3.12b}$$

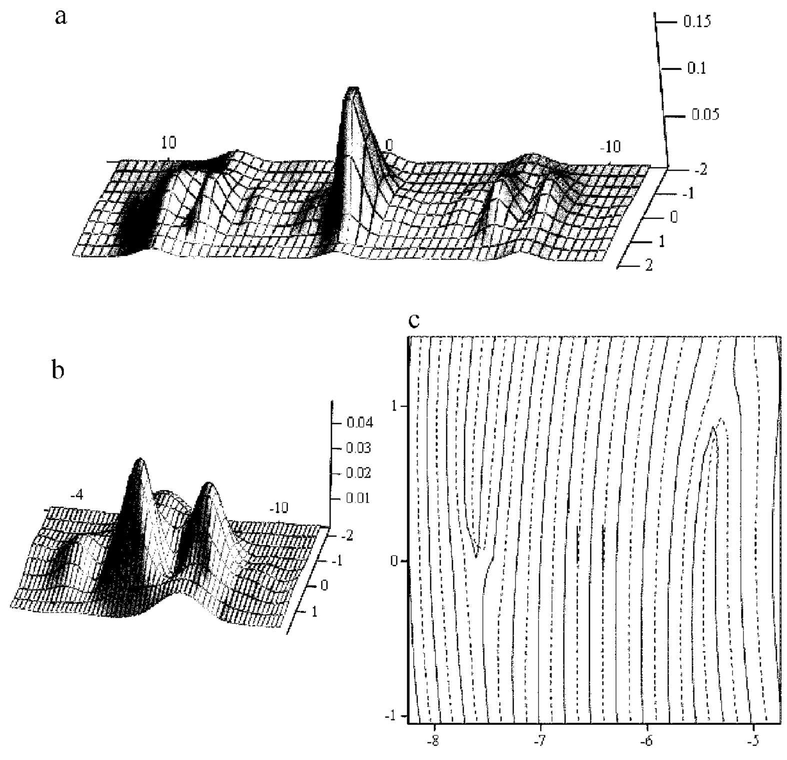

Fig. 3.10. Image of hologram shown in Figure 3.7 reconstructed with plane wave – analytical calculations. a) General view (zero and first diffraction orders); b) The view on first diffraction maximum; c) The plot of lines Re(U) = 0 (solid) and Im(U) = 0 (dashed). Intersection points determine the singular point position

Figure 3.10 shows the result obtained after analytical calculations for the simplified hologram shown in Figure 3.7. Figure 3.11 shows the plot of lines Re(U) = 0 and Im(U) = 0 obtained for the same hologram after numerical calculations. As expected (see the interferogram in Figure 3.8b), two OVs are presented in each figure; their location and local line geometry are similar. Small differences are caused by two different ways of hologram sampling for numerical and analytical calculations, meaning that the simple numerical algorithm preserves the existence, location and local structure of the OVs, at least with the same accuracy as calculations performed by the Fresnel diffraction integral. Figure 3.12 shows the numerical results for the hologram shown in Figure 3.1b. To preserve the sinusoidal character of amplitude part of hologram transfer function, formulas (3.12) were transformed to the form

$$UR(P) = \sum_{i=1}^{n_x} \sum_{j=1}^{n_y} A_{i,j} \cos(kR(P)_{i,j}), \tag{3.13a}$$

$$UI(P) = \sum_{i=1}^{n_x} \sum_{j=1}^{n_y} A_{i,j} \sin(kR(P)_{i,j}), \qquad (3.13b)$$

where $A_{i,j}$ is the pseudoamplitude (i.e. absolute value of the amplitude) at the *i*, *j* point *P* in hologram plane multiplied by hologram amplitude transfer function. The calculated images of the first order diffraction beams contain single zero amplitude points in their centers (Fig. 3.12). There is no image of the second order diffraction beam as is expected for such holograms. The light intensity around the single OV has an almost circular symmetry; however, the influence of the rectangular geometry of the whole hologram is still visible.

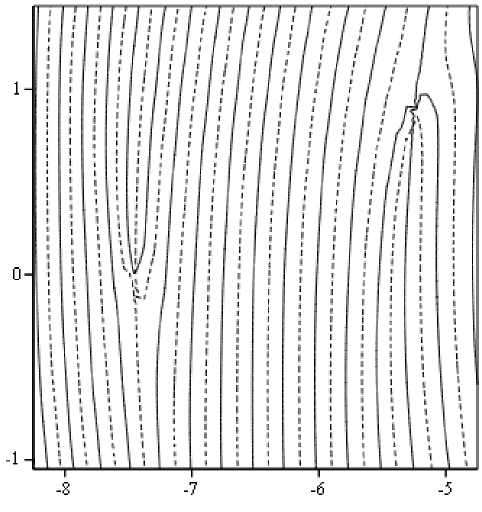

Fig. 3.11. The plot of lines Re(U) = 0 (solid) and Im(U) = 0 (dashed). The intersection points determined the singular point. Numerical calculations for hologram shown in Figure 3.7

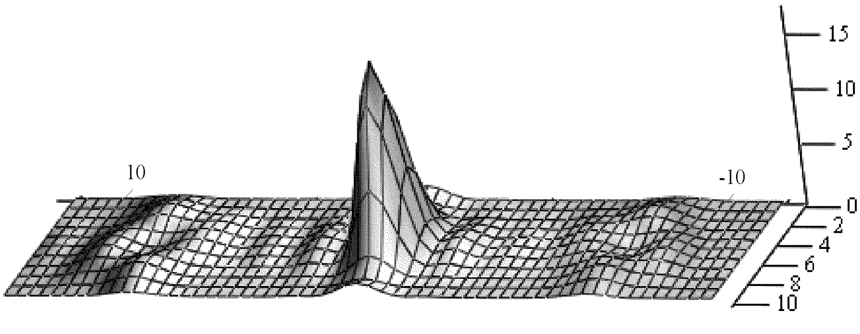

Fig. 3.12. The intensity of hologram shown in Figure 3.1b and calculated with formulas 3.13a and 3.13b

It was not the author's aim to consider all aspects of the holographic methods used for OVs generation. Although many issues have been omitted, some of them should at least be mentioned. Roux (1993a, b) has designed similar structures in the search for holograms that perform the rotation transformation. He expanded upon Bryngdhal's work (see, for example Bryngdhal (1974)) devoted to the theory that allows the design of holographic elements that perform a desired optical transformation. An example of such a hologram calculated by Przerwa-Tetmajer (2002) is given in Figure (3.13).

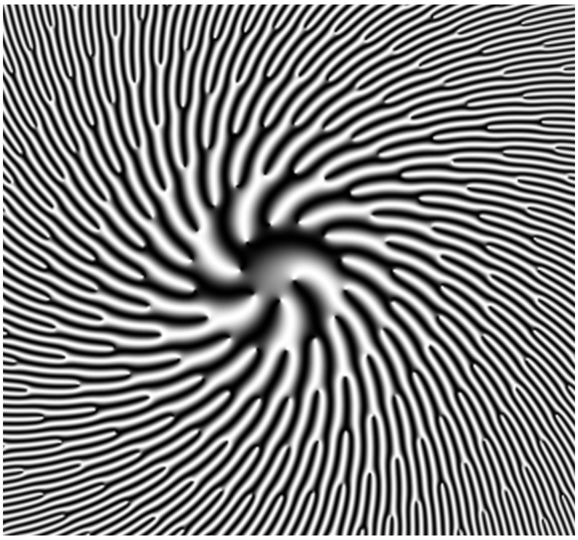

Fig. 3.13. Fringe geometry of the hologram performing rotation transformation [Roux 1993a,b, Przerwa-Tetmajer 2002]

Interesting considerations were presented in a paper by Abramochkin *et al.* (1993), where spiral beams with arbitrary intensity distribution and holograms generating such beams were studied. The book by Soifer and Golub (1994) completely covers the problem of designing holograms, which reproduce the desired laser modes. In a series of papers Brand studied (1997, 1998a,b, 1999a,b) the holographic generation, detection and properties of wavefronts with phase singularities at millimeter wavelengths. At the end of this section, it is worth emphasizing that the holographic method is very flexible and many design tools for making synthetic holograms are in use. Moreover, the high quality manufacturing technology is readily available. One may expect that the interest in holographic methods for generation of phase singularities will increase in the future and a number of new works in this area can be expected.

3.3. OVs generation by three plane waves interference

A regular net of OVs can be generated by the interference of plane waves. A brief comment on it was given by Rozanov (1993). In the paper by Angelsky *et al.* (1997), the OVs generation by two plane waves (plane waves in particular) is briefly studied. The obvious conditions for an isolated zero light amplitude at point *P* are

$$\varphi_A(P) = \varphi_B(P) \pm \pi\,, \qquad (3.14a)$$

$$U_A(P) = U_B(P)\,, \qquad (3.14b)$$

where φ_A, φ_B, U_A, U_B are phases and amplitudes of interfering waves *A*, *B*, respectively.

When both waves are plane, the conditions (3.14) can be met (at an isolated point) if the amplitude of one (or two waves) is inhomogeneous. Thus, the method proposed by Angelsky requires special filters for amplitude modulations. Masajada *et al.* (2001) studied the generation of OVs net by three homogeneous plane waves interference. Such a net is a base for an interferometer in which the optical vortices are used for phase determination. This issue is discussed in more detail below.

3.3.1. Three plane waves interference – global view

The interference of three plane waves produces a regular net of single OVs which can be used in optical metrology. The schematic representation of the field produced by three plane waves interference is shown in Figure 3.13. There are isolated points where CAVs of interfering waves form a triangle, provided their lengths satisfy the triangle condition. The single OV exists at each such point. There are two kinds of such triangles, which correspond to two possible signs of OV topological charge. The regularity of the OVs net, shown in Figure 3.14, results from the regularity of the interfering waves.

In Figure 3.14, the wave A propagates perpendicularly to the observation plane, so its phase is constant over this plane. The general case (when all waves are tilted with respect to the observation plane) can be transformed to this one without changing the OVs position. At each point of the observation plane each CAV can be rotated through an angle equal to the phase of a tilted wave A (Fig. 3.15).

$$\phi_{q'} = \phi_q - \phi_a\,, \qquad (3.15)$$

where ϕ_q is the phase distribution of a given plane wave in the observation plane $q \in (A,B,C)$. Thus, the wavefront *A* transforms to wavefront A', which is parallel to the observation plane. Using the transformation (3.15), the transformed plane wave can be written as

$$U'_q = U_0 \exp\{-i[(k_{qx} - k_{ax})x + (k_{qy} - k_{ay})y + (k_{qz} - k_{az})z + \psi_{q0}]\}. \qquad (3.16)$$

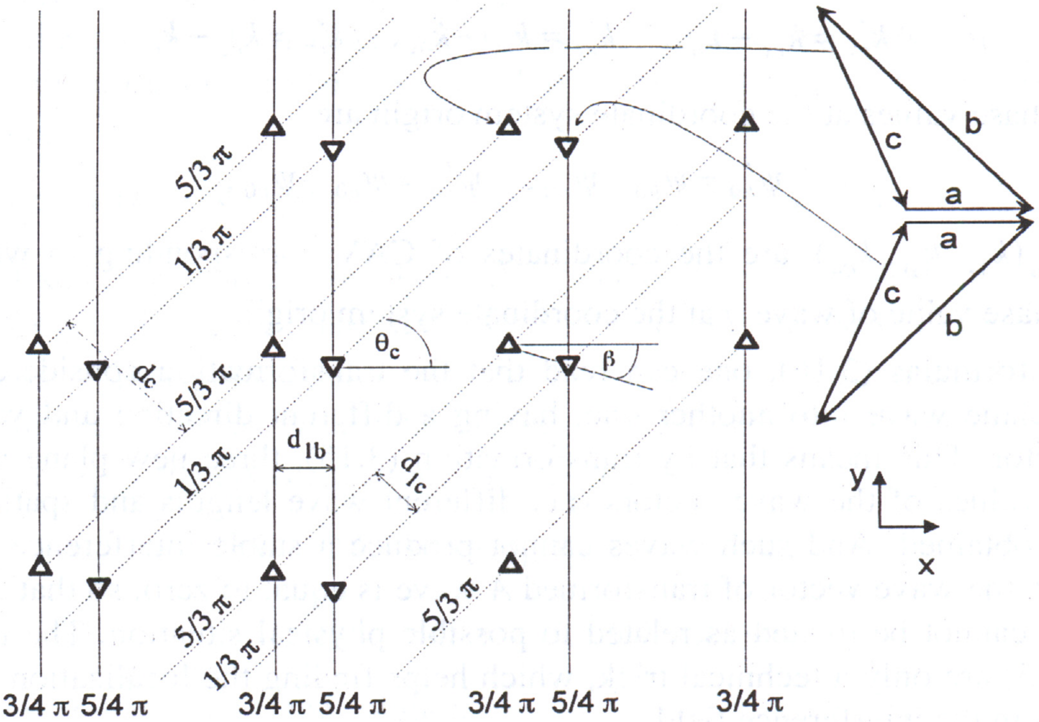

Fig. 3.14. Phase distribution of three interfering plane waves. Plane wave *A* is parallel to the plane of observation, which is the plane of the figure. Plane wave *B* has the wave vector $\mathbf{k}_b(0.01k, 0, 0.99995k)$ (its equiphase lines are parallel to *y*-axis). The $\mathbf{k}_c$ wave vector is $\mathbf{k}_c(0.01k, 0.01k, 0.99990k)$. The up-oriented triangles mark points where the negative OVs are placed while the down-oriented triangles mark points for the positive OVs. **a**, **b**, **c**, are CAVs of the waves *A*, *B*, *C*, respectively

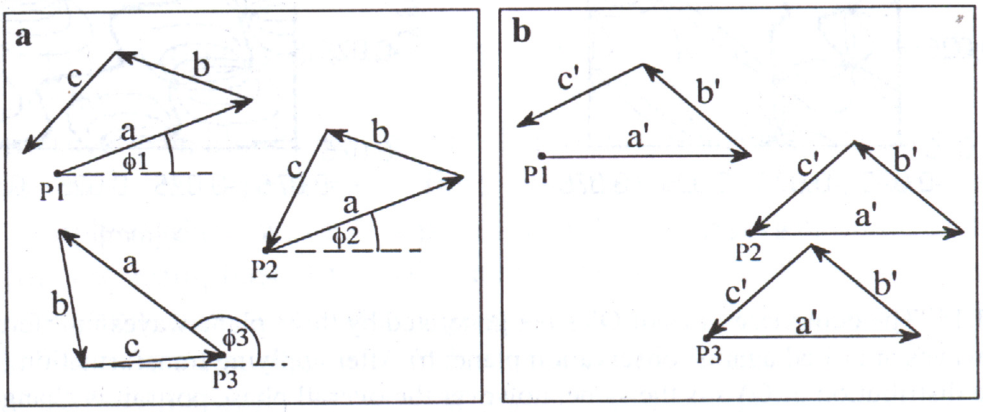

Fig. 3.15. At each point (*P*1, *P*2, *P*3) of the observation plane there are three CAVs representing the interfering waves. At each point all the CAVs rotate at angles (ϕ1, ϕ2, ϕ3) corresponding to phase of the wave *A*. Such transformation cannot change the angles between CAVs; a) before rotation; b) after rotation

Hence the other waves B and C transform to plane waves B' and C' with wave vectors given by

$$k'_{bx} = k_{bx} - k_{ax}\,, \quad k'_{by} = k_{by} - k_{ay}\,, \quad k'_{bz} = k_{bz} - k_{az}\,, \tag{3.16a}$$

$$k'_{cx} = k_{cx} - k_{ax}\,, \quad k'_{cy} = k_{cy} - k_{ay}\,, \quad k'_{cz} = k_{cz} - k_{az}\,. \tag{3.16b}$$

The phase values at the coordinate system origin are

$$\psi'_{b0} = \psi_{b0} - \psi_{a0}\,, \quad \psi'_{c0} = \psi_{c0} - \psi_{c0}\,, \tag{3.17}$$

where $\mathbf{k}_q(k_{qx}, k_{qy}, k_{qz})$ are the coordinates of CAV corresponding to wave q, and ψ_{q0} is phase value of wave q at the coordinate system origin.

From formulas (3.16), one can read that the transformation considered changes a given plane wave into another one, having a different direction and value of the wave vector. This means that by transformation (3.15), three new plane waves with different values of the wave vectors (i.e. different wave lengths and spatial frequencies) are obtained. And such waves cannot produce a stable interference pattern. In particular, the wave vector of transformed A wave is equal to zero, so that the new set of waves cannot be treated as related to possible physical situation. The transformations (3.15) are only a technical trick, which helps finding the localization of the vortex points in the interference field.

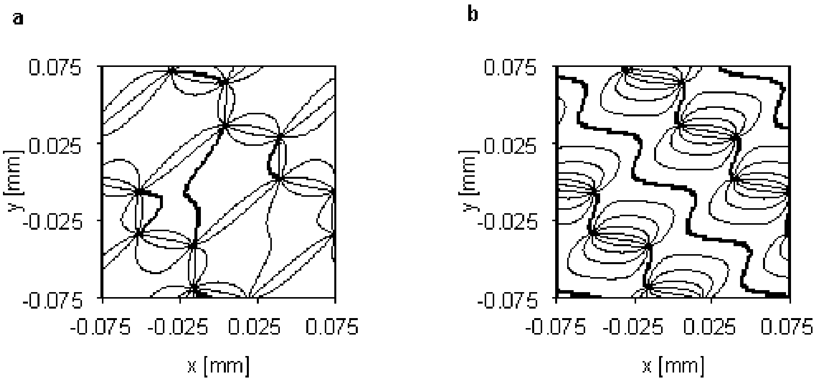

Fig. 3.16. The equiphase lines of OVs net generated by three plane waves interference. a) All waves are tilted against observation plane; b) After applying transformation (3.15). The distribution of OVs is the same, however the overall phase portrait is changed

The transformation (3.15) can be applied for a much wider class of problems. Any set of any waves can be transformed in this way without changing the OVs distribution. Moreover, the distribution of the rotation angle over the whole observation plane does not have to meet any condition (such as continuos condition), but the rotation angle must be the same for all CAVs seeded at a given point of the observation plane. This fact gives more freedom in analyzing the OVs distribution in a field generated by waves interference. It should be noted here that the transformation (3.15) changes the local phase portrait of each OV (Fig. 3.16).

Now, using the transformation (3.15) it is easy to find the OVs trajectories. Assuming that the observation plane is shifted at distance Δz along the z-axis, formula (3.16) becomes

$$U'_q = U_0 \exp\{-i[(k_{qx} - k_{ax})x + (k_{qy} - k_{ay})y + (k_{qz} - k_{az})(z + \mathit{\Delta} z) + \psi'_{q0} - \psi'_{a0}]\}\,. \quad (3.18)$$

For the fixed (x, y) coordinates the CAV of wave A' rotates while the observation plane shifts by angle $k'_{az}\,\Delta z$. The same shift must occur for the CAVs of waves B' and C' at the vortex points (otherwise the CAVs would not form triangles). If the (x, y) coordinate of vortex point will change from the initial position (x_i, y_i) to the final position (x, y) then two equations can be written

$$(x - x_i)\,k'_{bx} + (y - y_i)\,k'_{by} + \Delta z\, k'_{bz} = 0\,, \quad (3.18b)$$

$$(x - x_i)\,k'_{cx} + (y - y_i)\,k'_{cy} + \Delta z\, k'_{cz} = 0\,. \quad (3.18c)$$

This set of equations has the solution

$$x = \frac{k'_{cz}\,k'_{by} - k'_{cy}\,k'_{bz}}{k'_{bx}\cdot k'_{cy} - k'_{cx}\cdot k'_{by}}\,\Delta\, z + \frac{k'_{cy}\,k'_{bz} - k'_{cz}\,k'_{by}}{k'_{bx}\cdot k'_{cy} - k'_{cx}\cdot k'_{by}}\,x_i\,, \quad (3.19a)$$

$$y = \frac{k'_{bz}\,k'_{cx} - k'_{bx}\,k'_{cz}}{k'_{bx}\cdot k'_{cy} - k'_{cx}\cdot k'_{by}}\,\Delta\, z + \frac{k'_{bx}\,k'_{cy} - k'_{by}\,k'_{cx}}{k'_{bx}\cdot k'_{cy} - k'_{cx}\cdot k'_{by}}\,y_i\,. \quad (3.19b)$$

The OVs propagation is described by a linear function of z, so they propagate along straight lines.

By geometrical consideration, one can derive a number of relations describing the OVs distribution in the interference field obtained with three plane waves. This is particularly simple if plane wave A is parallel to the observation plane and the y-axis is oriented along the equiphase lines of wave B (Fig. 3.14). Using the transformation (3.15), these relations can describe any geometry of optical vortices generated by three plane waves. There is a list of a few of them shown in Figure 3.14.

The angle between equiphase lines of wave C and x-axis is

$$\theta_c = \text{atan}\left(-\frac{k_{cx}}{k_{cy}}\right). \quad (3.20a)$$

The distance between two subsequent equiphase lines of wave *B* or *C* is

$$d_q = \frac{2\pi}{\sqrt{k^2 - k_{qz}^{\ 2}}}. \tag{3.20b}$$

The distance between two different equiphase lines of wave *B* or *C* belonging to the twins OVs is

$$d1_q = \frac{\Delta\Psi_q}{2\pi} d_q. \tag{3.20c}$$

Here, $\Delta\Psi_q$ is

$$\Delta\Psi_q = |\Psi 1q - \Psi 2q|, \tag{3.20.d}$$

where angles $\Psi 1q$ are shown in Figure 3.17 and $\Psi 2q$ are the corresponding angles for the twin OV. The mutual relations between these angles and triangle angles $\gamma_a, \gamma_b, \gamma_c$ are expressed by the formulas:

$$\Psi 1b = \pi - \gamma_c, \quad \Psi 1c = \pi + \gamma_b, \tag{3.20e}$$

$$\Psi 2b = 2\pi - \Psi 1b, \quad \Psi 2c = 2\pi - \Psi 1c. \tag{3.20f}$$

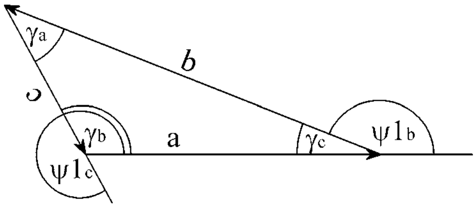

Fig. 3.17. The triangle formed from CAV vectors (at vortex point)

The angle between the line joining two twins OVs and the *X*-axis is

$$\tan(\beta) = \mathrm{sign}(k_y)\frac{d1_c}{d1_b}(\cos(\theta) - \tan(\theta)). \tag{3.20g}$$

3.3.2. Three plane waves interference – local picture

The phase portrait of a three plane wave interferogram is sensitive to the transformation (3.15) and it cannot be applied for local analysis. In Figure 3.18a, a small circle of radius ρ plotted around the chosen OV is shown. Figure 3.18b shows a plot of complex amplitude vector coordinates v_x, versus v_y of the total field while moving along the circle shown in Figure 3.18a. The plot of v_x versus v_y forms a closed curve (for small ρ) (Fig. 3.18b), as should be expected. The additional loop appears for ρ large enough. This happens because in such a case, the circle in Figure 3.18a encloses one vortex point and a neighboring saddle point. Figure 3.18c shows the plot for a circle that encloses the number of saddle and vortex points. To plot Figure 3.18b, the origin of a local coordinate system should be shifted to the position of a chosen OV. The corresponding translation vector $\mathbf{T}(T_x, T_y)$ can be calculated as follows: first, by applying transformation (3.15) one can change the given plane waves A, B, C to plane waves A', B', C' where wave A' has a uniform phase over the plane of interest. Because the transformation does not change the OVs distribution (in the fixed plane of interest) one can use this simplest case to find the transformation vector.

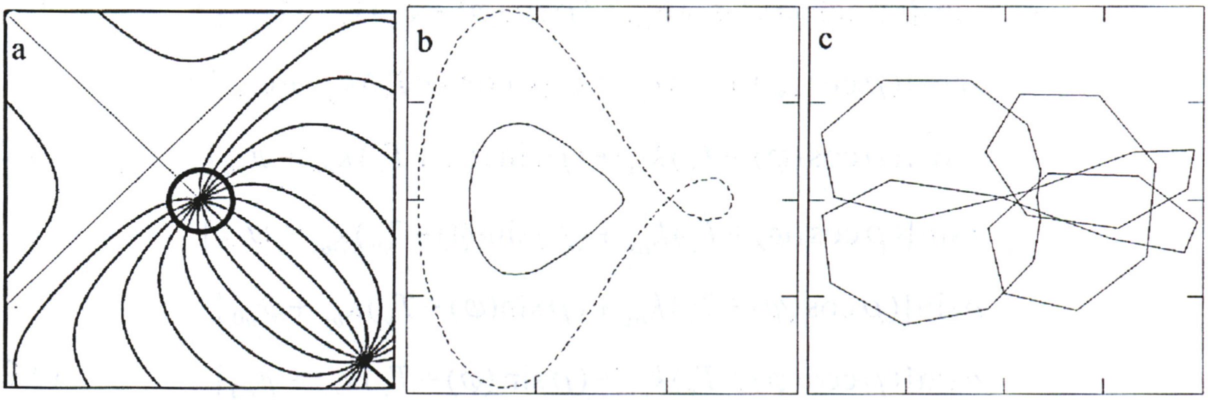

Fig. 3.18. a) Circle of radius ρ surrounding a given optical vortex (represented by the convergence point of equiphase lines); b) The plot of v_x versus v_y (vertical and horizontal axes, respectively) while tracing the circle shown in figure (a) – Curve with a loop (dotted line) is plotted for a circle of given radius ρ. Closed curve, free of loops, (solid line) is plotted with radius $\rho/5$; c) Multi-loop plot for the circle radius equal 10ρ

Let phases of waves B', C' at the vortex point be (modulo 2π) ψ'_{1b}, ψ'_{1c} (or ψ'_{2b}, ψ'_{2c}). At the vortex points, the following relations hold

$$x \cdot k'_{bx} + y \cdot k'_{by} + \psi'_{b0} = \psi'_{1b} + 2\pi n, \tag{3.21a}$$

$$x \cdot k'_{cx} + y \cdot k'_{cy} + \psi'_{c0} = \psi'_{1c} + 2\pi n, \tag{3.21b}$$

where n is an integer number and the prime variables refer to the parameters of the transformed waves (see formulas (3.16 and 3.17)).

The above set of equations has the solution for translation vectors of the form

$$T_x = \frac{k'_{cy}(\psi'_{1b} - \psi'_{b0} + 2\pi n) - k'_{by}(\psi'_{1b} - \psi'_{b0} + 2\pi n)}{k'_{bx}k'_{cy} - k'_{by}k'_{cx}}, \tag{3.22a}$$

$$T_y = \frac{k'_{bx}\,(\psi'_{1c} - \psi'_{c0} + 2\pi\, n) - k'_{cx}\,(\psi'_{1b} - \psi'_{b0} + 2\pi\, n)}{k'_{bx}\, k'_{cy} - k'_{by}\, k'_{cx}}\,. \tag{3.22b}$$

To derive expressions (3.22), the following formula for the phase value at the observation plane of the given plane wave (i.e. from plane wave B or C) was used

$$\psi(x,y)_b = x \cdot k_{bx} + y \cdot k_{by} + \psi_{b0}\,, \tag{3.23a}$$

$$\psi(x,y)_c = x \cdot k_{cx} + y \cdot k_{cy} + \psi_{c0}\,, \tag{3.23b}$$

where (x, y) are coordinates in the observation plane.

It is also advisable to use the polar coordinates (ρ,φ). The formulas for CAV coordinates (of the total wavefront) take the following form

$$\begin{aligned} v_x = {} & \cos[(\rho\cos(\varphi) + T_x)\, k_{ax} + (\rho\sin(\varphi) + T_y)\, k_{ay} + \psi_{a0}] + \\ & b\cos[(\rho\cos(\varphi) + T_x)\, k_{bx} + (\rho\sin(\varphi) + T_y)\, k_{by} + \psi_{b0}] + \\ & c\cos[(\rho\cos(\varphi) + T_x)\, k_{cx} + (\rho\sin(\varphi) + T_y)\, k_{cy} + \psi_{c0}]\,, \end{aligned} \tag{3.24a}$$

$$\begin{aligned} v_y = {} & \sin[(\rho\cos(\varphi) + T_x)\, k_{ax} + (\rho \cdot \sin(\varphi) + T_y)\, k_{ay} + \psi_{a0}] \\ & b\sin[(\rho\cos(\varphi) + T_x)\, k_{bx} + (\rho\sin(\varphi) + T_y)\, k_{by} + \psi_{b0}] + \\ & c\sin[(\rho\cos(\varphi) + T_x)\, k_{cx} + (\rho\sin(\varphi) + T_y)\, k_{cy} + \psi_{c0}]\,. \end{aligned} \tag{3.24b}$$

In this chapter, it is assumed that the amplitude of the wave A is normalized to unity. Thus, the amplitudes of the other two waves B, C can be recomputed proportionally and the whole phase and amplitude pattern of interfering waves A, B, C will not change.

Now the local structure of phase in the vicinity of a given vortex point is analyzed; so that the radius ρ can be made as small as necessary and the following approximations can be applied

$$\sin\alpha = \alpha\,, \tag{3.25a}$$

$$\cos\alpha = 1\,. \tag{3.25b}$$

After expanding the functions sine and cosine, applying the above approximations and neglecting terms with ρ^2 one gets

$$\begin{aligned} v_x = {} & (-k_{ax}\sin T_{\psi a} - b\, k_{bx}\sin T_{\psi b} - c\, k_{cx}\sin T_{\psi c})\,\rho\cos\varphi + \\ & (-k_{ay}\sin T_{\psi a} - b\, k_{by}\sin T_{\psi b} - c\, k_{cy}\sin T_{\psi c})\,\rho\sin\varphi + \\ & \cos T_{\psi a} + b\cos T_{\psi b} + c\cos T_{\psi c}\,, \end{aligned} \tag{3.26a}$$

$$v_y = (k_{ax}\cos T_{\psi a} + b\,k_{bx}\cos T_{\psi b} + c\,k_{cx}\cos T_{\psi c})\,\rho\cos\varphi + (k_{ay}\cos T_{\psi a} + b\,k_{by}\cos T_{\psi b} + c\,k_{cy}\cos T_{\psi c})\,\rho\sin\varphi + \sin T_{\psi a} + b\sin T_{\psi b} + c\sin T_{\psi c}\ , \tag{3.26b}$$

where

$$T_{\psi a} = T_x\,k_{ax} + \psi_{a0}\,,\quad T_{\psi b} = T_x\,k_{bx} + \psi_{b0}\quad \text{and}\quad T_{\psi c} = T_x\,k_{cx} + T_y\,k_{cy} + \psi_{c0}\,. \tag{3.26c}$$

Following the interpretation of the translation vector, one gets (3.21, 3.22)

$$\cos T_{\psi a} + b\cos T_{\psi b} + c\cos T_{\psi c} = 0 \quad \text{and} \quad \sin T_{\psi a} + b\sin T_{\psi b} + c\sin T_{\psi c} = 0$$

hence

$$v_x = (-k_{ax}\sin T_{\psi a} - b\,k_{bx}\sin T_{\psi b} - c\,k_{cx}\sin T_{\psi c})\,\rho\cos\varphi + (-k_{ay}\sin T_{\psi a} - b\,k_{by}\sin T_{\psi b} - c\,k_{cy}\sin T_{\psi c})\,\rho\sin\varphi\,, \tag{3.26d}$$

$$v_y = (k_{ax}\cos T_{\psi a} + b\,k_{bx}\cos T_{\psi b} + c\,k_{cx}\cos T_{\psi c})\,\rho\cos\varphi + (k_{ay}\cos T_{\psi a} + b\,k_{by}\cos T_{\psi b} + c\,k_{cy}\cos T_{\psi c})\,\rho\sin\varphi\,. \tag{3.26e}$$

The above formulas can be written in the form

$$v_x = b1_x\cos(\varphi) + b2_x\sin(\varphi)\,, \tag{3.27a}$$

$$v_y = b1_y\cos(\varphi) + b2_y\sin(\varphi)\,, \tag{3.27b}$$

where

$$b1_x = (-k_{ax}\sin T_{\psi a} - b\,k_{bx}\sin T_{\psi b} - c\,k_{cx}\sin T_{\psi c})\,\rho\,, \tag{3.28a}$$

$$b2_x = (-k_{ay}\sin T_{\psi a} - b\,k_{by}\sin T_{\psi b} - c\,k_{cy}\sin T_{\psi c})\,\rho\,, \tag{3.28b}$$

$$b1_y = (k_{ax}\cos T_{\psi a} + b\,k_{bx}\cos T_{\psi b} + c\,k_{cx}\cos T_{\psi c})\,\rho\,, \tag{3.28c}$$

$$b2_y = (k_{ay}\cos T_{\psi a} + b\,k_{by}\cos T_{\psi b} + c\,k_{cy}\cos T_{\psi c})\,\rho\,. \tag{3.28d}$$

Let

$$b1_x = B_x\cos(\psi_x) \quad \text{and} \quad b2_x = B_x\sin(\psi_x)\,, \tag{3.29a}$$

$$b1_y = B_y\sin(\psi_y) \quad \text{and} \quad b2_y = B_y\cos(\psi_y)\,. \tag{3.29b}$$

The above is true if the following conditions hold

$$B_x = \sqrt{b1_x^2 + b2_x^2} \quad \text{and} \quad \tan(\psi_x) = \frac{b2_x}{b1_x}, \tag{3.30a}$$

$$B_y = \sqrt{b1_y^2 + b2_y^2} \quad \text{and} \quad \tan(\psi_y) = \frac{b1_y}{b2_y}. \tag{3.30b}$$

Combining (3.29) and (3.27) gives

$$v_x = B_x \cos(\psi_x)\cos(\varphi) + B_x \sin(\psi_x)\sin(\varphi) = B_x \cos(\varphi - \psi_x), \tag{3.31a}$$

$$v_y = B_y \sin(\psi_y)\cos(\varphi) + B_y \cos(\psi_y)\sin(\varphi) = B_y \sin(\varphi + \psi_y). \tag{3.31b}$$

This can be written in the form

$$v_x = B_x \cdot \cos(\varphi), \tag{3.32a}$$

$$v_y = B_y \cdot \cos(\varphi + \delta), \tag{3.32b}$$

where δ is described as

$$\delta = \psi_x + \psi_y - \frac{\pi}{2}. \tag{3.33}$$

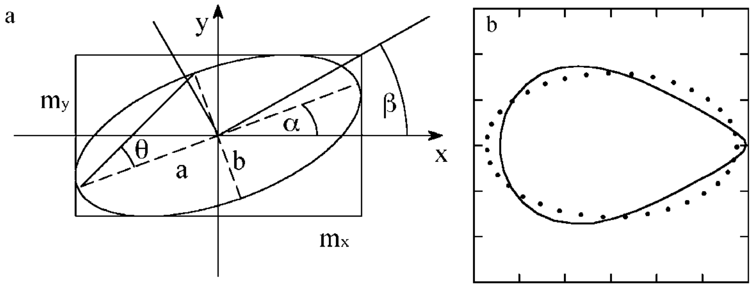

Fig. 3.19. a) Schematic picture of an ellipse representing local phase picture in local coordinate system of single vortex point; b) The plot of the ellipse, in the case of the circle shown in Figure 3.18a with radius $\rho/5$ (dotted line). The solid line plot shows an exact plot

The local representation (3.32) is similar to the light polarization state description by polarization ellipse [Azzam 1977] (Fig. 3.19a); however, it was derived in a local coordinate system (see the comments following equation (3.24)). Figure 3.19b shows a plot of the ellipse for the small radius of circle shown in Figure 3.18b. The relations between parameters m_x, m_y, α, β, θ, a, b are the same as for polarization ellipse and can be found in most of the publications concerning polarization (see, e.g., Azzam (1977), Ratajczyk (2000)). For example, the following formula can be derived

$$\sin 2\vartheta = \sin 2\beta \sin\delta \,. \tag{3.34}$$

The above relations contain a number of trigonometric functions in various combinations, meaning that the use of these relations for finding three plane waves that generates OVs, which have specific local phase geometry may be a hard task. Nevertheless, some interesting cases can easily be found. For example, three plane waves configuration which produces a locally symmetrical phase distribution can be found. In such a case, the ellipse in Figure 3.19 becomes a circle and the following conditions must be satisfied

$$B_x = B_y \quad \text{and} \quad \delta = \frac{\pi}{2}. \tag{3.35}$$

Combining these conditions with expressions (3.30) and (3.33) gives

$$b1_x = b2_y \quad \text{and} \quad b1_y = -b2_x\,. \tag{3.36}$$

The above set of equations is over-determined. Thus, there are infinite combinations of wave parameters which produce the desired phase distribution. To make the problem more uniquely defined, the following values are taken arbitrarily: the amplitudes of contributing waves are all equal $U_A = U_B = U_C = 1$ and the wave vector coordinates satisfy three conditions $k_{ax} = 0$, $k_{by} = k_{cy}$ and $k_{bx} = -k_{by}$. It can also be assumed that the phase of wave *A* at the given vortex point is equal to zero. Using wave amplitudes, it is easy to find the phase angles of two other waves *B*, *C*; they are $2/3\pi$ and $4/3\pi$ (or vice versa if one wants to consider vortex point of opposite topological charge). The local phase portrait in the case of plane waves is the same for all vortex points of the same sign. The vortex point of opposite vortex sign differs in the orientation of phase lines. Thus, it is enough to consider one vortex point. It is reasonable to assume that this representative vortex point is located at the coordinate system origin. Then, from relations (3.26c) we have

$$\sin(T_{\psi a}) = 0, \quad \sin(T_{\psi b}) = -\frac{\sqrt{3}}{2}, \quad \sin(T_{\psi c}) = \frac{\sqrt{3}}{2}, \tag{3.37a}$$

$$\cos(T_{\psi a}) = 1, \quad \cos(T_{\psi b}) = -\frac{1}{2}, \quad \cos(T_{\psi c}) = -\frac{1}{2}\,. \tag{3.37b}$$

Now, the solution of the set of equations (3.36) is

$$k_{ay} = k_{by} + \sqrt{3}\,k_{bx}\,. \tag{3.38}$$

The solution is still non-unique. Figures 3.20a and 3.20b show two examples of local phase distribution generated by waves with parameters which satisfy equation

(3.38) with all related conditions. The plotted phase lines are symmetrically distributed. Figures 3.20c and 3.20d show the same examples with slightly different parameters. As expected, the plotted phase lines have asymmetrical distribution.

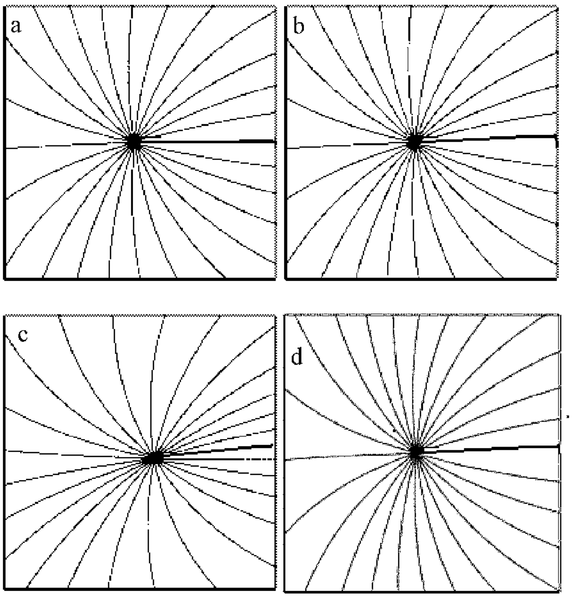

Fig. 3.20. Local phase distribution in the neighborhood of vortex point generated by three plane waves interference. Image size is 0.1 mm and light wavelength is 632.8 nm. a) All waves have unit amplitude. Wave vector coordinates are (in 1/mm) $k_{xa} = 0$; $k_{ya} = 0.675$; $k_{xb} = 4.206$; $k_{yb} = -6.61$; $k_{xc} = -k_{xb}$; $k_{yc} = k_{yb}$ and satisfy equation (3.38); b) Wave amplitudes are the same. Wave vector coordinates are $k_{xa} = 0$; $k_{ya} = 0.810$; $k_{xb} = 4.627$; $k_{yb} = -6.610$; $k_{xc} = -k_{xb}$; $k_{yc} = k_{yb}$ and satisfy equation (3.38); c) The same case as (a) but wave amplitudes are $U_A = 1.2$, $U_B = 1$, $U_C = 0.8$. This case does not satisfy conditions under which equation (3.38) is valid and the phase line distribution is not symmetric; d) The same case as (a) but wave vector $k_{ya} = -0.675$ does not solve equation (3.38) and phase distribution is asymmetric. Remark: All figures were plotted with the same equal phase separation values between subsequent equiphase lines

In the next chapter, the use of a regular OVs net generated by three plane waves interference as an interferometric reference system is discussed. Such interferometer is simple in construction and application, and has unique properties.

4. Optical vortex interferometer

4.1. Introduction

The phase singularities, including optical vortices, can be present in interference field generated by interferometers. Such objects were treated as a source of additional difficulties in phase reconstruction problem (see, for example, Fried *et al.* (1992), Ghiglia *et al.* (1998)). There were few exceptions. Bryngdhal [Bryngdhal 1973, Bryngdhal *et al.* 1974] proposed the interferometer with reference beam carrying optical vortices. The specific task for this interferometer was measuring wavefronts of radial symmetry. This interferometer did not attract much attention. In the papers by Larkin [Larkin *et al.* 2001, Larkin 2001] the "vortex transform" for phase demodulation is defined. This transformation can be performed physically by specially designed synthetic holograms. The holograms proposed in these papers are well known holograms generating OVs (see section 3.2). The vortex transform can be used to support phase reconstruction from interferograms.

Masajada *et al.* (2001) have proposed the interferometer based upon a regular net of optical vortices. Previously, brief notes on such a possibility were published in paper by Masajada *et al.* (2000) and the first public presentation of the interferometer took place at Diffractive Optics Conference in Budapest in 2001 [Masajada 2001]. The interferometer was named Optical Vortex Interferometer (OVI). This section is devoted to the OVI. The basic OVI optical scheme is presented in subsection 4.2. Section 4.3 deals with important problem of localizing vortex points in an OVI interference field. The applications are studied in sections 4.4 and 4.5. This is the first such complete publication devoted to OVI.

4.2. Interferometer set up

The Optical Vortex Interferometer (OVI) can be set up in various configurations. A number of measuring procedures can also be applied. Since there is no way to consider all of these possibilities only one of them, namely the simple system based on

Mach–Zender configuration, is presented (Fig. 4.1). In this example all problems characteristic of OVI interferometry can be discussed.

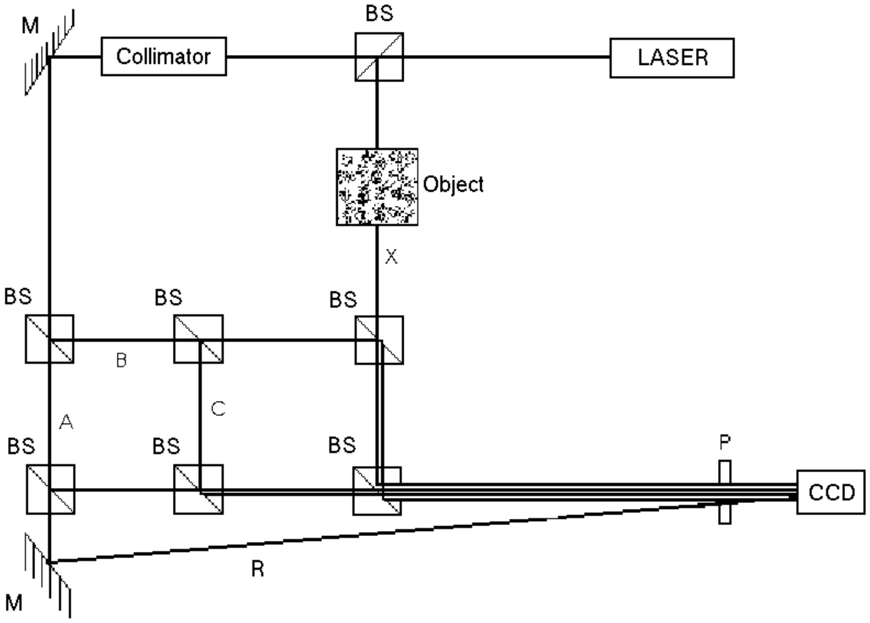

Fig. 4.1. Optical scheme of the OVI. This is the most extended version of the laboratory system. The extra reference beam *R* reflected from lower mirror M is optional and the simplest measurement schemes use only three beams marked as *A*, *B*, *C*, so the wave *X* can be removed. In the figure BS are the beam splitters, P is the polarizer (used optionally), CCD is the CCD camera

Figure 4.2 shows the system used in the author's laboratory. This laboratory setup can be easily modified. The OVI dedicated for specific applications can be designed in the more compact, movable and stable way.

The optical elements of the OVI are integrated onto a metal plate, 1100 mm in width and 1500 mm in length. The six beam splitters are fixed in a rectangular configuration. The mount of cubic beamsplitters provides high resolution angular and linear adjustment. There is some place between the beamsplitters for additional elements such as light stops, filters, phase shifters, etc. Mirror M allows visualization of OVs by interferometric method (see section 3.2.2) and is not necessary in the end user system. Optional polarizer P (cubic beamsplitter with polarizing coatings) supports linearly polarized output beams. The system is illuminated by stabilized He-Ne laser. The collimator with spatial filter gives the plane wave, the quality of which was tested by parallel $(\lambda/3)$ glass plate. Such an integrated optical system is positioned on anti-vibration table. To measure the interference pattern the CCD camera is used.

Fig. 4.2. View of the laboratory setup

The camera works with resolution of 758 × 560 pixels. It gives 8-bit black and white signal, which is binarized by Matrox frame grabber system. The grabbing software is supported by Dr Jarosław Jaroński and Dr Tomasz Licznerski from the Institute of Physics, Wrocław University of Technology. The software records images with frequency up to 10 frames per second. The software for image analysis was written by the author's research group and is still under development.

A sequence of interferograms have to be taken to measure the phase distribution of the beam investigated. In this sequence, some of the beams have to be passed and others stopped. The switching between beams *A*, *B*, *C* was made by moving a card from left to right between rows of beam splitters. With some practice the four measurements necessary in the simplest measurement scheme can be performed in less than two seconds. In the future the following improvements of the system will be considered:

- Electronic shutters which allow full system computerization.
- Fast, low noise, digital camera (10–12 bit) with one million pixels.
- New software for the analysis of interferograms.

With these improvements the system will be faster (at least five times), less sensitive to the noise and its resolution will be higher. Finally, the designated software strictly bounded with system hardware will support fast and full interferogram analysis.

Various measuring procedures can be used with this simple OVI system. Two of them are briefly described below.

4.2.1. Scheme I

In this scheme two plane waves (*B*, *C*) are used as reference beams. The wave *X* under investigation is the wave *A* (Fig. 4.1). Wave *X* has to be quasi-plane to preserve the regular form of the generated OVs net. The question of what the quasi-plane wave means depends on particular system characteristics.

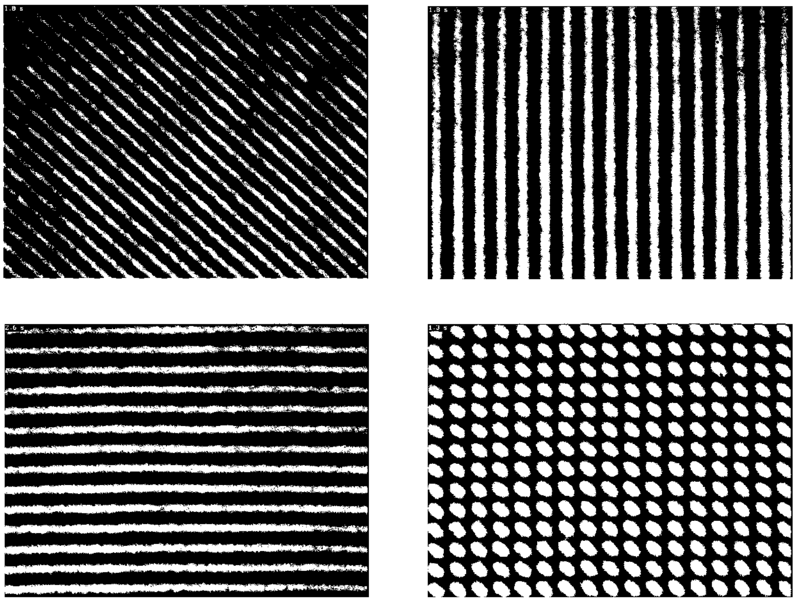

Fig. 4.3. The set of four interferograms needed in the case of the first measurement scheme (experimental results). The first three pictures show three two beam interferograms, the last figure (lower right corner) shows a three beam interferogram

To determine the relative phase of wave *X* the interferograms generated by pairs *X*+*B*, *X*+*C*, *B*+*C* and by all waves *X*+*B*+*C* must be taken. Figure 4.3 shows an example of such a series. At a vortex point (when the light intensity is zero) the following relations hold

$$I_X = I_{B+C}, \quad I_B = I_{X+C}, \quad I_C = I_{X+B} \tag{4.1}$$

where I_Q, I_{Q+R} $Q,R \in (X = A,B,C)$ are the intensities of single waves and pairs of interfering waves, respectively. Hence, at vortex points, the intensities of waves *X*, *B*, *C* can be determined by inspecting the values of the *X*+*B*, *X*+*C*, *B*+*C* interferograms. The square root of these intensities leads to the absolute values of the corresponding amplitudes (pseudo-amplitudes). Since, at vortex points, the corresponding amplitude vectors of waves *X*, *B*, *C* form a triangle the angles between them can be calculated. By determining triangle orientation – vortex sign – (Fig. 3.17) these angles can be directly related to the phase differences between waves *X*, *B*, *C*. In this way, the relative phase of wave *X* can be determined. To apply this first measurement scheme as well as the second one described below, the vortex points must be precisely localized. The localization problem is a subject matter of section 4.3.

4.2.2. Scheme II

In the second scheme three waves *A*, *B*, *C* are used as reference beams. The object under investigation is illuminated by the fourth wave *X*. Using scheme I the phase shifts between the reference waves can be found. Then the phase shifting procedure can be used [Creath 1998] for finding the relative phase angles between object and reference waves. For intensities measured in *A*+*X*, *B*+*X*, *C*+*X* interferograms, the following set of equations can be written

$$I_A + I_X + 2\sqrt{I_A I_X}\cos(\alpha_a) = I_{AX}\ , \tag{4.2a}$$

$$I_B + I_X + 2\sqrt{I_B I_X}\cos(\alpha_a + \delta_B) = I_{BX}\ , \tag{4.2b}$$

$$I_C + I_X + 2\sqrt{I_A I_C}\cos(\alpha_a + \delta_C) = I_{CX}\ , \tag{4.2c}$$

where δ_B, δ_C are phase shifts of waves *B* and *C* with respect to wave *A* calculated from the first three measurements (*A*+*B*, *A*+*C*, and *B*+*C*); α_a is the phase difference between waves *A* and *X*. The system of equations (4.2) is over-determined since there are three equations in two unknowns (i.e. I_X, and α_a). Therefore, one equation can support error corrections, as used in phase shifting interferometry, or can be used to improve the localization of vortex points. The second scheme demands more measurement steps but wave *X* may have an arbitrary wavefront.

Measurement schemes I and II can be modified in many ways. For example, in scheme II the new measurements of waves *A*+*B*+*X*, *A*+*C*+*X*, *B*+*C*+*X* which are equivalent to the measurements –*C*+*X*, –*B*+*X*, –*A*+*X* (where –*Q* means wave *Q* shifted by π) can be performed. More measurements require a more stable system but allow additional error compensation. Instead of adding new measurements the measurements *A*+*B*, *A*+*C*, *B*+*C* can be replaced by *A*+*B*+*X*, *A*+*C*+*X*, *B*+*C*+*X*, which demand a more complicated OVs localization procedure.

So far the second scheme has not been tested in great detail. However, much attention was put into studying the first one, which constitutes a part of the second scheme. Below the second scheme will not be considered any more.

It is worth noting that three plane waves which generate the reference OVs net are the optimum choice (at least in most of the practical applications of the interferometer). In the two beam system described in paper by Angelsky *et al.* (1997) the amplitude of reference wave must be carefully modulated and both detection process and the OVs localization procedures are more complicated and less accurate. More than three wave systems are also possible. If four reference waves are then used at vortex points the CAVs form a quadri-

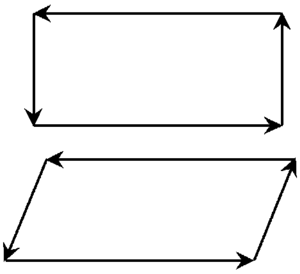

Fig. 4.4. At vortex points created by four waves interference relative wave phases cannot be determined in a unique way

lateral. Such geometry does not allow unique phase determination (Fig. 4.4). When more than four reference waves are used the localization of vortex points is even more ambiguous. In this work geometries with more than three waves are not studied.

4.2.3. Numerical simulations

Although the final evaluation of the OVI should be made in experiment, the numerical simulations are also valuable. In fact, it was the only way to get answer to questions when the necessary equipment was not available to the author. Specifically the limits of OVI resolution have not been tested experimentally yet. The results of the numerical simulations were in sound agreement with the real experiment in every case, when the experiment was possible.

The numerical simulations were performed in three steps. In the first step, the OVI interference field was modeled by ideal plane waves. Furthermore the plane waves were disturbed by extra plane waves of smaller amplitude (which simulate the reflections in the system) and some of them were modified by spherical waves with a great radius of curvature. The biggest amplitude of disturbing waves were ten times smaller than amplitudes of ideal plane waves. Finally, the plane waves were additionally disturbed by small phase and amplitude random factors. The numerical experiments were performed in two ways. In the first way, the full arithmetic precision of PC computers was taken advantage of. The densities of sampling points were much higher than in CCD camera used in experiment. In the second way the values representing measured values were binarized with 8-bit resolution characteristic of the camera used in experiment. The density of the simulated measurement points was also similar to the density of pixels at the CCD element.

4.3. Localization of vortex points

The OVs distribution in the field generated by three plane waves interference is very sensitive to disturbances introduced to one or more of interfering waves. Such disturbances can result from passing or reflecting of one or more interfering waves from the object under investigation. Tracing the changes in OVs positions the physical quantities related to the object investigated can be determined. For this reason the precision of OVs localization is of primary importance for the accuracy of measurements performed with OVI. Because the problem of localization of vortex points did not exist in classical interferometry, it will be discussed carefully in this section.

In this monograph the procedures applicable to the system shown in Figure 4.1 are presented. However, in author's opinion the methods discussed are general enough to be applicable in most of OVI systems, because they are based on common features of the OVI. The knowledge of specific conditions, characteristic of specific OVI system may result in additional methods, but cannot disprove these general ones.

4.3.1. Minima method

Since vortex points are points of zero light intensity they can be localized by finding isolated points where the light intensity is zero. The regularity of the OVs net can support such a procedure. In practice, due to noise, the measured intensities, at vortex points, are greater than zero. The highest influence of the detector noise is at the points where light intensity is low. So, instead of identifying zero light intensity points, the local light intensity minima are found. Although the OVs net generated in real experiment is never of perfect symmetry, its regularity is sufficient to support the local minima identification and give information on the total number of vortex points in the OVs net. This method for localization of vortex points is named minima method. The minima method may produce non-unique results. The effects of noise, quantization and binarization may cause that the area of local intensity minima are spread over few pixels. To extract a single point the center of gravity of such area is calculated.

To find the intensity minima certain threshold level has to be fixed. The simplest procedure rejects points at which light intensity exceeds the threshold level. If the threshold value is fixed too high a large number of false vortex points are identified. If the threshold value is too low some of the vortex points can be omitted. At this moment the advantages of OVs net regularity are clearly seen. Due to this regularity (although not perfect in real case) the number of vortex points and their approximate position is known (with accuracy of few pixels). To improve the minima method resolution the $A+B+C$ interferogram may be preprocessed by advanced image processing routines [Russ 1995]. The author and his coworkers have used the following image processing routines: local background analysis and subtraction, interferograms and their histograms scaling, numerical filtering, interpolation with bilinear method.

In the case of high quality optical and electronics system the minima method works with accuracy better than one pixel on average (i.e. most of the vortex points should be found at their theoretical localization, less than half should be shifted by one pixel, very few by two pixels).

The resolution of minima method is sufficient for a number of applications. When better accuracy is required or the OVI interference field is of poor quality more advanced localization methods are necessary. Such methods are described below. They require approximate vortex points position, which can be found by minima method.

4.3.2. Zero-crossing method

The zero-crossing method is based on the fact described in paper by Freund *et al.* (1994). At singular points the lines of $\mathrm{Re}(U) = 0$ and $\mathrm{Im}(U) = 0$ intersect (Fig. 2.2). The method uses the explicit form of the complex amplitude function describing the interfering waves and as such can only be used in computer simulations. As computer based method it can be calculated with full PC arithmetic precision and with high density of sampling points. The zero-crossing method is very precise and is treated as reference method in this chapter (in the case of numerical simulations).

4.3.3. Triangle method

Looking at OVs net phase plot one can see two characteristic features. In the vortex points neighborhood the equiphase lines have a star like geometry and this geometry is a dominant factor in the whole phase pattern (Fig 4.5). In such a case the neighborhood points should possess some information about the nearest vortex point. The concept of advance localization methods is based on this fact. Now the method named *triangle* will be analyzed.

At vortex point the corresponding CAVs form a triangle. The question is what the behavior of the CAVs in neighboring points is (Fig. 4.6a). To answer this question a remarkable number of different CAV configurations were studied. The representative cases were collected into atlas [Jarosławski 2003]. In this way some hypotheses were found and tested. Finally the most effective hypotheses were accepted and named “triangle method”. There is no space here to present all these considerations, so only the final results will be given and evaluated.

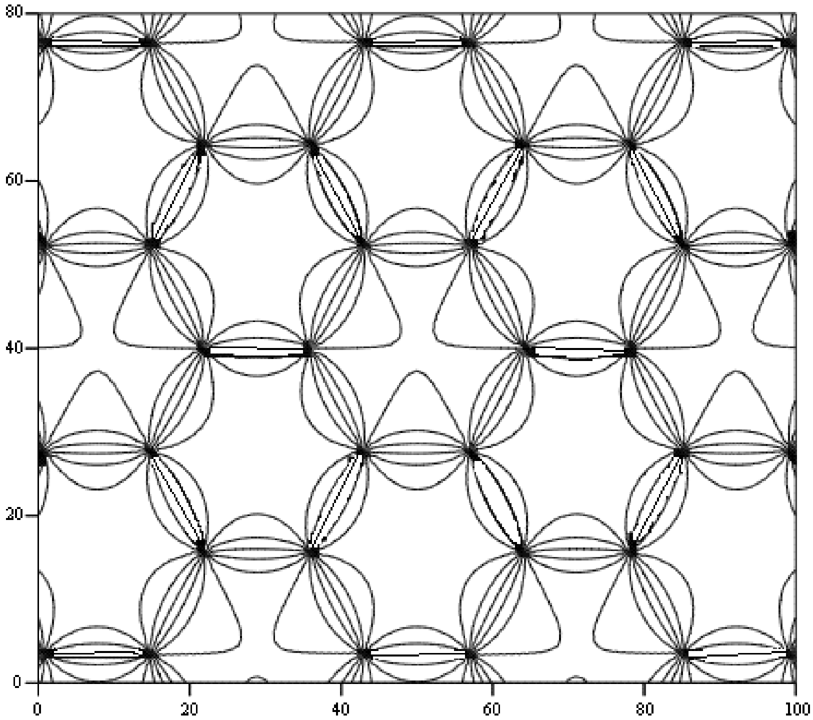

Fig. 4.5. Phase lines for highly regular OVs net – an example.
The vortex points are at places where phase lines converge. Around vortex points each phase line represents different phase value. The phase is changing continuously from zero to 2π

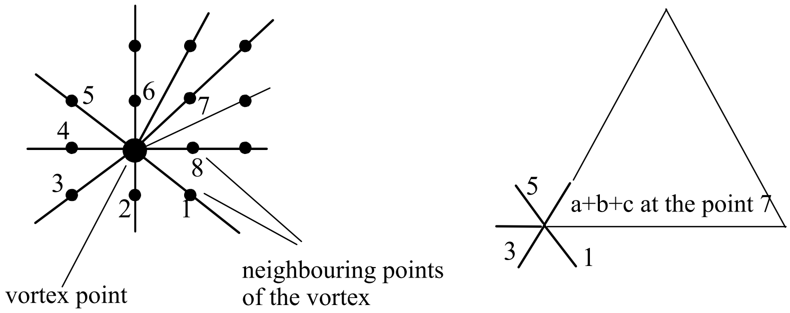

Fig. 4.6. a) Schematic view of the pixel distribution at CCD element.
At rectangular net each vortex point has eight neighbor points; b) Schematic view of the CAVs of A+B+C field around the vortex point. Around the vortex point the CAVs change their orientation by 2π. In a real case the phase angle does not change uniformly while going around the vortex point

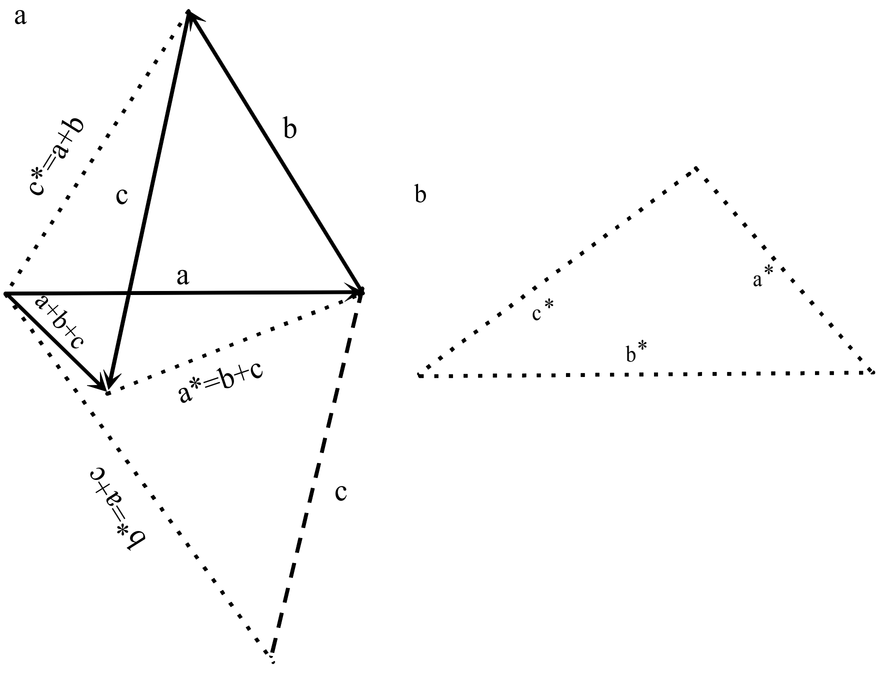

Fig. 4.7. In the neighborhood of the vortex point the CAVs
do not form a triangle; however, the triangle can be formed from a^*, b^*, c^* sides

Figure 4.6b shows schematically the CAVs geometry at the point close to the vortex point. Although the CAVs do not form a triangle the triangle can be formed with a given set of three CAVs. Such triangles will be called "false triangles". The measured quantities are I_{ab}, I_{ac}, I_{bc} and their square roots can be considered as lengths of the false triangle sides (Fig. 4.7). To follow the triangle method the tentative vortex points are necessary. The tentative vortex points indicate the area of true vortex points localization. They can be found by minima method. Having the tentative vortex points one must investigate their neighbourhood. It is enough to consider all points at a distance of no more than four pixels from each tentative vortex point. For this purpose, a set of submatrices representing measured light intensity at CCD pixels in the neighborhood of tentative vortex points is created. At each point belonging to such submatrices the false triangle is created. Each false triangle is normalized in such a way that length of its longest side is equal to one. Now, the following expressions are calculated $|a^* - b^*|$, $|a^* - c^*|$, $|b^* - c^*|$ and the greatest among them is picked up. This value will be denoted by BV. The true vortex point has the greatest number of neighbors with BV, that are greater than the BV of the given true vortex point. To complete the method the following procedure was written (Fig. 4.8). For each point belonging to a given a submatrix (except the border points) the closest points were compared with respect to the BV value. If the BV value was greater the corresponding cell was filled with zeros, if not the cell was filled with ones. Then the numbers in surrounding cells were added and the result was written to the central cell. By repeating this procedure a new submatrix was created. The minimal value in this new submatrix indicates the position of true vortex point. The important feature of the triangle method is that when the tentative vortex point is a false vortex point the method still shows the position of the true vortex point. In Figure 4.8c the tentative vortex point was a true vortex point. Figure 4.8d shows the same example, but with shifted tentative vortex point. The minima also shift to the true vortex point.

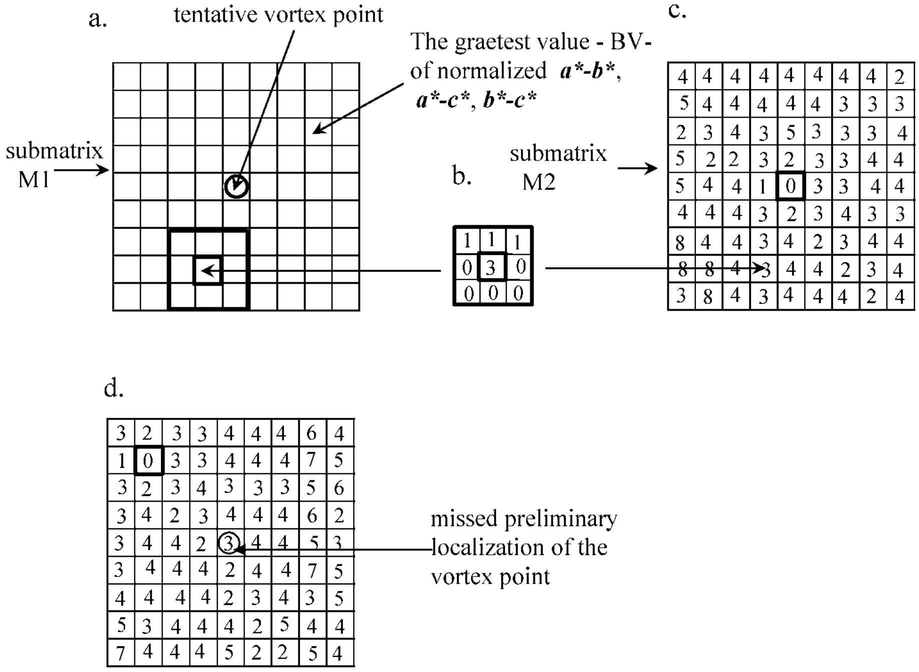

Fig. 4.8. Figures illustrate the algorithm for triangle method. In Figure the submatrix representing the pixels around the tentative vortex point is shown; b) at each cell of this submatrix the number of BV is written; Figure c shows the resulting submatrix in the case of tentative vortex point being in the same place as true vortex point (in the matrix center); Figure d shows the case when the tentative vortex point misses the true vortex point by three pixels. The minimal value still shows true localization of vortex point. This matrix was calculated for experimental data

The triangle method can also be applied in a slightly different manner. Instead of analyzing the BV value one can study the relations between the longest triangle sides. The rest of the procedure is the same. The accuracy of this version is practically the same, but the results between these two versions are slightly different (at the subpixel level).

There has been no sufficient error analysis of this method provided yet. The method is sensitive to the amplitude variations across the contributing plane waves. However, if these variations are not rapid the method works well. The best results are obtained when the component plane waves have the same amplitude. In this case the method is also easy to prove. When the amplitudes become different the localization accuracy slightly decreases. The errors can rise when one of the waves has remarkably lower amplitude, but then the vortex points become close to each other and all localization procedures fail. For this reason the case when one wave has much smaller amplitude than two others should be avoided. The numerical and experimental tests of the triangle method are presented in section 4.3.5.

4.3.4. Amplitude method

The concept of the method named amplitude method is based on the fact that in the vortex point neighborhood the phase circulates at 2π. This should affect the intensity distribution of $A+B$, $A+C$, $B+C$, $A+B+C$ interferograms in the vortex point neighborhood. Using this hypothesis the method named pseudo-phase method was invented [Popiołek-Masajada *et al.* 2003]. Then the method was improved and named amplitude method [Masajada *et al.* 2004]. Compared to pseudo-phase method, the amplitude method is simpler, faster, and more accurate. The efficiency of amplitude method was not proved in any rigorous way (mathematically), but it was intensively tested. The numerical and experimental tests have shown that the amplitude method works effectively. Their limits are similar to the triangle method. The best results are obtained when the amplitudes of interfering waves have comparable magnitude. Below, a brief description of the amplitude method is given.

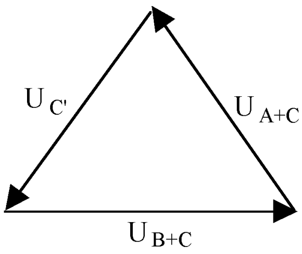

Fig. 4.9. The triangle used in amplitude method

The interferograms should be prepared by preprocessing procedures and the tentative vortex point must be found. Then small submatrices (7 × 7) covering such areas, with tentative vortex points in the center must be chosen. From $A+B$, $A+C$, $B+C$ interferograms the cosines of their relative phase angles are determined. This is a common problem solved in two beam interferometry. In the next step, at each analyzed point a triangle is built as is shown in Figure 4.9. Having the triangle sides *BC* and *AC* and the angle between waves *A* and *B* (read from *A*+*B* interferogram) the cosine rule is used to calculate value of C' (Fig. 4.9) and the difference $|C'-AB|$ is calculated. Following the same way the expressions $|B'-AC|$ and $|A'-BC|$ are calculated at each measurement point under investigation. Then the following sum is calculated $\frac{|A'-BC|}{BC}+\frac{|B'-AC|}{AC}+\frac{|C'-AB|}{AB}$ and this value is written down into matrix cell corresponding to the measurement point being analyzed. In such a way a new matrix is defined and its minimum shows the vortex point position. In the last step the local coordinates are recomputed to global coordinates covering the whole measurement area. Tests of the amplitude method are presented in the next section.

4.3.5. Results and discussion

The localization methods were tested both numerically and experimentally. First, the numerical tests will be presented. To be close to experimental conditions the numerically defined plane waves were disturbed by other waves, both plane and spherical of smaller amplitude. Representative examples of tests are discussed below.

In the numerical simulations the analyzed area corresponds in the size and pixel density to the 8-bit CCD camera used in the experiment (1/3 inch of diameter with 768/576 pixels). In this area 216 OVs were generated. The reference position of vortex points was determined by zero crossing method calculated with full precision of PC arithmetic and with higher density of sampling points (four times more than in experiment). To simulate the experimental conditions the interferograms were binarized with 8-bit resolution. In the next steps the interferograms were processed in the same way as experimental interferograms. Their quality was improved by image processing routines. Finally the tentative vortex points were localized with minima method followed by the triangle and amplitude methods. Figure 4.10 shows the difference between results obtained by new methods and reference method, i.e. zero-crossing method. Figure 4.10a represents the triangle method and Figure 4.10b the amplitude method. The results are shown in three cases: in the case when no interpolation was made and in the case of interpolation which increases the measurement point density by factor two and four (level 2 and level 4, respectively). Both methods give comparable results when compared with the reference method. For most of the vortex points the difference in position is less than the distance between neighboring pixels. Very few of them are localized with accuracy higher than the distance between neighboring pixels. The interpolation improves the results. The efficiency of interpolation procedures shows that the relative density of measurement points is an important factor, for vortex points localization accuracy. Relative density means here the number of CCD pixels per one vortex point. The high accuracy of localizing vortex points yields high accuracy of OVI measurements. Thus the OVI accuracy can be improved by applying low noise CCD camera with great number of pixels and preserving the total number of vortex points over the whole CCD element.

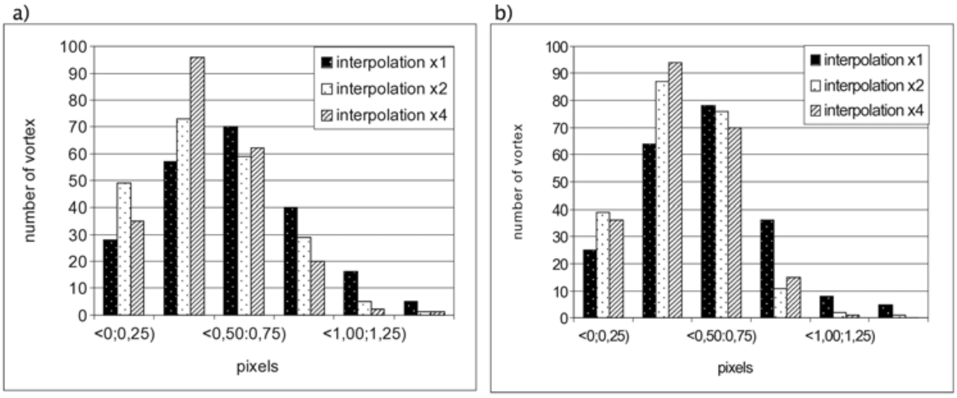

Fig. 4.10. Localization of vortex points – numerical simulations.
a) amplitude method; b) triangle method

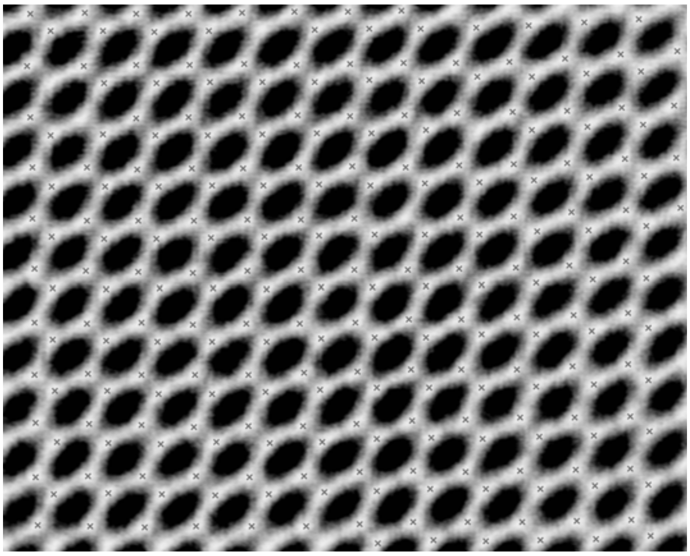

Fig. 4.11. The crosses show the position of vortex points localized in the interference field of the OVI (experiment). The vortex points were localized by triangle and amplitude method. When the results were different by more than the distance between CCD pixels then the position of vortex point was not plotted. The figure is printed in reverse contrast

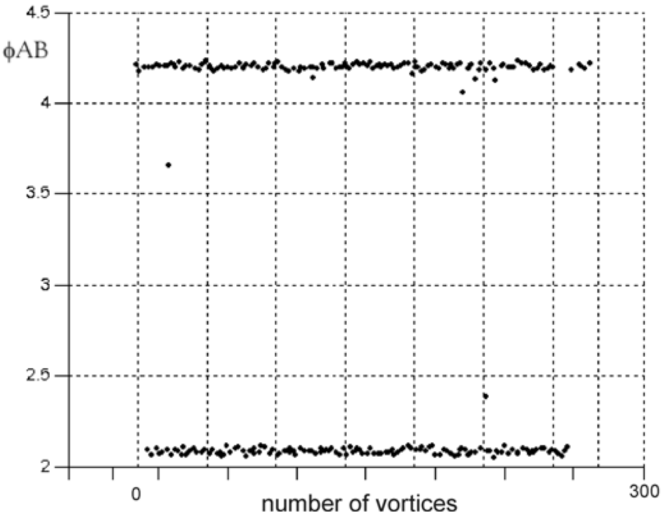

Fig. 4.12. The phase angle between two of the three interfering waves (experiment).
The two clouds of points correspond to two topological charges of OV.
The variations of the phase value, within each cloud are small – less than 0.15 radian.
A few bad points, which lie out of the clouds, can be easily excluded

Figure 4.11 shows results obtained from the experimental data. At CCD element 259 vortices were born. This figure shows vortex points, which were localized by both methods (amplitude and triangle), with difference not greater than the distance between neighboring CCD pixels. Only few vortex points have not passed this test, meaning that on experimental interferograms both methods give close results.

When vortex points are localized the relative angles between interfering waves can be calculated (3.16). Figure 4.12 shows the phase difference between two of the three interfering waves calculated for vortex points localized by triangle method. In the experiment three plane waves of a 3 cm diameter were used. The beams were adjusted in such a way that they overlap at CCD element (of 1/3 inch diameter) with their most regular parts. The beams enter the CCD element directly, i.e. without using objectives. In this way a high quality OVs net was obtained. The calculated phase angle between these two waves is almost the same for each measurement point, as should be expected in this case. Except for a few bad points, the difference in phase values is less than 0.15 radian. These points can easily be identified and eliminated from further investigation. The interferogram area which contains such points has irregularities, so by inspection they can be removed. The position of bad points, which was determined by triangle and amplitude method differs more than the distance between neighboring pixels, so in Figure 4.11 the bad points have already been excluded.

It should be noted that the differences in phase angle value estimated above cannot be treated as an error introduced by the measurement system. The interfering waves *A*, *B*, *C* were not perfect, so the relative phase angle between interfering waves varies across the measurement area. The calculated variations of the phase value for different vortex points fit very well to the expected values. These results show that the OVI works correctly, but the limits on its possible resolution must be determined in another way.

As was already mentioned the OVI accuracy strongly depends on the precision of localizing vortex points. In this work, some general information on OVI resolution is given.

The most important factor for accuracy of vortex points localization is the number of the CCD camera pixels per one vortex point (density of CCD pixels). For 8-bit detector the maximum useful density is about 3000 pixels per one vortex point. Since the gradient of slow varying fringe intensity cannot be registered with sufficient resolution, the higher density of CCD pixels does not results in better localization accuracy. Thus, the higher density of CCD pixels requires higher level of data binarization (10, 12, 14 bit). On the other hand, when the number of measurement points is important the relative density of CCD pixels cannot exceed some limit. For each OVI system devoted to specific measurement problem the density of CCD pixels should be optimized according to the parameters of available detectors, electronics and the specific measurement conditions.

Table 4.1

The phase between two interfering waves determined for different localizations of the vortex point. The central cell (gray cell) represents the true vortex point and reference value of the phase. The other cells represent the neighboring pixels at CCD element. The density of CCD pixels is 2100 pixels per vortex point. The phase values are given in radians

1.7993	1.8592	1.9192	1.9790	2.0391
1.9031	1.9631	2.0230	2.0830	2.1429
2.0070	2.0669	2.1269	2.1868	2.2467
2.1108	2.1707	2.2307	2.2906	2.3506
2.2146	2.2746	2.3345	2.3945	2.4544

Table 4.2

The phase between two interfering waves determined for different localizations of the vortex point. The central cell (gray cell) represents the true vortex point and reference value of the phase. The other cells represent the neighboring pixels at CCD element. The density of CCD pixels is 8200 pixels per vortex point. The phase values are given in radians

1.2973	1.4172	1.5371	1.6570	1.7769
1.5050	1.6249	1.7448	1.8647	1.9846
1.7127	1.8326	1.9524	2.0723	2.1922
1.9203	2.0402	2.1601	2.2800	2.3999
2.1280	2.2479	2.3678	2.4877	2.6075

Tables 4.1 and 4.2 show the influence of localization error on the phase difference between two waves determined using OVI. The results were obtained by numerical modeling. The two cases shown in the table represent two different densities of CCD pixels. In the first case this density has value 2100 pixels per vortex point while in the second case 8200 pixels per vortex point. In both cases the gray cell shows the phase value for the point of true localization of the vortex point. The neighboring cells show this value for vortex points localized in the neighboring CCD pixels. The tables show that the error in phase value depends on both the value and direction of localization error. This second factor can be understood when considering the dynamics of CAVs around the vortex point. There is always a direction where CAVs of waves *A*, *B*, *C* rotate almost in the same way and their sum is close to zero. In this direction the error in phase determination increases slowly. There is also a direction along which the rotations of CAVs give fast increase in the total light intensity in the *A*+*B*+*C* interferogram, which results in fast increasing of the error of phase angle value.

The simulations were also performed for high quality OVI system working with 12 bit low noise CCD camera. Applying the localization routines described in this monograph, the optical vortices can be localized with accuracy better than 0.5 of distance between neighboring pixels of CCD camera. This results in the relative phase angle determined with accuracy better than 0.02 radian. Of course, in real measurements the mechanical and thermal effects will cause additional errors lowering the OVI resolution. The discussion on the influence of these factors on OVI resolution is out of the scope of this monograph.

4.4. OVI features

The set of three independent plane waves defines a unique plane which will be called the “OVI-plane” (Fig. 4.13). The orientation of this plane does not depend on the interfering waves amplitude and phase, but only on their wave vectors. It is easy to prove that vortex points propagate perpendicularly to the OVI-plane. Wave vectors, together with a corresponding OVI-plane, form a tetrahedron (Fig. 4.16a). In a real situation, when the waves are not perfectly plane, their wave vectors determine “OVI-surface”, but this case will not be considered here. Let the *z*-axis of the coordinates system be oriented along such tetrahedron height, which is perpendicular to the OVI-plane. Then the wave vectors $\mathbf{k_a},\mathbf{k_b},\mathbf{k_c}$ have the same *z*-coordinate. Thus, when moving along a line parallel to the tetrahedron height, the CAVs of three interfering waves rotate through the same angle. If at the given point of such a line the CAVs form a triangle, it is the same at all other points of this line, meaning that this line is a trajectory of vortex point. This means that a stable and regular system of OVs lines, which is perpendicular to the observation plane can be generated by OVI. Such a system can be used in 3-D scanning interferometry, where the interferograms are taken at subsequent observation planes shifted along the *z*-axis (by shifting CCD element, for example). It is important that the phase relations between interfering waves do not change along vortex lines and the subsequent interferograms are mutually related. This possibility has not been studied yet in detail.

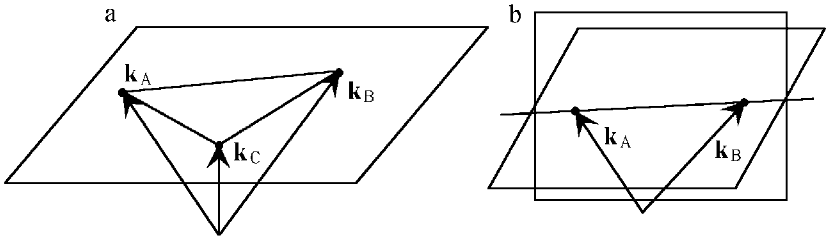

Fig. 4.13. a) Three non-collinear wave vectors define a plane which is called the OVI-plane. Wave vectors together with OVI plane form tetrahedron;
b) Two non-collinear wave vectors correspond to infinite number of possible planes

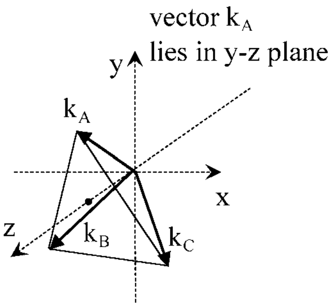

Fig. 4.14. Three wave vectors which form with OVI-plane a regular tetrahedron

The influence of the three main wave parameters can be evaluated separately when using OVI. These parameters are: *A*, *B*, *C* wave vectors, phases and amplitudes. Wave vectors are responsible for the distribution of positive (negative) vortex points. Wave amplitudes define the relative phases between the interfering waves at vortex points and the geometrical relations between two subnets of positive and negative vortex points. The changes in the phase of interfering waves shift a net of vortex points as a rigid body. Such a decomposition is important when considering OVI applications. For example, it allows a smart small-angle rotations measurement which will be discussed in the next section.

Now, an example of a symmetrical vortex points net will be defined. It will be used in further considerations as an illustrative example. When solving equations (3.19) under the conditions $\Delta x = 0,\ \Delta y = 0$, one gets the wave vectors based on the equilateral triangle (Fig. 4.14). Assuming the *z*-axis of the coordinate system lies along the corresponding tetrahedron height and $\mathbf{k}_{\mathbf{a}}(0,\ k_{ay},\ k_{az})$ the following relations can be written

$$\left|\frac{k_{bx}}{k_{by}}\right| = \sqrt{3}\,, \quad 2k_{by} = -k_{ay}\,, \quad k_{by} = k_{cy}\,, \quad k_{bx} = -k_{cx}\,. \tag{4.3}$$

In this symmetrical case, all two beam interferograms have fringes of equal density. The fringe orientation and phase distribution is also symmetrical (Fig. 4.15 and Fig. 4.16).

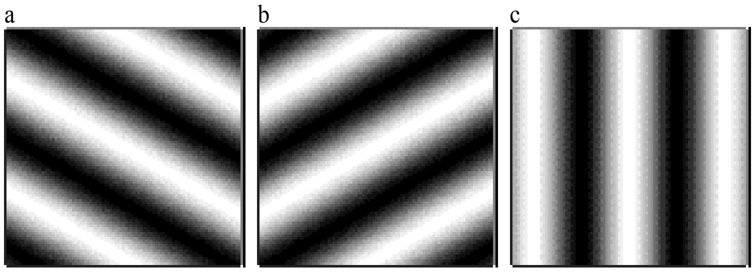

Fig. 4.15. In the case of waves geometry shown in Figure 4.14 the fringes of two beam interferograms are of equal density. This figure shows interferograms of waves *A+B*, *A+C*, *B+C*, respectively

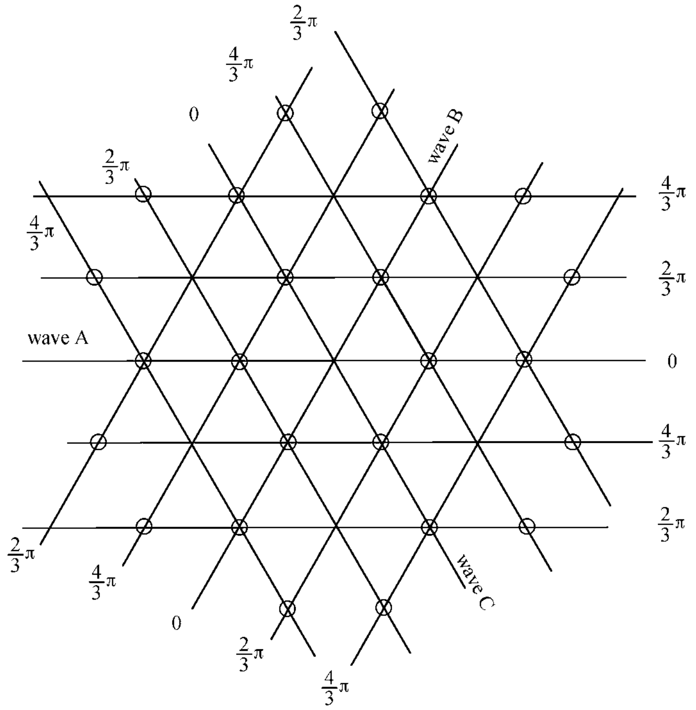

Fig. 4.16. Plot of vortex points (circles) distribution and corresponding equiphase lines of interfering plane waves *A*, *B*, *C* in the case of the wave geometry as shown in Figure 4.14. The reference plane is OVI-plane

In the arrangement of interfering waves shown in Figure 3.14, where wave phases were determined with respect to the wave *A* surface, waves *B* and *C* have two different phase values at vortex points. Presently, when wave phases are determined in respect of OVI-plane, waves *A*, *B*, *C* have three phase values at vortex points. This is true in a symmetrical case corresponding to the tetrahedron geometry shown in Figure 4.14. Generally, interfering waves *A*, *B*, *C* may have an infinite number of different phase values at vortex points. These three possible phase values of waves *A*, *B*, *C*, at vortex points, can be determined in the following way.

The net of OVs shown in Figure 4.5 can be transformed using transformation (3.15) to the corresponding net with one contributing wave (say *A*) parallel to the observation plane. Furthermore, the transformed values are denoted by a prime. Let the phase of wave A' be equal zero in the observation plane (which is a purely technical assumption). Having the amplitudes *a*, *b*, *c* of contributing waves the phases of waves B', C' with respect to wave A' can be found at vortex points (Fig. 3.17). Two possible values for each wave are obtained in this way (say $\Psi 1_b, \Psi 2_b, \Psi 1_c, \Psi 2_c$). At the center of the coordinates, let there be a vortex point for which these values are $(\Psi 1_b, \Psi 1_c)$. These assumptions are also purely technical and have no influence on the result. To answer the question regarding the location of the next vortex point of the same phase geometry (topological charge) the set of equations is solved

$$\left.\begin{aligned} x_v\, k'_{bx} + y_v\, k'_{by} &= 2\pi\, m \\ x_v\, k'_{cx} + y_v\, k'_{cy} &= 2\pi\, n \end{aligned}\right\} \tag{4.4}$$

The solutions is

$$x_v = 2\pi \frac{m\, k'_{cy} - n\, k'_{by}}{(k'_{bx}\, k'_{cy} - k'_{by}\, k'_{cx})}\,, \tag{4.5a}$$

$$y_v = 2\pi \frac{n\, k'_{bx} - m\, k'_{cx}}{(k'_{bx}\, k'_{cy} - k'_{by}\, k'_{cx})}\,. \tag{4.5b}$$

To calculate the corresponding phases Ψ_q of original waves (before transformation (3.15)) the following equation can be used

$$x_v\, k_{ax} + y_v\, k_{ay} = \Psi_a\,. \tag{4.6}$$

It is enough to solve this equation for wave *A* (the simplest case) and find the corresponding solution for waves *B* and *C* directly from the triangle geometry (Fig. 3.17). In the given example $k_{ax} = 0$, and equation (4.6) has a particularly simple form

$$y_v\, k_{ay} = \Psi_a\,. \tag{4.7}$$

The formula for Ψ_a is

$$\Psi_a = 2\pi k_{ay} \frac{(n+m) k'_{bx}}{k'_{bx} k'_{cy} - k'_{by} k'_{cx}}, \tag{4.8}$$

where relations (4.3) were used. Applying (3.16) we have

$$k'_{bx} k'_{cy} - k'_{by} k'_{cx} = 2 k_{bx} (k_{cy} - k_{ay}). \tag{4.9}$$

Using relations (4.3) one gets

$$\Psi_a = \pi \frac{(n+m)}{\left(\frac{k_{cy}}{k_{ay}} - 1 \right)}. \tag{4.10}$$

For such regular geometry of waves vectors $k_{cy} / k_{ay} = 1/2$ and finally

$$\Psi_a = -\pi \frac{2}{3} (n+m). \tag{4.11}$$

This formula gives three possible (modulo 2π) values of wave *A* phase at singular points. These values are 0, $2/3\pi$, $4/3\pi$. Referring to the triangle geometry, one can find that waves *B*, *C* may have the same three phase values for both topological charges of vortex points.

4.5. Small-angle rotations measurement

A new method for measuring small-angle rotations is discussed in this section. The method uses OVI and has a number of important advantages compared with other interferometric methods that have the same resolution. These advantages will be discussed briefly in the last part of this section.

The possible optical scheme of OVI dedicated to small-angle rotations measurement is shown in Figure 4.17. Mirror RM should be mounted on the element under rotation. The wave geometry is as shown in Figure 4.14. The symmetrical wave geometry produces a symmetrical phase distribution, which is very suitable for the presentation of the method. The question of whether this is the best wave geometry for performing this kind of measurements with OVI has not been answered yet. Preliminary studies have shown that other wave arrangements result in similar precision of measurements.

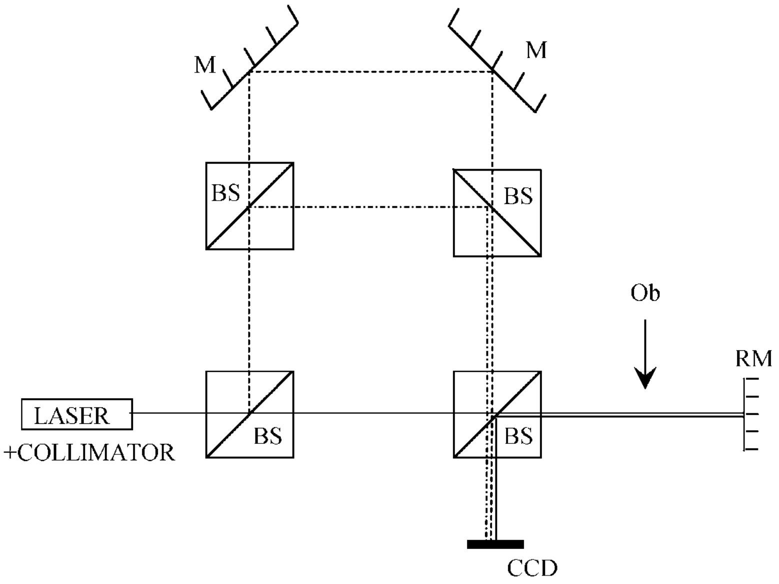

Fig. 4.17. Optical scheme of the OVI designed for measurement of small-angle rotations

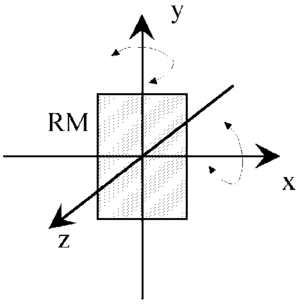

Fig. 4.18. Rotation axis orientation

In present case the reference plane is the OVI-plane, i.e. all phase values are determined in the OVI-plane. Figure 4.18 shows the orientation of the rotation axis – the mirror RM can be rotated about two perpendicular axes *x* and *y*. If mirror RM rotates at a small angle, the interference pattern ($A + B + C$) changes. Also, the configuration of the vortex point net changes. This shift of vortex points can be measured and its magnitude is strictly related to the angle through which mirror RM was rotated.

When the wave *A* changes its orientation vortex points move in a specific way. To understand this dynamic, the concept of constant angle lines of two waves must be introduced. Constant angle lines of two waves are two lines along which phases of these waves change at equal rates. This means that when moving along such a line, the relative phase angle between these waves is constant. Figure 4.19 shows how to determine such a line geometrically.

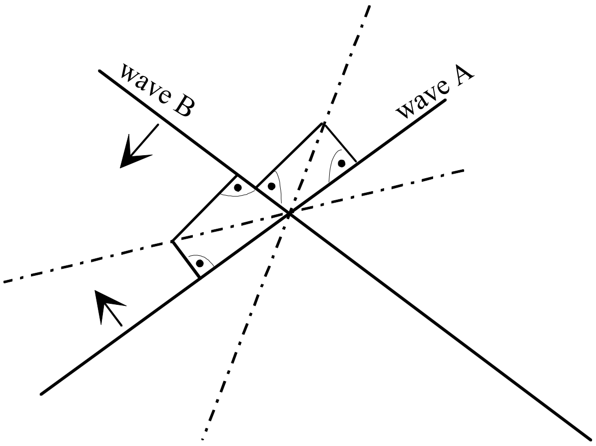

Fig. 4.19. Geometric way for finding constant angle lines of two interfering plane waves. Constant angle lines are the lines along which phases of two given waves *A*, *B* change at equal rate. Two segments are plotted perpendicularly to equiphase lines of waves *A* and *B* in such a way that their ends meet. The ratio of their length is equal to the ratio of the period of waves *A*, *B* measured in observation plane. Any two plane waves have two constant angle lines, which corresponds to two possible topological charges of optical vortices. Arrows show the direction in which *A*, *B* wave phases increase

Figures 4.20 and 4.21 show schematically the vortex points shifting under mirror RM rotation about the x and y axes, respectively. Figure 4.22 shows the vortex point shift when the mirror RM rotates about both axes. If the mirror RM rotates about the x-axis, then the distance between two equiphase lines of wave A decreases or increases, and their orientation remains the same.

If the mirror RM rotates about the y-axis, then the distance between two equiphase lines of wave *A*, measured along the y-axis, remains the same, but the lines rotate in the OVI-plane. When wave *A* is reflected from mirror RM the relative phases between waves *B* and *C* remain unchanged. Hence, under mirror RM rotation, the vortex points must move along constant angle lines of waves *B* and *C*. The angle of mirror RM rotation can be determined by measuring the shift of vortex points. Since this shift differs in character when the mirror RM rotates about x or y axis, the two different rotation angles can be determined simultaneously in a single measurement.

When mirror RM undergoes the linear shift, due to vibration, for example, then the vortex point net moves as a rigid body. This additional shift can be subtracted, and in fact it is subtracted automatically when using the procedures described below. Thus, the system presented is resistant to vibrations, which is one more of its important advantages.

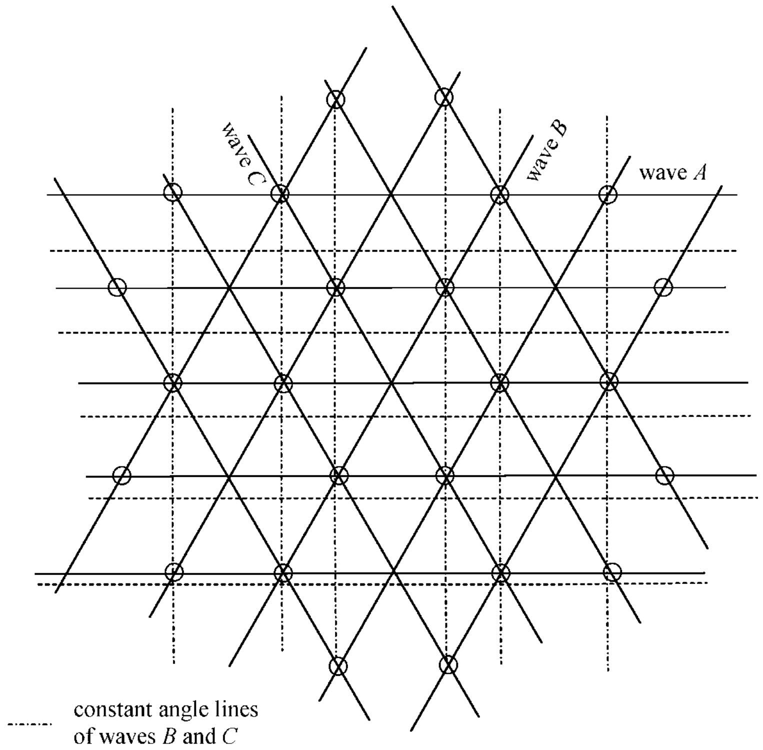

Fig. 4.20. Equiphase lines of three waves *A*, *B*, *C* forming OVI vortices net – an example.
The waves have equal amplitudes and their wave vectors are:
$\mathbf{k}_\mathbf{a}(0, k_{ay}, k_{az})$, $\mathbf{k}_\mathbf{b}(\sqrt{3}\,k_{az},\ k_{ay}/2,\ k_{az})$, $\mathbf{k}_\mathbf{c}(-\sqrt{3}\,k_{az},\ -k_{ay}/2,\ k_{az})$.
Vortex points are denoted by circles. Dash-dotted lines are constant angle lines of waves *B*, *C*.
Dashed lines show the equiphase lines of wave *A* after mirror rotation.
Rotation around *x*-axis causes that the density of the equiphase lines of wave *A* decreases or increases, but their orientation remains the same. Vortex points move along constant angle lines of waves *B* and *C*.

The rotation of mirror RM changes the coordinates of the wave vector $\mathbf{k}_\mathbf{a}$ by $(\Delta k_{xa},\ \Delta k_{ya})$, which are related to the rotation angles about the *y* and *x* axis, respectively. They can be determined by solving the following system of equations:

$$\Delta x1\,k'_{xb} + \Delta y1\,k'_{yb} = \Delta xn1\,(k'_{xb} - \Delta k_{xa}) + \Delta yn1\,(k'_{yb} - \Delta k_{ya})\,, \tag{4.12a}$$

$$\Delta x2\,k'_{xb} + \Delta y2\,k'_{yb} = \Delta xn2\,(k'_{xb} - \Delta k_{xa}) + \Delta yn2\,(k'_{yb} - \Delta k_{ya})\,, \tag{4.12b}$$

where relations (3.16) were used. These equations require the position of three vortex points (say, VP1, VP2, VP3, which will be named the vortex triplet). In the OVI system under consideration, many vortex points are generated. This result in thousands of vortex triplets and the advanced statistical method can be applied to increase the measurement resolution. The difference in the x and y coordinate between VP2 and VP1 vortex points before rotation is denoted by $(\Delta x1, \Delta y1)$, while $(\Delta x2, \Delta y2)$ is such a difference between VP3 and VP1 vortex points. The values $(\Delta xn1, \Delta yn1)$ and $(\Delta xn2, \Delta yn2)$ are such differences between the same pairs of points but shifted due to rotation.

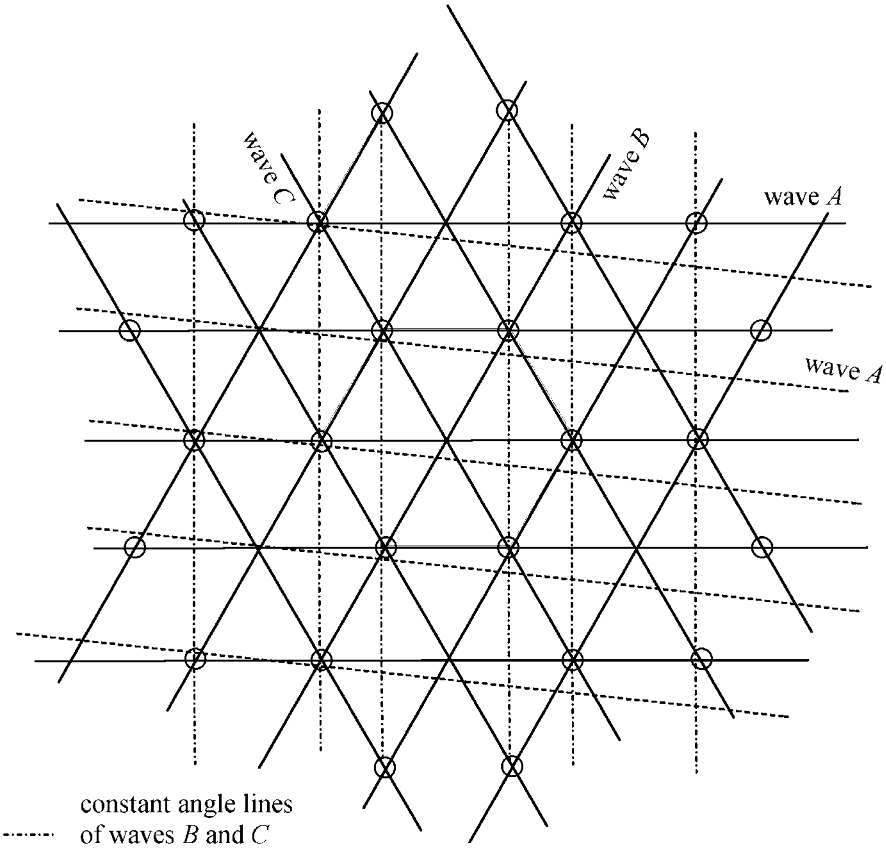

Fig. 4.21. The same case as in Figure 4.19 but the mirror RM rotates about the y-axis. In this case, the equiphase lines of wave A preserve their density along y-axis but change their orientation. For the same reason as above the vortex points move along constant angle lines of waves B and C

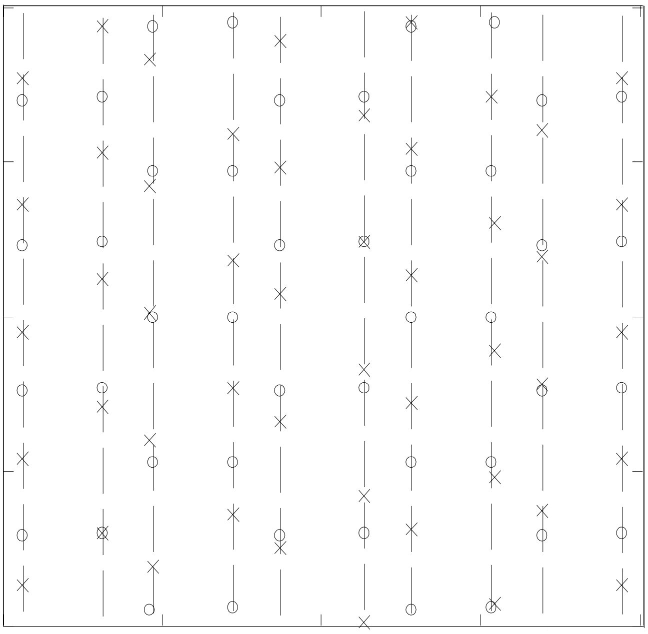

Fig. 4.22. Circles show the position of the vortex points before rotation, while crosses show their position after rotation. Dashed lines show the constant angle lines of reference waves. Rotation angles are: 2 arc second about x-axis and –4 arc second about y-axis. The plot has size 200×200 pixels with density corresponding to standard CCD camera resolution. Wave vector coordinates of interfering waves are:

$\mathbf{k_a}(0,-4.44,9.929\cdot 10^4)$, $\mathbf{k_b}(3.846,2.22,9.929\cdot 10^4)$, $\mathbf{k_c}(-3.846,2.22,9.929\cdot 10^4)$.

The plot was calculated by computer and all values were binarized with 8-bit resolution

This set of equations has the solution:

$$\Delta k_{xa} = \frac{(\Delta x2\,\Delta yn1 + \Delta xn1\,\Delta yn2 - \Delta x1\,\Delta yn2 - \Delta xn2\,\Delta yn1)\,k'_{xb}}{\Delta xn1\,\Delta yn2 - \Delta yn1\,\Delta xn2}$$

$$\frac{(\Delta y2\,\Delta y1 - \Delta y1\,\Delta yn2)\,k'_{yb}}{\Delta xn1\,\Delta yn2 - \Delta yn1\,\Delta xn2}, \tag{4.13a}$$

$$\Delta k_{ya} = \frac{(\Delta y1\,\Delta xn2 + \Delta xn1\,\Delta yn2 - \Delta y2\,\Delta xn1 - \Delta yn1\,\Delta xn2)\,k'_{yb}}{\Delta xn1\,\Delta yn2 - \Delta yn1\,\Delta xn2}$$

$$\frac{(\Delta x1\,\Delta xn2 - \Delta x2\,\Delta xn1)\,k'_{xb}}{\Delta xn1\,\Delta yn2 - \Delta yn1\,\Delta xn2}. \tag{4.13b}$$

In order to use solutions (4.13), the values of (k'_{xb}, k'_{yb}) must be known. If the interferograms (*A*+*B*, *A*+*C*, *B*+*C*) are taken, then quantities (k'_{xb}, k'_{yb}) can be determined by inspecting the corresponding fringe density along the *x* and *y* axes, respectively. This is a standard procedure in interferometry (finding the relative angles between two interfering waves) and will not be discussed here. One more procedure is described below.

Before calculations are made, it is advisable to change the coordinate system in such a way that one axis, say the *y*-axis, is parallel to constant angle line of waves *B* and *C*. Figure 4.23 shows a part of the vortex point net shown in Figure 4.21. For calculation purposes a vortex triplet must be chosen. In Figure 4.23, the points belonging to vortex triplet are denoted by P1, P2, P3. One of these points (point P1) will be treated as a reference point of the triplet. Now, the relative angles between the interfering waves can be calculated (Fig. 3.17). Because the relative angles are necessary, one can assume that the CAV of wave *A* at the reference point P1 has a phase angle equaling zero. Figure 4.23 shows how the angles of interfering waves change when moving between vortex triplet points. It must be noted that the closest neighbors of given vortex points have opposite topological charges.

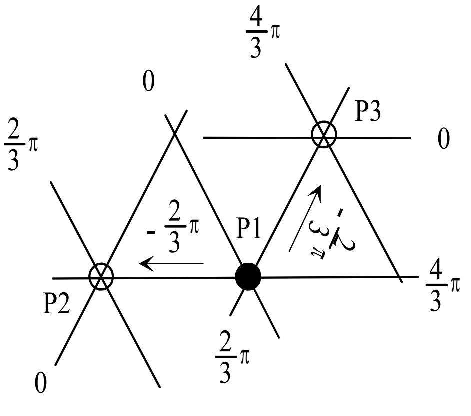

Fig. 4.23. An example of the vortex triplet geometry. This is a fragment of Figure 4.21. In this example points belonging to vortex triplet are neighbors, but they can be separated by many other vortex points

While moving from point P1 to P3, the phase of wave *B* does not change $\Delta\varphi 13_B = 0$ and the phase of wave *A* changes by $\Delta\varphi 13_A = -2/3\pi$. Thus, the phase difference between waves *B* and *A* changes by

$$\Delta\varphi 13_{BA} = \Delta\varphi 13_B - \Delta\varphi 13_A = \frac{2}{3}\pi \,. \tag{4.14a}$$

While moving from point P1 to P2, the phase of wave *A* does not change $\Delta\varphi 12_A = 0$ and the phase of wave *B* changes by $\Delta\varphi 12_B = -2/3\pi$. Thus, the phase difference between waves *A* and *B* changes by

$$\Delta\varphi 12_{BA} = \Delta\varphi 12_B - \Delta\varphi 12_A = -\frac{2}{3}\pi\,. \tag{4.14b}$$

Knowing the relative phase change while going from one vortex point to another, the following set of equations can be written

$$k_{xb}\,\Delta x1 + k_{yb}\,\Delta y1 - k_{xa}\,\Delta x1 - k_{ya}\,\Delta y1 = \Delta\varphi 13_{BA} + 2\pi\,n\,, \tag{4.15a}$$

$$k_{xb}\,\Delta x2 + k_{yb}\,\Delta y2 - k_{xa}\,\Delta x2 - k_{ya}\,\Delta y2 = \Delta\varphi 12_{BA} + 2\pi\,m\,. \tag{4.15b}$$

This can be rewritten as

$$k'_{xb}\,\Delta x1 + k'_{yb}\,\Delta y1 = \Delta\varphi 13_{BA} + 2\pi\,n\,, \tag{4.16a}$$

$$k'_{xb}\,\Delta x2 + k'_{yb}\,\Delta y2 = \Delta\varphi 12_{BA} + 2\pi\,m\,. \tag{4.16b}$$

The above set of equations has the solution

$$k'_{xb} = \frac{\Delta y2\,\Delta\varphi 12_{AB} - \Delta y1\;\Delta\varphi 13_{AB} + 2\,\Delta y2\,\pi\,n - 2\,\Delta y1\,\pi\,m}{\Delta y2\,\Delta x1 - \Delta x2\,\Delta y1}\,, \tag{4.17a}$$

$$k'_{yb} = \frac{\Delta x1\,\Delta\varphi 13_{AB} - \Delta x2\;\Delta\varphi 12_{AB} + 2\,\Delta x2\,\pi\,n - 2\,\Delta x1\,\pi\,m}{\Delta y2\,\Delta x1 - \Delta x2\,\Delta y1}\,, \tag{4.17b}$$

where $\Delta x1, \Delta x2, \Delta y1, \Delta y2$ are distances measured along axes *x* and *y* between points P1–P3 and P1–P2, respectively.

Solutions (4.17) show that there is a condition concerning vortex triplet that has to be observed

$$\Delta y2\;\Delta x1 - \Delta x2\;\Delta y1 \neq 0\,. \tag{4.18}$$

By solving the set of equations (4.12) for $\Delta yn1,\ \Delta yn2$, one can explore one more condition. The solution is

$$\Delta yn1 = \frac{\Delta xn1\,\Delta k_{xa} + (\Delta x1 - \Delta xn1)\,k'_{xb} + \Delta y1\,k'_{yb}}{k'_{yb} - \Delta k_{ya}}\,, \tag{4.19a}$$

$$\Delta yn2 = \frac{\Delta xn2\,\Delta k_{xa} + (\Delta x2 - \Delta xn2)\,k'_{xb} + \Delta y2\,k'_{yb}}{k'_{yb} - \Delta k_{ya}}\,. \tag{4.19b}$$

It is enough to consider the solutions (4.19a) only. Furthermore, rotation about the x-axis is assumed (i.e. $\Delta k_{xa} = 0$),), and vortex point pairs lying on the constant angle line are considered (i.e. $\Delta xn1 = \Delta x1 = 0$). It is also assumed that the constant angle lines are parallel to the y-axis. Under these conditions, equation (4.19a) becomes

$$\Delta yn1 = \frac{\Delta y1 k'_{yb}}{k'_{yb} - \Delta k_{ya}}. \tag{4.20}$$

The denominator of expression (4.18) is

$$k'_{yb} - \Delta k_{ya} = k_{yb} - \bar{k}_{ya}. \tag{4.21}$$

where the definitions (3.16) and relations $\Delta k_{ya} = k_{ya} - \bar{k}_{ya}$ were used. Here, $\bar{k}_{ya}$ means the y-coordinate of A wave vector after rotation. Formula (4.20) means that when $(k'_{yb} - \Delta k_{ya}) \rightarrow 0$ then the distance, measured along the constant angle line, between two neighboring vortex points increases to infinity and no measurement can be performed in this case. Expression (4.21) gives the simple geometric interpretation of this condition. When $(k'_{yb} - \Delta k_{ya}) \rightarrow 0$ then the y-coordinate of wave vector $\mathbf{k}_b$ becomes equal to the y-coordinate of the wave vector representing the rotated wave A. The vortex points move along the constant angle lines, which are parallel to the y-axis. So, in this case, both waves A and B encounter the same phase shift. But Figure 4.19 shows that when moving along the constant angle line from one vortex point to another, the phase of waves A and B cannot change simultaneously (the same can be said of waves A and C). This situation is illustrated in Figure 4.24, which shows the plot of $\Delta yn1$ against Δk_{ya}. The forbidden area (when $k_{yb} = \bar{k}_{ya}$) is seen. The question of how to avoid this area will be briefly discussed below. Before that, the rotation about the y-axis will be considered in respect of the question of OVI limitations.

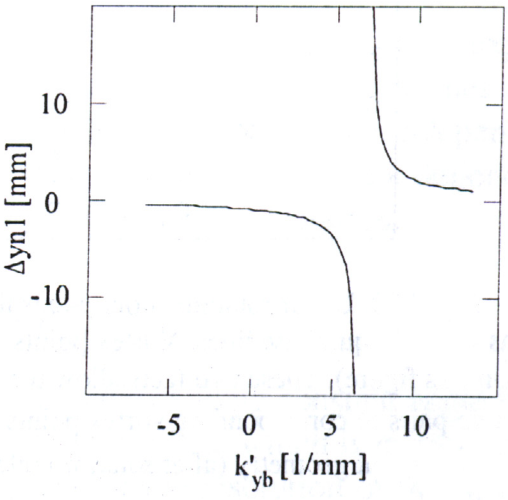

Fig. 4.24. Illustration of the relation (4.19) for the waves shown in figure 4.24. Wave vector value is $|\mathbf{k}| = 9929 [1/\text{mm}]$

It is still assumed that the y-axis of the coordinate system is oriented along a constant angle line. The y-axis rotation changes the orientation of equiphase lines of wave A (Fig. 4.21), but not its density measured along the constant angle line. This conclusion can be drawn from basic geometry of parallel lines in a plane. Hence, the y-axis rotation will not cause the problems described above. However, now the problem of identifying the corresponding vortex triplets, before and after rotation, occurs. Figure 4.25 shows an example of such a problem, i.e. the set of vortex points before and after the larger rotation about the y-axis. In the example shown in Figure 4.25, the x-coordinate of A wave vector has changed from zero to $\bar{k}_{xa} = k_{ya} = \bar{k}_{ya}$ and its y-coordinate remains the same. Because the x and y coordinates of A wave vector are the same (after rotation) its equiphase lines are now inclined at angle π/4 against the x-axis. The vortex pattern must change by the same angle. This example shows how to find the corresponding vortex points in general case.

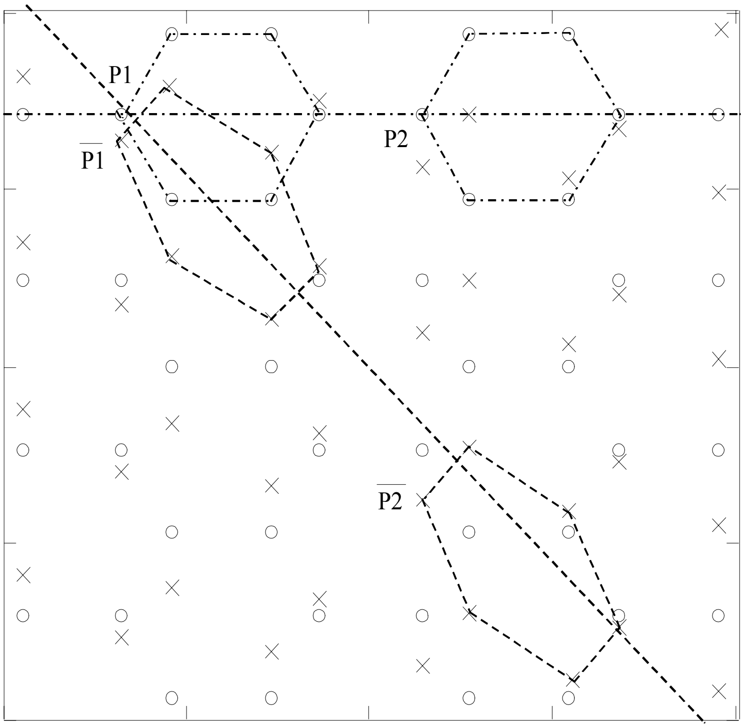

Fig. 4.25. Under rotation about y-axis the vortex points geometry is rotated at the same rate as wave A equiphase lines. Vortex points move along the constant angle lines (which are vertical in this figure). These two facts allow the corresponding vortex points to be found. In the figure two pairs of corresponding vortex points (P1, $\overline{\text{P}}$1) and (P2, $\overline{\text{P}}$2) are pointed. The characteristic vortex point geometry (after rotation) related to this interfering waves geometry is also outlined

Because of the forbidden area shown in Figure 4.23, not all angles can be measured by OVI. The range of measured angles depends on the relative angles between waves. The bigger these angles are, the wider range of angles can be measured. On the other hand, bigger angles mean more dense vortex points and less accurate measurements. In “micro-” and “nano-” science and technology (MEMS, for example [Trimmer *et al.* 2001]), many angles to be measured are very small. The OVI can be easily adapted for measuring the rotation of micro-elements. The simplest way is to add a microscopic objective at the position shown in Figure 4.17. In such a case, the limitations discussed here have no meaning. In other cases, a few solutions are possible.

One can read additional information from (*A*+*B*, *A*+*C*, *B*+*C*) interferograms. Studying these interferograms does not allow measuring small angles of rotation. But for the given system the rotation angles that are close to forbidden area are not small, so this method can work.

One more reference wave can be used. If the rotation angles come close to the forbidden area, then the system can be switched to other references with a different forbidden area. This makes the system more complicated, but solves the problem.

The rotated wave *A* can be split into two waves which meet two different sets of reference waves (having different forbidden areas). Such a two head interferometer is even more complicated, but the two separate measurements can be made simultaneously and no switching between waves is necessary.

Summarizing the following step is necessary to determine the small-angle rotations with OVI: The four interferograms (*A*+*B*, *B*+*C*, *A*+*C*, *A*+*B*+*C*) must be taken. Then, by applying localization procedures as described in section 4.3, the vortex points at *A*+*B*+*C* interferogram must be localized. After mirror RM rotation this measurement must be repeated. However, if the measurement system is stable and waves *A*, *B*, *C* are of high quality, then the *A*+*B*+*C* interferogram is sufficient. Using relations (4.13) the rotation angles can be determined.

The method presented was illustrated in the case of symmetrical interfering waves geometry; however, they can also be applied in general cases. In particular, the axis of the coordinate system does not have to be fixed as shown in Figure 4.18; however, this choice gives the clearest insight into the problem and can be easily found in experiment. It shows that there are two axes of rotation such that the equiphase lines shift differs in character when rotating around one or another. In effect, two independent angles of rotation can be determined. Since the system possibilities do not depend on the coordinate system, the same can be done in any x and y axis orientation.

4.5.1. Numerical examples

The qualitative experiment shows that vortex points move along constant angle lines of two reference waves when one of the mirrors is slightly tilted, which is in agreement with the theory presented above. The experimental test of the resolution of the method presented requires a mirror which can be precisely rotated with resolution of an arc second or below; however, such a system has not been available to the author yet.

OVI for small-angle rotations measurement was tested numerically under various conditions. First, the plane waves were used with and without 8-bit binarization. In the next step, the contributing waves were disturbed to simulate experimental conditions. In the examples presented, only quantities which can be measured in experiment (i.e. light intensities in interferograms) were used as input data. The calculations of angles of rotation were based on the procedures presented in the previous subsection. No statistics, except simple arithmetic averaging, were used. The calculations were based on two waves – rotated wave A, and one of the reference waves denoted by B. Calculations with wave pairs A, C were not performed. The amplitude of real plane waves are non-uniform. Fortunately, at each vortex point, they can be determined separately. This fact was used to increase the accuracy of the analysis performed. The simulations were performed for 8-bit black and white CCD camera having about 0.5 million of pixels.

In the numerical test presented, the system parameters are as follows: Before rotation: wave vector $\mathbf{k}_\mathbf{A}(0,\ -4.44,\ 9929.18)$ 1/mm. After rotation, these coordinates become $(0.496,\ -4.54,\ 9929.18)$ 1/mm. The light wavelength is 632.8 nm. Rotation angles are: –10.08 arc second about the y-axis and 2.016 arc second about the x-axis. Table 4.3 shows the results obtained for a few vortex triplets. The necessary quantities $\Delta k'_{xb}$, $\Delta k'_{yb}$ are extracted from formulas (4.17) after arithmetic averaging of the number of single results; they are $k'_{xb} = -3.778$ 1/mm, $k'_{yb} = 6.840$ 1/mm. The real values (defined numerically) were –3.846 1/mm and 6.661 1/mm, respectively. The average values of Δk_{xa}, Δk_{yb} calculated with the values from the last five rows in Table 4.3 are 0.502 1/mm and –0.111 1/mm, respectively. The true numerical values are 0.496 1/mm and –0.1 1/mm, respectively. In this case, errors are –0.006 1/mm and 0.012 1/mm, respectively. In this case, the change of wave vector coordinate by 0.25 1/mm means the rotation angle equal to 0.5 arc second. So the errors given in arc measure are 0.012 and 0.25 arc second, respectively. Other numerical examples including different interfering waves geometry – not necessarily as regular as in Figure 4.14 – give similar results. Generally, the simulations (for small angles) give results with an accuracy of 0.5 arc second or better for each axis.

Table 4.3 shows one more problem which was found by numerical simulations. The localization errors (of sub-pixel range) create additional calculation errors when using formulas (4.13). These errors can be large for some vortex triplets. Fortunately, it is easy to eliminate such wrong triplets. The expressions $\Delta xn1\Delta yn2 - \Delta xn2\Delta yn1$ and $\Delta y1\Delta xn2 - \Delta xn1\Delta y2$ should be greater than 5. Number 5 is a safety threshold and it was found in simulations by studying a number of numerical examples.

Numerical simulations show that the OVI can be used for measuring the small-angle rotations with accuracy better than arc second. This resolution can be improved using the higher resolution digital CCD camera. According to simulations, the CCD 12-bit camera which has one million pixels at 2/3 inch CCD element, enables the measurement of the rotation angle with a resolution of 0.05 arc second.

Table 4.3

Examples of Δk_{xa} and Δk_{yb} values determined in numerical experiment. Expression named "check 1" equals $\Delta xn1 \Delta yn2 - \Delta xn2 \Delta yn1$ and expression named "check 2" equals $\Delta y1 \Delta xn2 - \Delta xn1 \Delta y2$. The results for which both check1 and check 2 are greater than 5 are valid (last five rows in this table). The arithmetic average of valid values for Δk_{xa} and Δk_{yb} are 0.502 and –0.112, respectively. The real values are 0.496 and –0.099, respectively

No.	Δk_{xa} [1/mm]	Δk_{ya} [1/mm]	Check 1 [mm^2]	Check 2 [mm^2]
1	0.516	–0.294	1.5	–5.6
2	0.460	–0.074	3.0	–3.0
3	0.502	–0.100	2.3	–2.4
4	0.530	–0.110	9.1	–9.12
5	0.505	–0.121	7.1	–7.2
6	0.505	–0.122	6.1	–6.2
7	0.487	–0.113	6.0	–6.1
8	0.485	–0.093	7.0	–7.2

In conclusions the OVI dedicated for small-angle rotations measurement enables the determination of two independent angles of rotation. The effects of the system vibration can be subtracted. The system has simple and flexible construction, which can be adopted to meet various user requirements. The interferograms analysis is based on relatively simple and fast calculation procedures and strong statistical methods can be applied to improve the system resolution.

4.5.2. Other OVI applications

In the previous section, the discussion on OVI application for small rotation angles measurement was given. The possibility of 3-D interferometry was also mentioned. There are two more topics that are considered by the author and his coworkers. The first is OVI application for small wave front geometry reconstruction. This is one of the primary aims for the interferometry. The standard reconstruction is obvious and one example was presented in Figure 4.12. Standard here means that the wavefront geometry of the investigated waves is related to the wavefront of the reference wave. Thus, in order to know what is the wave geometry of the investigated wave, one must know what is the wave geometry of the reference wave. But to judge the quality of the reference wave with high accuracy is a hard task. The available methods (like parallel glass plates) require additional optical elements to be put into interferometer. This takes time and disturbs the gentle configuration of interfering waves. OVI allows the geometry of "on line" reference waves to be evaluated. The question of accuracy is still under investigation, but it seems that $\lambda/10$ is available in the simplest optical system without any additional measurements (the four interferogram procedure is enough). Thus, both reference waves B and C can be tested during standard measurements. Obviously, such measurement does not introduce any disturbance to the system and with computerized OVI can be very fast. To measure the reference waves geometry one has to compare the ideal distribution of vortex points with the real one. The shifts between this two nets and additional information from (A+B, A+C, B+C) interferograms are sufficient to evaluate reference waves phase disturbances. This is the most current research topic on OVI at the time when the monograph were submitted for publication. The other subject is superresolution. There are a few ideas how to win superresolution imaging with OVI. The simplest idea is directly based on the small-angle rotations measurement described above. If the incident A beam is focused onto a sample (here imaging in reflected light is considered) with a surface that is not flat, then a different area of this surface can be treated as a set of mirrors rotated at different angles. By moving the sample (or objective) and observing the dynamics of the vortex points in the OVs net, one can reconstruct the sample morphology.

Aksenov (Aksenov *et al.* 2004) has proposed a system based on OVI for turbulent atmosphere inspection. So far, Aksenov's work has been available for the author as a short communication and will not be discussed here. The author hopes that more independent research groups will start to work on OVI development and find more interesting applications.

4.6. Other optical vortices applications

At the moment the optical instruments based on the optical vortices are young and must work for success. One exception are optical manipulators, a devices used for small bio-molecules manipulations and trapping [Padgett & Allen 1997, Curtis *et al.* 2002]. The molecules are caught by laser beam possessing OVs and then they can be moved or rotated. Such manipulators seems to be well developed and practically tested.

The concept of superresolution microscopy using phase defects was introduced by Tychynsky [Tychynsky 1989, Tychynsky *et al.* 1989, 1994].

When the focused laser light scans the sample a number of phase defects (including optical vortices) are born in the reflected (or transmitted beam). A part of these defects propagate within zero order diffraction component and can be detected in image plane. The detected defects bring information about the object and can be used for the object geometry reconstruction.

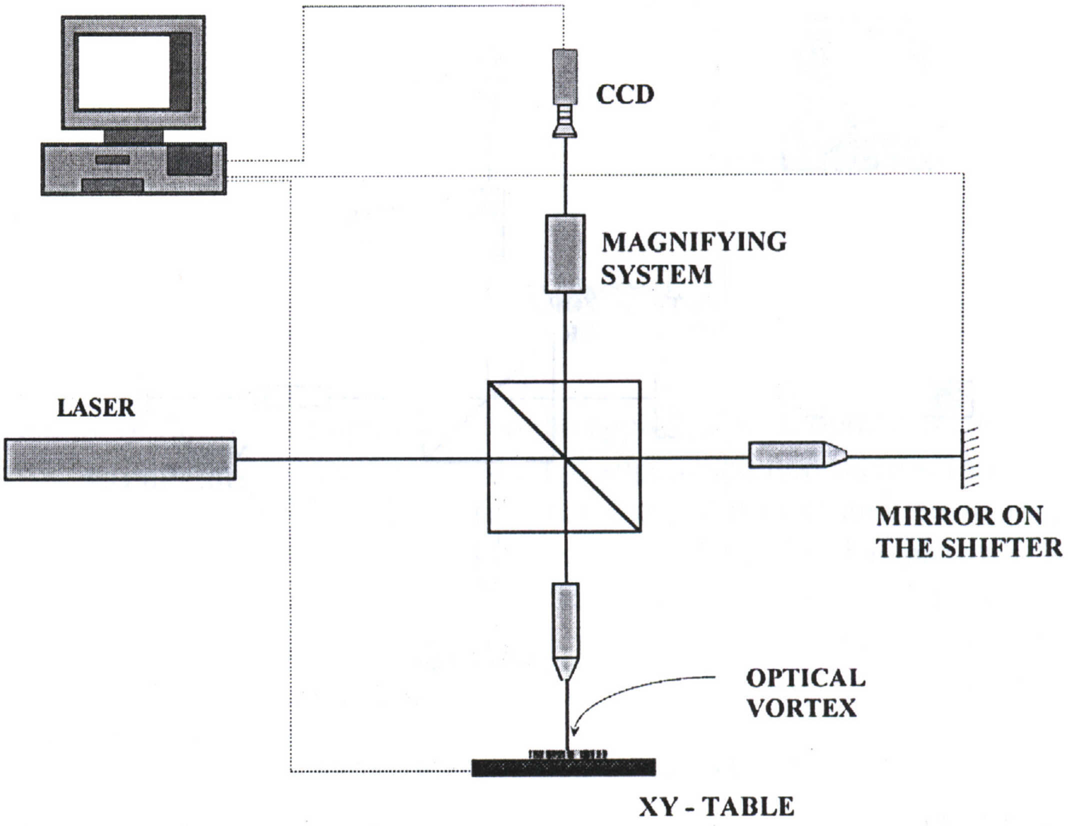

Fig. 4.26. SUPHIM – optical scheme

Figure 4.26 shows schematically optical system of such scanning microscope which is called SUPHIM (Superresolution Phase Image Microscope). This is a simple phase shifting interferometric system. The laser beam is focused by an microscopic objective of high numerical aperture. The reference beam is reflected by mirror mounted on the phase shifter (piezoelectric system for instance). The reference beam goes through the same optical path as the object beam (including microscopic objective of the same parameters). Both beams generate a fringe system, which is registered by CCD camera. The magnifying system (together with objective) has big power of order 10 000 times, which is far beyond the classical limits. The magnifying power should be enough to stretch the image of the center of focused beam over the whole CCD element. In classical phase shifting techniques the minimum three interferograms are necessary to reconstruct the phase of the investigate wave. However, if one needs to find dislocations at least four interferograms with four different phases of reference beam must be taken per one measurement. After each measurement the movable microscopic table is shifted to next position. The system operates under control of computer system, which after each measurement performs the interpretation of the interferograms. The SUPHIM has obvious advantages. It works in far field, does not need vacuum or special preparation of the sample. It scans the sample with low energy laser beam. However, the imaging theory has been not fully developed yet.

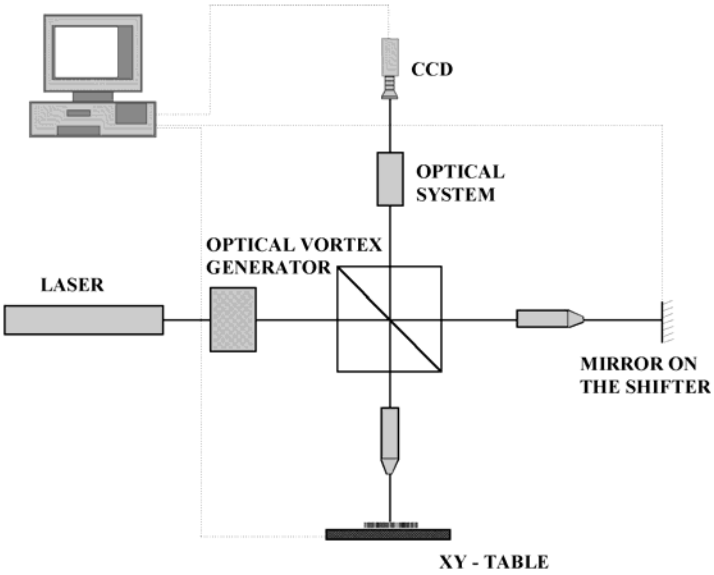

Fig. 4.27. OVSM – optical scheme

The SUPHIM setup, the scheme of which is shown in Figure 4.26, was also investigated by the author [Velzel *et al.* 1999]. However, the results obtained were ambiguous (see also [Totzeck *et al.* 1997]). As a consequence the author has decided to switch to the new project which is described below. The system is named Optical Vortex Scanning Microscope (OVSM). The simplest scheme for such a microscope is shown in Figure 4.27. The *optical vortex generator* (an appropriate hologram for instance) introduce to the scanning Gaussian beam an optical vortex. It can be single valued or multi-charge vortex. At the CCD the dynamics of the optical vortex in the diffracted beam is traced. Beams with star like structures are more sensitive to the sample morphology than the standard Gaussian beams. The vortex point is easy to trace by using the extra reference beam. While sample moves the characteristic fork like fringe also moves at the image plane. This movement is due to surfaces roughness. Thus the information on surface geometry can be retrieved from the vortex point (or points) dynamics analysis. This dynamics was studied in case of micro-step by applying calculations presented in section 2.4 [Masajada 2000c]. Results of more rigorous calculations will be presented in separate paper. Theoretical and numerical investigations show that such instrument could work with the resolution exceeding the classical limits. The simple experiments confirm the characteristic dynamics of vortex point, when the beam is diffracted by small rows. But the final conclusions can be drawn on the basis of well prepared experiment and this has not been performed yet. There are also some possibilities of combining the advantages of the OVI and OVSM in one single instrument, which is a subject of further investigations.

5. Summary

The author of this monograph works on the applications of optical vortices to optical measurements. The first works were devoted to superresolution microscopy – SUPHIM project [Velzel 1999]. The SUPHIM was a commercial project and it was stopped before introducing the new microscope into the market. The author has proposed a simpler version of the microscope working with optical vortices – OVSM. In the OVSM the sample is scanned with focused laser beam carrying OV. Under disturbances introduced by the sample, the vortex points, in the reflected beam move in a characteristic way. Thus, at least simple morphological structures of submicron size (like grooves, holes), can be identified by observing the behavior of a vortex point in focused Gaussian beam. The numerical tests have shown that the OVSM resolution goes beyond the classical limits. Simultaneously, the author has worked on simple technology for manufacturing synthetic holograms generating optical vortices (see section 3.2).

While studying OVSM a new concept concerning new kind of interferometer – namely OVI – was born, resulting in the discontinuation of investigations on OVSM, and all efforts were focused on developing OVI.

It should be emphasized that OVI represents a new kind of interferometry. Although the regular net of vortex points is generated by a three plane waves interference, the OVI is not a simple extension of two beam interferometry. The three plane waves method is used because it is technically simple and gives a natural decomposition of a vortex points net into three plane waves. This decomposition allows vortex points to be localized fast and accurately, as was shown in section 4.3. The relative phases between interfering waves can also be determined.

The most interesting option is to use the vortex point net dynamics for optical measurements. Instead of determining the relative phases between interfering waves, the changes in vortex points positions are traced. Tracing the movement of vortex points in a vortex point net is a new problem in interferometry. Since vortex points are stable and well localized objects in the OVI interference field, the changes in their position can be determined with high accuracy. This in turn gives a high measurement precision.

Both possibilities – i.e. relative angles and vortex points' movement determination – can be used simultaneously. For example, information on relative phases between interfering waves was used to compensate for the amplitude errors in small-angle rotations measurement.

The measurement of small-angle rotations, as presented in section 4.5, reveals the great potential of OVI. Using simple optical arrangements the rotation angles about two perpendicular axes can be determined with high accuracy. In other interferometric systems designed for this purpose and working with comparable resolution, the simultaneous measurement of two angles means that the optical system needs the second measurement channel. This results in a more complicated optical and electronic system. The physical concept of small-angle rotations measurement with OVI is simple and free of ambiguities contrary to some of the classical interferometric systems. Moreover, the influence of rotating element vibration is subtracted automatically, which is not the case in classical interferometric systems.

The OVI is open for further development in many possible directions. While finishing this work some new OVI properties were discovered. For example it is now known that the geometry of positive vortex points net (or negative vortex points net) does not depend on interfering waves amplitudes. Here positive (negative) vortex points net means all vortex points of positive (negative) topological charge. Amplitudes of interfering waves define the relative orientation of these two vortex points nets. This fact is important when considering OVI application for the wavefront geometry reconstruction. These new results are not explored in this monograph.

Apendix A

A.1. Introduction

The simplest solutions of the wave equation are plane and spherical waves. Both of these solutions are often used for modeling in geometrical and physical optics. However, for many physical problems, including the modeling of light emitted by laser, they are not sufficient. Contrary to plane waves lasers beams are confined to a well defined region. The divergence or convergence of laser beams are also specific and generally cannot be described by spherical waves. To represent laser beams Kogelnik used so called Gaussian beams. Gaussian beams are circularly symmetric beams, which meet the wave equation in parabolic approximation. In fact, one can define a family of functions which are the solutions of wave equation (in parabolic approximation) and characterize some aspects of laser beams. The family members share some core structures.

A.2. Basic Gaussian beam

The basic Gaussian beam is the simplest member of the whole family of beams representing intricate structure of laser radiation. In cylindrical coordinates (ρ, φ, z) it can be given as

$$U(\rho,\varphi,z) = U_0 \frac{w_0}{w_z} \exp\left\{-\frac{\rho^2}{w_z^2}\right\} \exp\left\{i\left(\frac{k\,\rho^2}{2R_z} - \operatorname{atan}\left(\frac{z}{z_R}\right) + k\,z - \omega t\right)\right\} \qquad \text{(A1)}$$

where E_0 is the beam amplitude, w_0 is the waist parameter,

$$w_z = w_0\sqrt{(1 + z^2 / z_R^2)}\ , \qquad \text{(A1a)}$$

is the transversal beam dimension in z plane. This value gives the radial distance where the light pseudo-amplitude (i.e. the square root of light intensity $\sqrt{I_0}$) has dropped from the maximum value $\sqrt{I_0}$ in the center $(\rho = 0)$ to $\sqrt{I_0}/e$ for $\rho = w_z$. For $z = 0$ one gets $w_z = w_0$, i.e. the beam waist is the transverse beam dimension at position where beam wavefront is flat (waist plane) and by convenience the origin of the coordinate system is in this plane. In the beam waist plane the beam energy has the narrowest distribution.

$$R_z = z(1 + z_R^2 / z^2) \tag{A1b}$$

is the wavefront curvature and

$$z_R = k\, w_0^2 / 2 \tag{A1c}$$

is the Rayleigh range. It describes the point where the intensity on axis has dropped to half the value in the waist plane and the waist enlarges by the factor $\sqrt{2}$ (Fig. A1). The beam waist can be treated as focus point of the beam and the value $2z_R$ is frequently described as the depth of focus or as the confocal parameter. The $-\mathrm{atan}(z/z_R)$ is called the Gouy phase, which changes from 0 for $z = 0$ to $-\pi/2$ for $z \to \infty$.

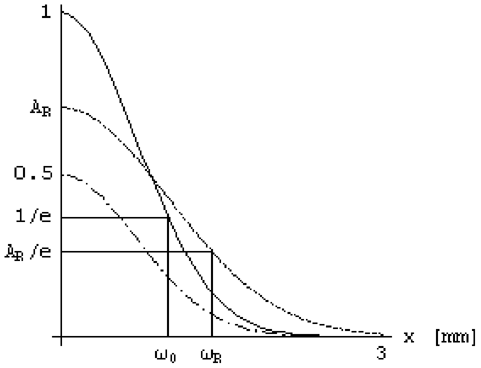

Fig. A1. The solid line shows the pseudo-amplitude of Gaussian beam in the waist plane. The dotted line shows its pseudoamplitude in Rayleigh plane. The dotted lone shows the beam intensity in Rayleigh plane

The beam (A1) has a Gaussian like transverse intensity distribution, hence the beam name. The Gaussian beam (A1) has variable wavefront curvature (A1b). For $z = 0$ one gets $R_z = \infty$, i.e. the wavefront is flat. For $z >> z_R$ the wavefront becomes spherical like and the beam transversal size w_z depends linearly on z. The beam has a constant divergence angle of

$$\Xi = \frac{2\pi\lambda}{2w_0}. \tag{A2}$$

Under propagation through the optical system with axially symmetric components that can be described in parabolic approximation the Gaussian beams remain Gaussian. This means that the beam emerging from the system will be Gaussian again, however, now with a new position of the waist.

There are many detailed studies devoted to the different aspects of Gaussian beams. One can find an example of such studies in [Siegman 1986, Bachor 1998]. An interesting discussion on the validity of paraxial approximation can be found in a paper by Lax [Lax 1975].

A.3. Hermite–Gauss modes

The Gaussian beam (A1) is not the only stable solution of paraxial wave equation. There are many other spatial solutions which are physical real, i.e. they can be emitted by laser and propagate without change in shape. The well known set of such solutions are the Hermite–Gauss (HG) beams. They have the same paraboloidal wavefront curvature as the Gaussian beam. Their intensity distribution is fixed and scales with R_z. However, they have non-Gaussian intensity distribution. These solutions can be represented as a product of two Hermite functions [Byron *et al.* 1972], one in the *x*, and other in the *y* direction.

$$u_{mn}^{HG} = U_0 \cdot A_{mn}^{H} \cdot \frac{w_0}{w_z} \, H_m\!\left(\frac{\sqrt{2}\,x}{w_z}\right) H_n\!\left(\frac{\sqrt{2}\,y}{w_z}\right) \exp\left\{-\frac{x^2+y^2}{w_z^2}\right\}$$

$$\exp\left\{-i\left[\frac{k\rho^2}{2R_z} - (m+n+1)\,\mathrm{atan}\!\left(\frac{z}{z_R}\right) + k\,z\right]\right\}, \tag{A3}$$

where A_{nm}^{H} is a normalization constant, H_n are Hermite polynomials of order *n*. In particular, $H_0(x)=1$ and $u_{0,0}^{H}$ is the pure Gaussian beam described above.

The HG mode rotated by $\pi/4$ can be expanded into the set of non-rotated HG modes [Allen *et al.* 1999]:

$$u_{nm}^{HG}\left(\frac{x+y}{\sqrt{2}}, \frac{x-y}{\sqrt{2}}, z\right) = \sum_{k=0}^{m+n} b(n,m,k)\, u_{m+n-k,k}^{HG}(x,y,z)\,, \tag{A4}$$

$$b(n,m,k) = \sqrt{\frac{(n+m)!\,k!}{2^{n+m}\,n!\,m!}}\;\frac{1}{k!}\frac{\mathrm{d}^k}{\mathrm{d}t^k}\left[(1-t)^n\,(1+t)^m\right]\Big|_{t=0}\,. \tag{A4a}$$

This relation is important when analyzing a transformation of HG modes into LG modes.

The HG modes form a complete basis set in function space and any arbitrary field distribution can be described by superposition of these modes. The Hermite polynomials have rectangular symmetry and the laser system has usually circular symmetry. However, small asymmetries in the laser cavity give rise to the rectangular symmetry in the output field. This makes the HG modes an effective way to represent the intricate structure of laser radiation (Fig. A.2). It is worth noting here that by special cavity attenuation one can obtain from the laser the desired pure HG mode [Oron *et al.* 2001].

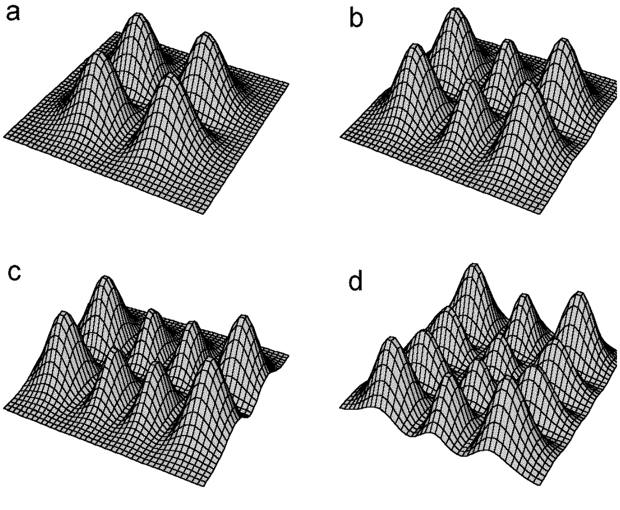

Fig. A2. Light intensity distribution in HG modes in the beam waist plane.
a) $n = 1$, $m = 1$; b) $n = 2$, $m = 1$; c) $n = 3$, $m = 1$; d) $n = 2$, $m = 3$. The plots have different z-scales

A.4. Laguerre–Gauss modes

The other modes that form a complete basis set are Laguerre–Gauss (LG) modes. Their field amplitude can be given as:

$$u_{nm}^{LG} = U_0 \cdot A_{lm}^{L} \cdot \frac{w_0}{w_z} \left(\frac{\rho\sqrt{2}}{w_z} \right)^{l} \exp\left\{ -\frac{\rho^2}{w_z^2} \right\} L_p^l \left(\frac{2\rho^2}{w_z^2} \right)$$

$$\exp\left\{ -i \left[\frac{k\rho^2}{2R_z} + i\,l\,\varphi + (l+p+1)\,\mathrm{atan}\left(\frac{z}{z_R} \right) + k\,z \right] \right\}, \qquad \text{(A.5)}$$

where A_{lm}^{L} is the normalization constant, $L_p^l(x)$ is the generalized Laguerre polynomial [Byron *et al.* 1979], $l = m - n$, and $p = \min(n, m)$. It is more usual to use the indices l, p instead of n, m when describing LG modes, so in formula (A5) we could write u_{lp}^{LG} instead of u_{mn}^{LG}. The characteristic feature for these modes is the azimuthal phase term $\exp\{-i\,l\,\varphi\}$, which gives rise to the helical wavefronts and non-zero orbital angular momentum of the beam.

As each of the HG and LG modes form the complete basis set in function space any LG modes can be expressed in terms of HG modes as follows [Allen *et al.* 1999]:

$$u_{nm}^{LG}(x,y,z)=\sum_{k=0}^{m+n} i^k\, b(n,m,k)\, u_{m+n-k,k}^{HG}(x,y,z) \tag{A6}$$

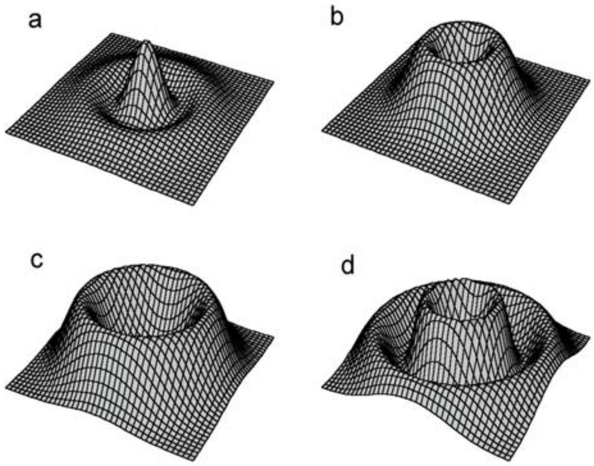

Fig. A3. Light intensity distribution in LG modes in the beam waist plane.
a) p = 1, l = 0; b) p = 0, l = 1; c) p = 0, l = 3; d) p = 1, l = 2. The plots have different z-scales

A.5. "Helical–Gaussian" beam

Apart from the beams with OVs, which are well known in laser physics, in many papers "helical Gaussian" beams are introduced. These beams are the simplest beams with Gaussian envelope and fundamental properties characteristic of beams with single or multicharge OV satisfying the wave equation in parabolic approximation. In the case of topological charge value m = 1 and topological charge sign $sgn = \pm 1$, the beam is Laguerre–Gaussian beam with parameters p = 0 and l = 1. The beam can be described by the formula

$$U(x,y,z)=U_0\frac{w_0}{w_z^{m+1}}(x+i\,sgn\,y)^m\exp\left\{-\frac{x^2+y^2}{w_z^2}\right\}$$
$$\exp\left\{i\left(\frac{k(x^2+y^2)}{2R_z}-(m+1)\,\mathrm{atan}\left(\frac{z}{z_R}\right)\right)\right\}\exp\{ikz\}. \tag{A7}$$

In cylindrical coordinates formula (A7) transforms into:

$$U(\rho,\varphi,z) = U_0 \frac{w_0}{w_z^{m+1}} \rho^m \exp\left\{-\frac{\rho^2}{w_z^2}\right\} \exp\{i\, sgn\, m\, \varphi\}$$

$$\exp\left\{ i \left(\frac{k\rho^2}{2R_z} - (m+1)\,\mathrm{atan}\left(\frac{z}{z_R}\right)\right)\right\} \exp\{i k z\}. \qquad \text{(A8)}$$

In this monograph, the following definition is used:

$$A = \frac{1}{w_z^2} - \frac{ik}{2R_z}. \qquad \text{(A9)}$$

Appendix B

List of symbols and abbreviations

In this appendix a list of most frequently used symbols is given. The symbols are valid throughout the whole monograph and are never redefined. Together with symbols, a list of abbreviations and definitions introduced by the author is included. The abbreviations and definitions are explained explicitly or by referring to the proper page in the monograph.

A	One of the waves generating OVI vortex net.
B	One of the waves generating OVI vortex net.
BV	See page 60
C	One of the waves generating OVI vortex net.
CAV	Complex amplitude vector.
Φ_G	The Gouy phase shift, see Appendix A.
$\mathbf{k}$, k	Wave vector, wave vector magnitude.
m	Value of topological charge of optical vortex.
OV	Optical vortex.
OVI	Optical Vortex Interferometer/Interferometry.
OVI-plane	See page 72
OVs	Optical vortices.
OVSM	Optical Vortex Scanning Microscope.
sgn	The sign of topological charge of optical vortex.
SUPHIM	Superresolution Phase Image Microscope.
U	Complex amplitude representing light wave in scalar approximation.
U_0	Amplitude of light wave.
Vortex triplet	See page 75

References

Abramochkin E.G., Volostnikov V.G., 1996, *Spiral-type beams: optical and quantum aspects*, Opt. Commun., **125**, 3020–3023.

Abramochkin E.G., Losevsky N., Volostnikov V., 1997, *Generation of spiral-type laser beams*, Opt. Commun., **141**, 59–64.

Ackemann T., Kriege E., Lange W., 1995, *Phase singularities via nonlinear beam propagation in sodium vapor*, Opt. Commun., **115**, 941–950.

Aksenov V., Tikhomirova O., 2002, *Theory of Singular-Phase Reconstruction for an Optical Speckle Field in the Turbulent Atmosphere*, J. Opt. Soc. Am., A, **19,** 345–355.

Aksenov V. Tikhomirova O., 2004, The work was presented at NATO Workshop on Singular Optics in Kiev 2003 and is to be published in J. Opt. A Special Issue: Singular Optics.

Allen L., Beijersbergen M.W., Spreeuw R.J.C., Woerdman J.P., 1992, *Orbital angular momentum of light and the transformation of Laguerre–Gaussian laser modes*, Phys. Rev. A, **45**, 8185–8189.

Allen L., Lembessis V.E., Babiker M., 1996, *Spin-orbit coupling in free-space Laguerre–Gaussian light beams*, Phys. Rev. A., **53**, 2937–2939.

Allen L., Padgett M.J, Babiker M., 1999, *The orbital angular momentum of light*, Progress in Optics, E. Wolf (Ed.), Vol. **39**, Chapter IV.

Allen L., 2002, *Introduction to the atoms and angular momentum of light special issue*, J. Opt., B, **4**, 1–6.

Angelsky O.V., Besha R.N., Mokhun I.I., 1997, *Appearance of wave front dislocations under interference among beams with simple wave fronts*, Opt. Appl., **37**, 273–278.

Arlt J., Dholakia K., Allen L., Padgett M.J., 1998, *The production of multiringed Laguerre–Gaussian modes by computer-generated holograms*, J. Mod. Opt., **45**, 1231–1237.

Arlt J., Dholakia K., Allen L., Padgett M.J., 1999, *Parametric down-conversion for light beams possessing orbital angular momentum*, Phys. Rev., A., **59**, 3950–3952.

Arnold V.I., 1986, *Catastrophe theory*, Springer, Berlin.

Azzam R.M.A., Bashara N.M., 1977, *Ellipsometry and polarized light*, North-Holland Publishing Company, Amsterdam.

Bachor H., 1998, *A Guide to Experiments in Quantum Optics*, Wiley, New York.

Baranova N.B., Mamaev A.V., Pilipetsky N.F., Shkunov V.V., Zel'dovich B.Ya., 1983, *Wave-front dislocations: topological limitations for adaptive systems with phase conjugation*, J. Opt. Soc. Am., **73**, 525–528.

Barnett S.M., Allen L., 1994, *Orbital angular momentum and nonparaxial light beams*, Opt. Commun., **110**, 670–678.

Basisty I.V., Soskin M.S., Vasnetsov M.V., 1995, *Optical wavefront dislocation and their properties*, Opt. Commun., **119**, 604–612.

Bazhenov V.Yu., Soskin M.S., Vasnetsov M.V., 1992, *Screw dislocation in light wavefronts*, J. Mod. Opt., **39**, 985–990.

Beijersbergen M.W., Coerwinkel R.P.C., Kristensen M., Woerdman J.P., 1994, *Helical-wavefront laser beam produced with a spiral phaseplate*, Opt. Commun., **112**, 321–327.

Berry M.V., 1978, *Disruption of wavefronts: statistics of dislocations in incoherent Gaussian random waves*, J. Phys., A, **11**, 27–37.

Berry M.V., Upstill C., 1980, *Catastrophe optics: morphologies of caustics and their diffraction patterns*, Progress in Optics, **18**, Chapter III.

Berry M.V., 1981, *Singularities in waves and rays*, Physics of Defects, Les Houches Session 35, 1980, R. Balian, M. Kléman, J.P. Poirier (Eds.), North–Holland, course 7.

Berry M.V., Dennis M.R., 2001, *Polarization singularities in isotropic random vectors waves*, Proc. Roy. Soc. Lond., A., **457**, 141–155.

Berry M.V., *Coloured phase singularities*, 2002, New Journal of Physics, **4**, 1–14.

Beth R.A., 1936, *Mechanical detection and measurement of the angular momentum of light*, Phys. Rev., **50**, 115–125.

Born M., Wolf E., 1991, *Principles of Optics*, Chapter VIII, Pergamon Press, sixth edition.

Brambilla M., Lugiato L.A., Penna M.V., Prati F., Pagani P., Vanotti P., Li M.Y., Wiess C.O., 1991, *Transverse laser patterns. I. Phase singularity crystals*, Phys. Rev., A., **43**, 145–164.

Brand G.F., 1997, *Generation of millimeter-wave beams with phase singularities*, J. Mod. Opt., **44**, 1243–1248.

Brand G.F., 1988a, *Millimeter-wave beams with phase singularities*, IEEE Transactions on Microwave Theory and Techniques, **46**, 948–951.

Brand G.F., 1998b, *The generation of phase singularities at millimeter wavelengths by the use of a blazed grating*, J. Mod. Opt., **45**, 215–220.

Brand G.F., 1999a, *Rotating-mode content of gyrotron output*, Appl. Phys. Lett., **75**, 1320–1322.

Brand G.F., 1999b, *Phase singularities in beams*, Am. J. Phys., **67**, 55–60.

Bryngdahl O., 1973, *Radial and circular-fringe interferograms*, J. Opt. Soc. Am., **63,** 1098–1104.

Bryngdhal O., 1974, *Geometrical transformations in optics*, JOSA, **64**, 1092–1099.

Bryngdahl O., Lee Wai-Hone, 1974, *Shearing interferometry in polar coordinates*, J. Opt. Soc. Am. 1606–1615.

Byron F.W., Fuller R.W., 1972, *Mathematics of classical and quantum physics*, vol. 2, Addison–Wesley Inc., Massachusetts.

Coats A.B., Weiss C.O., Green C.D., D'Angelo E.J., Tredicce J.R., Brambilla M., Cattaneo M., Lugiato L.A., Pirovano R., Prati F., Kent A.J., Oppo G.L., 1994, *Dynamical transverse patterns II. Experiments*, Phys. Rev., **49**, 1452–1469.

Coullet P., Gil L., Rocca F., 1989, *Optical Vortices*, Opt. Commun., **73**, 403–408.

Courtial J., Dholakia K., Allen L., Padgett M.J., 1997, *Second-harmonic generation and the conservation of orbital angular momentum with high-order Laguerre–Gaussian modes*, Phys. Rev. A, **56**, 4193–4196.

Courtial J., Padgett M.J., 1999, *Performance of a cylindrical lens mode converter for producing Laguerre–Gaussian laser modes*, Opt. Commun., **159**, 13–18.

Creath K., 1998, *Phase-measurement interferometry techniques*, Progress in Optics, **26**, chapter V.

Curtis J.E., Koss B.A., Grier D.G., 2002, *Dynamic holographic optical tweezers*, Opt. Commun., **169**, 169–175.

Dholakia K., Simpson N.B., Padgett M.J., 1996, *Second-harmonic generation and the orbital angular momentum of light*, Phys. Rev., A, **54**, 3742–3745.

Erdèlyi A., (Ed.), 1953, *Tables of integral transforms*, McGraw–Hill, New York.

Freund I., Shvartsman N., Freilikher V., 1993, *Optical dislocations networks in highly random media*, Opt. Commun., **101**, 247–264.

Freund I., 1994, *Optical vortices in Gaussian random wave fields: statistical probability densities*, JOSA A, **11**, 1644–1652.

Freund I., Shvartsman N., 1994, *Wave-field phase singularities: The sign principle*, Phys. Rev., A, **50**, 5164–5172.

Freund I., 1995, *Saddles, singularities and extrema in random phase fields*, Phys. Rev., E, **52**, 2348–2360.

Freund I., Freilikher V., 1997, *Parametrization of anisotropic vortices*, J. Opt. Soc. Am., A, **14**, 1902–1910.

Freund I., 2001, *Polarization flowers*, Opt. Commun., 2001, 47–63.

Fried D.L., Vaughn J.L., 1992, *Branch cuts in the phase function*, Appl. Opt., **31**, 2865–2882.

Gahagan K.T., Swartzlander G.A. Jr., 1999, *Simultaneous trapping of low-index and high-index particles*, J. Soc. Am., B, **16**, 533–537.

Gbur G., Visser T.D., Wolf E., 2002, *Anomalous behavior of spectra near phase singularities of focused waves*, Phys. Rev. Lett., **88**, no. 013901.

Ghiglia D.C., Pritt M.D., 1998, *Two-dimensional phase unwrapping*, Wiley, New York.

Goodman W., 1968, *Introduction to Fourier optics*, McGraw-Hill, New York.

Gu M., Gan X.S., 1997, *Fresnel diffraction by a circular plane with optical phase singularities and its effect on the intensity distribution in the focal plane of a lens*, Optik, **105**, 51–56.

Hajnal J.V., 1987a, *Singularities in the transverse fields of electromagnetic waves*, *I. Theory*, Proc. Roy. Soc. Lond., A, **414**, 433–446.

Hajnal J.V., 1987b, *Singularities in the transverse fields of electromagnetic waves*, *II. Observations on the electric field*, Proc. Roy. Soc. Lond., A, **414**, 447–468.

Hajnal J.V., 1990, *Observations of singularities in the electric and magnetic fields of freely propagating microwaves*, Proc. Roy. Soc. Lond. A., **430**, 413–421.

Harris M., Hill C.A., Tapster P.R., Vaughan J.M., 1994a, *Laser modes with helical wave fronts*, Phys. Rev. A., **49**, 3119–3122.

Harris M., Hill C.A., Vaughan J.M., 1994b, *Optical helices and spiral interference fringes*, Opt. Commun., **106**, 161–166.

He H., Friese M.E.J., Heckenberg N.R., Rubinsztein-Dunlop H., 1995, *Direct observation of transfer of angular momentum to absorptive particles from a laser beam with phase singularities*, Phys. Rev. Lett., **75**, 826–829.

Heckenberg N.R., McDuff R., Smith C.P., Rubinsztein-Dunlop H, Wegener M.J., 1992, *Laser beams with phase singularities*, Opt. Quant. Elect., **24**, 951–952.

Indebetouw G., 1993, *Optical vortices and their propagation*, J. Mod. Opt., **40**, 73–87.

Indebetouw G., Korwan D.R., 1994, *Model of vortices nucleation in a photorefractive phase-conjugate resonator*, J. Mod. Opt., **41**, 941–950.

Jarosławski J., 2003, diploma works of Institute of Physics, Wrocław University of Technology, (in Polish).

Khonina S.N., Kotlyar V.V., Shinkaryev M.V., Soifer V.A., Uspleniev G.V., 1992, *The phase rotor filter*, J. Mod. Opt., **39**, 1147–1154.

Krauss H.G., 1988, *Huygens–Fresnel–Kirchhoff wave front diffraction formalism: paraxial and exact Gaussian laser beams*, J. Opt. Soc. Am., A, **7**, 430–434.

Kravtsov Yu.A., Orlov Yu.I., 1990, *Geometrical optics of inhomogeneous media*, Springer, Berlin.

Kravtsov Yu.A., Orlov Yu.I., 1993, *Caustics, catastrophes and wave fields*, Springer, Berlin.

Larkin K.G., Bone D.J., Oldfield M.A., 2001, J. Opt. Soc. Am. A, **18**, 1862–1870.

Larkin K.G., 2001, *Natural demodulation of two-dimensional fringe patterns*, *II. Stationary phase analysis of the spiral phase quadrature transform*, Opt. Soc. Am., A, **18**, 1871–1881.

Lax M., 1975, *From Maxwell to paraxial wave optics*, Phys. Rev., A, **11**, 1365–1370.

Lu Y.C., *Singular theory and introduction to catastrophe theory*, Springer Verlag, New York, Berlin.

Malacara D., Servin M., Malacara Z., 1998, *Interferogram analysis for optical testing*, Marcel Dekker, New York.

Masajada J., Nowak J., 1994, *Glass lenses with deposited diffractive microstructure – numerical analysis of the image quality*, Optik, **98**, 61–64.

Masajada J., 1998, *Simple synthetic holograms for optical vortices generation*, SPIE Proc., **3820**, 96–102.

Masajada J., 1999, *Synthetic holograms for optical vortex generation – Image evaluation.* Optik, **110**, 554–558.

Masajada J., 2000a, *Half-plane diffraction in the case of Gaussian beams containing an optical vortex*, Opt. Commun., **175**, 289–294.

Masajada J., 2000b, *Gaussian beams with optical vortex of charge 2- and 3-diffraction by a half-palne and slit*, Opt. Appl., **30**, 247–256.

Masajada J., 2000c, *Gaussian beams with optical vortices diffraction by simple objects*, SPIE Proc., **4356**, 178–181.

Masajada J., 2001, *Phase measurements with optical vortices as a phase markers*, EOS Topical Meetings Digest Series (CD version), **30**, 52–53.

Masajada J., Dubik B., 2001, *Optical vortex generation by three plane wave interference*, Opt. Commun., **198**, 21–27.

Masajada J., Popiołek-Masajada A., Wieliczka D., 2002, *The interferometric system using optical vortices as a phase markers*, Opt. Commun., **207**, 85–93.

Masajada J., Popiołek-Masajada A., Frączek E., Frączek W., 2004, *Vortex points localization problem in optical vortices interferometry*, Opt. Commun., **234**, 23–28.

Masajada J., 2004a, *Singular Optics*, SPIE Proc., **5259**, 66–74.

Masajada J., 2004b, *Small rotation angles measurement with OVI*, Opt. Commun., in press (available electronically).

Meyer-Arendt J.R., 1972, *Introduction to classical and modern optics*, Prentice–Hall, Englewood Cliffs, Section 2.3.

Nye J.F., Berry M.V., 1974, *Dislocations in wave trains*, Proc. Roy. Soc. Lond., A **336**, 165–189.

Nye J.F., 1983, *Polarization effects in the diffraction of electromagnetic waves: the role of disclinations*, Proc. R. Soc. Lond., A **387**, 105–132.

Nye J.F., Hajnal J.V., 1987, *The wave structure of monochromatic electromagnetic radiation*, Proc. R. Soc. Lond., A., **409**, 21–36.

Nye J.F., 1999, *Natural focusing and fine structure of light*, IoP, Bristol and Philadelphia.

O'Neil A., Courtial T., 2000, *Mode transformations in terms of the constituent Hermite–Gaussian or Laguerre–Gaussian modes and the variable-phase mode converter*, Opt. Commun., **181**, 35–45.

Oron R., Nir D., Asher F.A., 2001, *Transverse mode shaping and selection in laser resonators*, Progress in Optics, **42**, chapter VI.

Padgett M., Arlt J., Simpson N., Allen L., 1996, *An experiment to observe the intensity and phase structure of Laguerre–Gaussian laser modes*, Am. J. Phys., **64**, 77–82.

Padgett M.J., Allen L., 1997, *Optical tweezers and spanners*, Phys. World, **9**, 35–38.

Padgett M.J., Allen L., 2002, *Orbital angular momentum exchange in cylindrical-lens mode convertors*, J. Opt., B, **4**, 17–19.

Pearson J.E., McGill T.C., Kurtin S., Yarif A., 1969, *Diffraction of Gaussian laser beams by semi-infinite plane*, J. Opt. Soc. Am., **59**, 1440–1445.

Peterson L.E.R., Smith Glenn S., 2002, *Three-dimensional electromagnetic diffraction of a Gaussian beam by a perfectly conducting half-plane*, JOSA A, **19**, 2265–2280.

Petrov D.V., Torner L., 1997, *Second-harmonic generation by intense beams containing phase dislocations: self-breaking into sets of solitons*, Opt. Quant. Elect., **29**, 1037–1046.

Popescu G., Dogariu A., 2002, *Spectral anomalies at wave-front dislocations*, Phys. Rev. Let., **88**, no. 183902.

Popiołek-Masajada A., Masajada J., Stefaniak E., 2003, *Optical vortices aided interferometry*, SPIE Proc., **5259**.

Poston T., Stewart I., 1978, *Catastrophe theory and its applications*, Pitman, Boston.

Przerwa-Tetmajer T., 2002, *Syntetyczne hologramy generujące zadane fronty falowe*, diploma thesis, Institute of Physics, Wrocław University of Technology, (in Polish).

Ratajczyk F., 2000, *Dwójłomność i polaryzacja optyczna*, Oficyna Wydawniczna Politechniki Wrocławskiej, Wrocław.

Roux F.S., 1993a, *Implementation of general point transform with diffractive optics*, Appl. Opt., **32**, 4972–4978.

Roux F.S., 1993b, *Diffractive optical implementation of rotation transform performed by using phase singularities*, Appl. Opt., **32**, 3715–3719.

Roux S.F., 1995, *Dynamical behavior of optical vortices*, J. Opt. Soc. Am., B, **12**, 1215–1221.

Rozas D., Sacks Z.S., Swartzlander G.A., Jr., 1997, *Propagation dynamics of optical vortices*, J. Opt. Soc. Am., B, **14**, 3054–3065.

Rozanov N., 1993, *O formirovanii izlučenija s dislokacijami volnovo fronta*, Opt. i Spekt., **75**, 861–867, (in Russian).

Russ J.C., 1995, *The Image Processing*, CRC Press, London.

Schechner J., 1996, *Parameterization and angular momentum of anisotropic dislocations*, J. Opt. Soc. Am., A, **13**, 967–973.

Siegman A.E., 1986, *Lasers*, University Science Books, Mill Valley.

Smith C.P., Dihardja Y., Weiss C.O., Lugiato L.A., Prati F., Vanotti P., 1993, *Low energy switching of laser doughnut modes and pattern recognition*, Opt. Commun., **102**, 505–514.

Soifer V.A., Golub M., 1994, *Laser beam mode selection by computer generated holograms*, CRC Press, London.

Soifer V.A., (Ed.), 2001, *Methods for computer design of diffractive optical elements*, Wiley–Interscience.

Soskin M.S., Gorshkov V.N., Vasnetsov M.V., 1997, *Topological charge and angular momentum of light beams carrying optical vortices*, Phys. Rev., A, **56**, 4064–4075.

Soskin M.S., Vasnetsov M.V., 2001, *Singular Optics*, Progress in Optics **42**, Chapter 4.

Stravroudis O.N., 1972, *The optics of rays, wavefronts and caustics*, New York, Acad. Press

Tamm Chr., Weiss C.O., 1990a, *Spontaneous breaking of cylindrical symmetry in an optically pumped laser*, Opt. Commun., **78**, 253–258.

Tamm Chr., Weiss C.O., 1990b, *Bistability and optical switching of spatial patterns in laser*, J. Opt. Soc. Am., B, **7**, 1034–1038.

Tang D.Y., Weiss C.O., Vanotti P., Smith C.P., 1994, *Optical "friction wheels" asymmetric seeding of the* TEM_{01} *hybrid mode of a He-Ne laser*, Opt. Commun., **105**, 320–324.

Thom R., 1972, *Structural stability and morphogenesis*, Benjamin, New York.

Tiwari S.C., 1992, *Geometric phase in optics quantal or classical?* J. Mod. Opt., **39**, 1097–1105.

Tiwari S.C., 1999, *Photons and vortices*, J. Mod. Opt., **46**, 1721–1731.

Toker G., Brunfeld A., Shamir J., 1993, *Diffraction of apertured Gaussian beams: solution by expansion in Chebyshev polynomials*, Appl. Opt., **32**, 4706–4712.

Totzeck M., Tiziani H.J., 1997, *Phase-singularities in 2D diffraction fields and interference microscopy*, Opt. Commun., **138**, 365–382.

Trimmer W., (Ed.), 2001, *Micromechanics and MEMS, Classic and Seminal Papers*, Wiley & IEEE Book Press.

Turnbull G.A., Robertson D.A., Smith G.M., Allen L., Padgett M.J., 1996, *The generation of free-space Laguerre–Gaussian modes at millimeter-wave frequencies by use of spiral phaseplate*, Opt. Commun., **127**, 183–188.

Turunen J., Wyrowski F., (Eds.), 1997, *Diffractive optics for industrial and commercial applications*, Akademie Verlag, Berlin.

Tychinsky V.P., Maslov I.N., Pankov V.L., Ublinsky D.V., 1989, *Computerized phase microscope for investigation of submicron structures*, Opt. Commun., **74**, 37–40.

Tychinsky V.P., 1989, *On superresolution of phase objects*, Opt. Commun., **74**, 41–45.

Tychinsky V.P., Velzel C.H.F., 1994, *Super-resolution in Microscopy*, [in:] *Current trends in optics*, Academic Press, chapter 18.

Vasnetsov M., Staliunas K., (Eds.), 1999, *Optical Vortices*, Nova Science Publishers, Inc., Commack, New York.

Vaughan J.M., Willetts D.V., 1983, *Temporal and interference fringe analysis of* TEM_{01}^{*} *laser modes*, J. Opt. Soc. Am., **73**, 1018–1021.

Vaupel M., Weiss C.O., 1995, *Circling optical vortices*, Phys. Rev. A, **51**, 4078–4085.

Velzel C.H.F., Masajada J., 1999, *Superresolution phase image microscope*, Opt. Appl., **39**, 293–300.

Whewell W., 1833, *Essay towards a first approximation to a map of cotidal lines*, Phil. Trans. Roy. Soc. Lond., 147–236.

Whewell W., 1836, *On the results of an extensive series of tide observations*, Phil. Trans. Roy. Soc. Lond., 289–307.

Wiry optyczne
i ich zastosowanie w interferometrii

Regularna sieć wirów optycznych może powstać w wyniku interferencji trzech fal płaskich. Sieć taka charakteryzuje się unikatowymi własnościami i jest bardzo wrażliwa na zaburzenia wprowadzone do jednej z interferujących fal. Własności sieci wirów optycznych wykorzystano w interferometrze, którego działanie jest oparte na wirach optycznych. Interferometr można skonfigurować na wiele sposobów. Jest więc on instrumentem, którego budowę można przystosować do specyficznych warunków pomiarowych. Kluczowym zagadnieniem decydującym o dokładności tego interferometru jest lokalizacja wirów optycznych. Aby rozwiązać ten problem, zaproponowano i przetestowano kilka metod ich lokalizacji. Metody te zapewniają rozdzielczość większą niż odległość między punktami pomiarowymi (pikselami) i są jednocześnie wystarczająco szybkie, aby umożliwić pomiar w czasie rzeczywistym. Przedstawiono też podstawowe własności fizyczne i zagadnienia techniczne związane z interferometrem opartym na wirach optycznych. Omówiono jego możliwe zastosowania, w tym: pomiar małych kątów obrotu, pomiar małych przesuwów liniowych, rekonstrukcję geometrii frontu falowego, interferometrię 3-D, zastosowania w mikroskopii nadrozdzielczej. Zagadnieniu pomiaru małych kątów obrotu poświęcono szczególną uwagę. Monografia zawiera również krótkie wprowadzenie do teorii wirów optycznych.

Contents